

The Pennsylvania State University

The Graduate School

**SOLID-STATE NANOPORE FABRICATION AND SENSING TOWARDS  
INTEGRATED NUCLEIC ACID TESTING**

A Dissertation in

Electrical Engineering

by

Zifan Tang

© 2022 by Zifan Tang

Submitted in Partial Fulfillment  
of the Requirements  
for the Degree of

Doctor of Philosophy

August 2022

The dissertation of Zifan Tang was reviewed and approved by the following:

Weihua Guan

Associate Professor of Electrical Engineering

Dissertation Advisor

Chair of Committee

Aida Ebrahimi

Assistant Professor of Electrical Engineering

Thomas Jackson

Professor of Electrical Engineering

Pak Kin Wong

Professor of Biomedical Engineering

Mehdi Kiani

Associate Professor of Electrical Engineering

Kultegin Aydin

Professor of Electrical Engineering

Head of the Department of Electrical Engineering

## ABSTRACT

Regular, accurate, rapid, and inexpensive self-testing for infectious diseases is urgently needed to optimize clinical care and guide infection control to limit disease spread. Nucleic Acid Amplification Test (NAAT) is the most sensitive and specific method, thus becoming the gold-standard technique for diagnosis. However, laboratory-based NAAT requires highly trained personnel, dedicated facilities, and instrumentations, delaying testing results and limiting testing capacity. Existing self-testing methods usually rely almost exclusively on rapid antigen tests. Typically, the sensitivity of antigen tests is 30% to 40% lower than the nucleic acid amplification testing (NAAT), which could miss a significant portion of infected patients. Therefore, a self-testing NAAT device for diagnosis is strongly needed to optimize clinical care and guide infection control to limit disease spread.

This thesis mainly focuses on exploring the possibility of developing a solid-state nanopore-based NAAT device for a new form of ultracompact, rapid, and label-free nucleic acid self-testing. We demonstrated the nucleic acid amplification coupled nanopore counting method for qualitative positive/negative nucleic acid testing. Due to its intrinsic single molecule sensitivity, the nanopore sensor could make a faster positive/negative call than bulk optical methods. To further explore a more reliable and integratable method for nanopore fabrication, we developed the laser-assisted breakdown method for single nanopore fabrication. We theoretically and experimentally demonstrated that combining a high laser power and a low electric field is statistically favorable for forming a single nanopore at a programmed location.

Furthermore, we developed a fully integrated sample-in answer-out NAT device for SARS-CoV-2 detection using a self-collected saliva sample. This system can automatically handle the complexity

of heat-inactivated sample preparation, pressure-driven sample dispensing, real-time RT-LAMP reaction and detection, and data processing and storage. Using an optical sensor, we achieved a limit of detection (LoD) of 5 virus particles/ $\mu$ l of saliva sample in 45 minutes. The final amplicons from the developed prototype were also detected by nanopore counting methods. Therefore, the success completion of this project will pave the way for ultracompact, rapid, and affordable nanopore-based nucleic acid testing.



## TABLE OF CONTENTS

LIST OF FIGURES .....	ix
LIST OF TABLES .....	xvi
ACKNOWLEDGEMENTS .....	xvii
Chapter 1 Introduction and Overview .....	1
1.1. Background .....	1
1.2. Overview of work presented .....	5
Chapter 2 Loop-Mediated Isothermal Amplification-Coupled Glass Nanopore Counting Towards Sensitive and Specific Nucleic Acid Testing .....	6
2.1. Introduction .....	7
2.2. Material and methods .....	9
2.3. Working principle .....	13
2.4. Result and discussion .....	15
2.4.1. DNA Concentration as a function of event rate .....	15
2.4.2. Concept validation .....	16
2.4.3. Resolving the pore-clogging by voltage cycling scheme.....	17
2.4.4. Probing LAMP reaction dynamics .....	19
2.4.5. Qualitative testing .....	23
2.4.6. Quantitative testing .....	24
2.4.7. Limit of detection considerations.....	26
2.5. Summary .....	27
Chapter 3 Rapid Detection of SARS-CoV-2 by RT-LAMP Coupled Solid-State Nanopores	28
3.1. Introduction .....	29
3.2. Material and method.....	31

3.2.1. Materials and chemicals.....	31
3.2.2. Glass nanopore fabrication and characterization .....	31
3.2.3. Nanopore sensing and data analysis .....	32
3.2.4. SARS-CoV-2 RT-PCR .....	33
3.2.5. SARS-CoV-2 RT-LAMP.....	33
3.2.6. Spiked saliva sample testing .....	35
3.2.7. Clinical nasopharyngeal sample testing and statistical analysis .....	35
3.3. Result and discussion .....	36
3.3.1. Overall workflow from sample to nanopore counting.....	36
3.3.2. SARS-CoV-2 RT-LAMP assay validation .....	37
3.3.3. Nanopore counting of RT-LAMP amplicons .....	39
3.3.4. Evaluation with spiked saliva samples .....	43
3.3.5. Clinical validation with nasopharyngeal swab samples.....	45
3.4. Summary .....	49
Chapter 4 On Stochastic Reduction in Laser-Assisted Dielectric Breakdown for Programmable Nanopore Fabrication.....	50
4.1. Introduction .....	51
4.2. Materials and methods .....	53
4.2.1. Materials and Chemicals.....	53
4.2.2. Instrumentation .....	53
4.2.3. Photoluminescence Characterization.....	54
4.2.4. Atomic Force Microscopy Characterization.....	55
4.2.5. Nanopore Fabrication and Validation.....	55
4.2.6. DNA Sensing .....	55

4.3. Result and discussion .....	56
4.3.1. Principle of Laser-Assisted Dielectric Breakdown.....	56
4.3.2. Kinetics of Laser-Induced Photothermal Etching of SiN <sub>x</sub> in Electrolyte .....	57
4.3.3. Confidence Model of Laser-Assisted Dielectric Breakdown .....	61
4.3.4. Probing Specific Cases in the Confidence Model.....	65
4.3.5. Programmable Nanopore Fabrication .....	69
4.3.6. DNA Translocation Experiments.....	71
4.4. Summary .....	73
Chapter 5 Saliva-Based SARS-CoV-2 Self-Testing with RT-LAMP in A Mobile Device..	74
5.1. Introduction .....	75
5.2. Experiment section.....	77
5.2.1. SARS-CoV-2 samples .....	77
5.2.2. RT-LAMP reaction mix.....	78
5.2.3. Instrumentation .....	78
5.2.4. APP development .....	79
5.2.5. Microfluidic reagent cartridge .....	80
5.2.6. Data processing.....	82
5.3. Result and discussion .....	83
5.3.1. Overall Design and Module Validations.....	83
5.3.2. Automated Salvia Processing on The Cartridge .....	87
5.3.3. Saliva Test Workflow .....	89
5.3.4. Evaluation with mock sample and clinical sample .....	91
5.3.5. Nanopore analyze of the final amplicons.....	96
5.3.6. Performance comparison .....	97

5.4. Summary ..... 99

5.5. Appendix ..... 100

Chapter 6 Conclusions and Future Perspectives ..... 102

6.1. Conclusions ..... 102

6.2. Future prospective ..... 104

Bibliography ..... 108

## LIST OF FIGURES

- Figure 2-1.** (a) Microscope, (b) TEM and (c) SEM image of the nanopipette. I-V characterization for all glass nanopore used. (d) Current-voltage curves for the glass nanopore in 1 M KCl with Tris-EDTA-buffer solution. (e) Conductance distribution of the glass nanopores. The nanopore size clearly varies from batch to batch. Typical conductance of the fabricated nanopore is in the range of  $20 \pm 10$  nS..... 12
- Figure 2-2.** Typical noise performance of the glass nanopore sensor in 1 M KCl Tris-EDTA buffer at 400 mV. (a) Current traces, the RMS noise was around 4.2 pA, (b) Power spectrum density for the ionic current signal..... 13
- Figure 2-3.** Illustration of the working principle of nanopore counting of amplicons. (a) Schematic measurement setup as well as the SEM and TEM of the glass nanopore. Amplicons are electrophoretically driven through the glass nanopore one by one, resulting in discernible events of the ionic current blockade. The event rate is proportional to the amplicon concentration. (b) Events in a positive target case. (c) Events in a negative target case. (d) Schematic event rate as a function of amplification time (or cycle). ..... 14
- Figure 2-4.** Continuous recordings of current trace under 500 mV bias with 5 kbp-DNA through glass nanopore at 1M KCl in Tris-EDTA-buffer solution. (a) Segments of the current trace at different DNA concentrations. (b) The normalized probability distribution of the inter-arrival time at different concentrations, with corresponding exponential fits. (c) The average event rate as a function of DNA concentration, showing a linear dependence ( $R^2 = 0.985$ )..... 16
- Figure 2-5.** Concept validation of nanopore counting of amplicons. Time traces for (a) negative no-template control (NTC), and (b) positive control before and after the 35 min LAMP reaction. The clogging issue was observed in the positive controls. (c) Gel electrophoresis image of the LAMP products (2% agarose gel)..... 17
- Figure 2-6.** Resolving the nanopore clogging by voltage cycling scheme. (a) A representative current trace showing normal, temporary clog and permanent clog. (b) Expanded view of the temporary clog. (c) Expanded view of the permanent clog. (d) Illustration of the voltage cycling scheme. The voltage is cycled between 1 s of 200 mV for sensing and 2 s of -100 mV for de-clogging. (e) A typical current trace using the voltage cycling scheme. (f) Reconstructed 5 s current trace by sequentially combining the current obtained under the 200 mV sensing voltage. A total of 487 events could be identified without clogging issue. .... 19
- Figure 2-7.** Summary of all current time traces obtained after indicated LAMP reaction time (the Pf genomic DNAs concentration is the 100 ng/ $\mu$ l). The green dash line is the noise threshold and the red dots represent the peak location of the current dip. (n: total number of translocation events detected). Note the differences in time scale. .... 22
- Figure 2-8.** Nanopore counting to probing the LAMP reaction dynamics. (a) Current traces at various amplification times. (b) The event rate as a function of the amplification time. The event rate increased exponentially before reaching a saturated level. The solid line is fitting to the logistic

growth model ( $RL=0.1s^{-1}$ ,  $RH=123.2s^{-1}$ ,  $\beta=0.75min^{-1}$  and  $t_0=29.2$  min). (c) Scatter plots showing current dip magnitude vs. dwell time at various reaction times..... 23

**Figure 2-9.** Validation of the *Pf* and *Pv* LAMP assays using *Pf* and *Pv* genomic DNA in benchtop real-time PCR machine (NTC: no template control). ..... 24

**Figure 2-10.** Qualitative specific nucleic acid testing using the nanopore-LAMP. (a) Current traces obtained from nanopore reading for *Pf*-specific assay, and (b) for *Pf*-specific assay. The event rate difference between the positive and the negative is evident. (c) Gel electrophoresis image (2% agarose gel) for *Pf*-specific assay and, (d) for *Pv*-specific assay..... 25

**Figure 2-11.** Comparison between the nanopore method and fluorescence-based method. (a) The results acquired from the nanopore detection. The solid lines were fittings to the logistic function (with fitting parameters summarized in Table S2). 1X, 0.1X, and 0.01X denote the dilution factors of the templates. 1× is equivalent to 100 ng/μl *Pf* genomic DNAs. (b) Amplification curves obtained from the fluorescence method using benchtop real-time PCR machine. (NTC: no template controls). (c) Standard curves extracted from the nanopore platform and the fluorescence platform. The linearity in the nanopore method suggests it could be used for quantitative analysis of DNA. .... 26

**Figure 3-1.** (a) The glass nanopores were characterized using an I-V scan in 1 M KCl, corresponding to a nanopore with about 10 nm in diameter. (b) Representative current time traces of master mix (negative control) samples. (c) Event rate of 9 negative control samples. The mean ( $\mu$ ) is  $0.009 s^{-1}$ , standard deviation ( $\sigma$ ) is  $0.007 s^{-1}$  and  $\mu+3\sigma$  was  $0.029 s^{-1}$ ..... 32

**Figure 3-2.** Workflow of RT-LAMP coupled nanopore method for SARS-CoV-2 detection. (a) Sample collection, preparation, and RNA extraction from either the nasopharyngeal swab sample or the saliva sample. (b) RT-LAMP amplification. One step RT-LAMP reaction is performed at 65°C for 15 min. (c) Nanopore readout. In a negative control sample, no amplification occurs, resulting in a negligible event rate. In a positive case, amplicons increased significantly, resulting in a sharp increase in event rate. The right panel shows the nanopore event rate as a function of RT-LAMP reaction time. The event rate threshold was set at  $1s^{-1}$  as the criteria for a positive call. 37

**Figure 3-3.** RT-LAMP assay validation. (a) N primer set results, and (b) E primer set results with viral RNA concentrations ranging from 2 and 105 copies per reaction. (c) Time to positive value comparison between the N primer set (blue bars) and the E primer set (grey bars) at different RNA concentrations. The N primer set showed better performances in terms of sensitivity and time to positive. (d) Real-time RT-LAMP result with a finer serial dilution (2×) using N primer set. (e) The extracted hit rate at various RNA concentrations to establish the assay LoD, which is determined to be 65 copies at 95% confidence level. (f) Time to positive value with N primer sets at concentrations ranging between 102 and 105 copies per reaction. A good linearity is obtained, indicating that a semi-quantitative test is feasible. (g) Real-time RT-LAMP result in saliva RNA background. (h) Real-time RT-PCR result in saliva RNA background. (i) The correlation between the RT-PCR and RT-LAMP measurement in total saliva RNA background. .... 40

**Figure 3-4.** Nanopore counting of RT-LAMP amplicons. (a) Gel electrophoresis (2% agarose gel) result of the RT-LAMP products, at various reaction times from 0 mins to 16 mins. (b)

Corresponding current time traces measured in nanopores with 200 mV bias (Note the scale differences). (c) Corresponding current drop vs. dwell times distribution at different reaction times. (d) Corresponding event rate distribution as a function of ECD values. (e) The total event rate as a function of the reaction time. The solid line is fitting to the logistic growth model  $R^2=0.95$ . ... 43

**Figure 3-5.** Real-time result of the RT-LAMP reaction using the SARS-CoV-2 spiked saliva sample at different concentrations. .... 44

**Figure 3-6.** Analytical sensitivity and specificity test with saliva spiked sample. (a) Event rate of the RT-LAMP amplicons at various concentrations of SARS-CoV-2 in total saliva RNA background. An event threshold of  $1 \text{ s}^{-1}$  is used for positive/negative call. (b) The event rate for SARS-CoV-2 and three other non-SARS-CoV-2 targets with a concentration of  $10^5$  copies in total saliva RNA background. All non-SARS-CoV-2 targets showed event rates much less than  $1 \text{ s}^{-1}$  and were correctly classified as negatives. .... 45

**Figure 3-7.** Diagnostic sensitivity and specificity test with clinical nasopharyngeal swab samples. (a) Event rate of the RT-LAMP amplicons for a total of 127 samples. These samples were initially tested with RT-PCR (50 positives and 77 negatives). A predefined event rate threshold of  $1 \text{ s}^{-1}$  and a ROC optimized event rate threshold of  $1.25 \text{ s}^{-1}$  were used in nanopore sensors to classify the samples. (b) ROC curve analysis of the test result. The area under the ROC curve (AUC) is 0.96. .... 47

**Figure 4-1.** Schematic drawing of the nanopore fabrication by (a) normal breakdown and (b) laser-assisted breakdown. The drawings are for illustrative purposes and not to scale. (c) Schematic of the custom-built nanopore fabrication and characterization system. (BS: beam splitter, DM: dichroic mirror, ND: neutral-density filter). The focused laser spot at an arbitrary location on the membrane (inset i) and the Gaussian intensity profile of the laser (inset ii). .... 54

**Figure 4-2.** (a) Photoluminescence (PL) probed after exposing the  $\text{SiN}_x$  to the laser in the air. (b) AFM characterization of the sample exposed in the air (dash circles are the laser exposed regions). The counted emission photons were normalized to the integration time and the incident laser power (cpms/mW: counter per millisecond/milliwatt). No significant morphology change was observed. (c) PL probed after exposing the  $\text{SiN}_x$  to the laser in 2 M KCl solution. (d) AFM characterization of the sample exposed in 2 M KCl solution. The material etching was visible in the laser spots. (e) Extracted  $\text{SiN}_x$  etching rate as a function of the laser power. Note that the measured etching rate is the maximum etching rate in the membrane thickness direction. The solid line is the Arrhenius fitting. The PL map was obtained by scanning at 1 mW laser power with 200 nm step and 2 ms integration time. .... 57

**Figure 4-3.** AFM-obtained etching profiles in Figure 4-2. .... 59

**Figure 4-4.** Finite-element simulation to study the photothermal heating of the solution. Heat transfer model was implemented by applying the first law of thermodynamics. (a) The physical domain used for simulation. A 30-nm-thick  $\text{SiN}_x$  membrane was placed in the middle of the simulation domain and surrounded by water. At the bottom of the  $\text{SiN}_x$  membrane, a heat source (Q) with Gaussian distribution of intensity was applied on an area with a radius of  $1 \mu\text{m}$  to simulate the focused laser radiation. (b) Steady-state temperature profile under a 20 mW laser. The peak

temperature is located in the center of the spot and quickly decreases to room temperature. The maximum temperature caused by the 20 mW laser was 175 °C, which is far below the SiN<sub>x</sub> decomposition temperature. (c) Peak temperature as a function of laser power. The temperature increases linearly with laser power. The slope of the line is the photothermal coefficient (8.06 K/mW). (d) Boundary conditions used in simulation. (e) Parameters used in simulation..... 60

**Figure 4-5.** (a) PDF and (b) CDF of representative Weibull distribution of time to breakdown for the normal and laser-assisted breakdown. (Parameters: Normal breakdown: 0.6 V/nm; Laser-assisted breakdown: 0.6 V/nm and 50 mW laser;  $\lambda n = 24501s$ ,  $\lambda la = 1362s$ ,  $\beta = 0.63$ ). (c) Calculated confidence map of single nanopore localization at different laser powers and electric fields. Parameters used: integration constant  $B = 5 \times 10^{15} s$ , field acceleration factor  $\gamma = 38 \text{ nm/V}$ , membrane thickness  $d_0 = 30 \text{ nm}$ , photothermal coefficient  $b = 8.06 \text{ K/mW}$ , shape parameter  $\beta = 0.63$ . (d) laser-assisted breakdown at different electric fields (0.5-1 V/nm) and laser powers (5 and 20 mW). The top panels are microscope images with bright spots showing the locations of the focused laser spot. The bottom panels are ionic current mapping results, performed at 4 mW laser power and 100 mV voltage with 10  $\mu\text{m/s}$  scanning speed. The PDF and CFD of all cases can be found in Figure 4-6. .... 63

**Figure 4-6.** (a-c) Probability density function (PDF) and (d-f) Cumulative distribution function (CDF) of Weibull distribution of time to breakdown for normal and laser-assisted breakdown at different electric fields (0.5-1 V/nm) and laser powers (5-20 mW). .... 64

**Figure 4-7.** (a) Flowchart of the automated procedure for laser-assisted breakdown nanopore fabrication. The moving Z-Score is an online adaptive learning algorithm for detecting the abnormal points in a time-trace. It measures the number of standard deviations each new observation is away from the mean over a pre-defined time window length of  $w$ ,  $Zk = \frac{Ik - \text{mean}(Ik - 1: Ik - w)}{\text{std}(Ik - 1: Ik - w)}$ . The detailed description of the moving Z-score method can be found in our previous work [110]. (b) A representative nanopore fabrication process at 0.8 V/nm and 20 mW. The nanopore diameter estimated by the conductance measurement was about 5.2 nm. (c) Scanned ionic current mapping before (top) and after (bottom) the nanopore fabrication. Ionic current mapping experiments were performed at 4 mW laser power and 100 mV voltage with 10  $\mu\text{m/s}$  scanning speed. .... 67

**Figure 4-8.** (a) A representative nanopore fabrication process at 1 V/nm initial electric field and 20 mW laser power. Nanopore was formed around 10 s. The nanopore diameter estimated by the conductance measurement was about 102 nm. (b) Scanned ionic current mapping before (top) and after (bottom) the nanopore fabrication. Ionic current mapping experiments were performed at 4 mW laser power and 100 mV voltage with 10  $\mu\text{m/s}$  scanning speed. .... 68

**Figure 4-9.** Normal breakdown at 0.8 V/nm without laser. The top figures are microscope images before fabrication. The bottom color maps are ionic current mapping results, which were performed at 4 mW laser power and 100 mV voltage with 10  $\mu\text{m/s}$  scanning speed..... 68

**Figure 4-10.** (a) Programmable laser-assisted breakdown fabrication using 20 mW laser and low electric field ranging from 0.03 V/nm to 0.4 V/nm. The bright spots in the top microscope images show the laser location. The bottom laser enhanced ionic current mappings show the number and location of the fabricated nanopores. All ionic current mapping experiments were performed at 2



mW laser power and 100 mV voltage with 20  $\mu\text{m/s}$  scanning speed. (b) Overlay of the extracted laser location and the formed nanopore location. The error bar indicates the full width at half maximum (FWHM). (c) The nanopore fabrication time as a function of the electric field. (d) The formed nanopore diameter as a function of the electric field. The nanopore diameter is determined by the IV measurement. The line in (d) is used to guide the eyes. .... 70

**Figure 4-11.** Conductance measurement. I-V curves of the nanopore fabricated by laser-assisted breakdown method at 20 mW laser and low electric field ranging from 0.03 V/nm to 0.4 V/nm. All measurements were performed in 1M KCl with 10mM Tris, and 1mM EDTA. .... 70

**Figure 4-12.** (a) A representative current time-trace for 100 pM 48.5 kbp  $\lambda$ -DNA molecules translocating through a 10 nm nanopore at 300 mV bias. The magnified insets show two typical ionic current blockades during the translocation. (b) Scatter plot of the current blockades versus dwell time for a total of 238 translocation events. (c) Power spectrum density (PSD) of the ionic current obtained at 300 mV with a low-pass filter at 10 kHz. .... 71

**Figure 4-13.** Measured power spectral density (PSD) of the normal breakdown and laser-assisted breakdown nanopore. The estimated pore diameter of normal breakdown methods and laser-assisted breakdown method are 9 nm and 10 nm respectively. All experiments were performed with 1 M KCl at 300 mV with a low-pass filter at 10 kHz. .... 72

**Figure 5-1.** The flow chart of the android App development. First, the App interface guides users to provide their personal information. Second, we set up Bluetooth communication. App interface scans and connects the Bluetooth LE around the analyzer. The communication protocol can be built using the Service UUID and Characteristic UUID of the Bluetooth LE, enabling the data communication function between these two devices. The third part is the real-time data transfer and plotting. We added two check bits at the beginning and the end of the string to ensure accuracy. After confirming the check bit of the received string from the analyzer, the string value will be split into three channels and plotted with different colors. Meanwhile, the split data in each channel is compared with the threshold value (RFU 50) to make the decision. If more than or equal to two channels have three successive data greater than the threshold, the test result will be identified as a positive. Otherwise, the App will continue to receive the string value from the analyzer. If no positive result has been determined after 30 minutes of the amplification, the test result will be negative. In the end, the APP will combine personal information, color sensor data in each channel, and test results into a spreadsheet. This file can be saved on the local device and uploaded to a Google drive. .... 81

**Figure 5-2.** Mobile phone user interface and result unloading. The Android SLIDE application guides the user through steps to set up and run the test. (a-b) Collect user information. (c-e) Instructions for the user to collect samples. (f-h) Selection of the Bluetooth and the test initiation. (i) Real-time analysis during the test (g) Upload the testing result to local or Google drive. .... 82

**Figure 5-3.** Representative measurement for 9 negative control samples. All of the samples were measured for 45 minutes. The baseline varies from RFU 28 to 42. Therefore, we set the RFU 50 as the threshold to avoid false positives. .... 83

**Figure 5-4.** System diagram. An Arduino nano microcontroller incorporates five subsystems: thermal modules, optical module, pump module, connectivity module, and power module..... 84

**Figure 5-5.** SLIDE Instrument design and validation. (a) Schematic of the SLIDE device showing components in an exploded view. The platform consists of five main functional modules: optical module (LED/optical sensor), thermal modules (power resistor/thermal sensor), micro pump modules, power supply module (battery), and data connectivity modules (Bluetooth). Each module was controlled by a microcontroller on a customized PCB board. (b) Photograph of the SLIDE analyzer and the smartphone interface. (c-d) Characterization of the optical sensor using 40  $\mu\text{l}$  calcein solution for 10 minutes of recording. The optical sensor showed a linear response to the concentration of calcein from 0 to 25  $\mu\text{M}$ . The temperature profile of the heating block and the liquid (saliva/assay) for (e) 95°C virus heat inactivation and 65°C RT-LAMP reaction. (g) Characterization of the piezo pump frequency with the flowrate. (h) Characterization the power consumption for one test..... 86

**Figure 5-6.** (a) Exploded view of the cartridge with three PMMA layers: top-loading layer, middle microchannel layer, and bottom covering layer. (b) Assembled view of the cartridge includes a saliva collection chamber (250  $\mu\text{l}$ ), three trapping chambers (10  $\mu\text{l}$ ), three reaction chambers (60  $\mu\text{l}$ ) with preloaded RT-LAMP master mix (30  $\mu\text{l}$ ), two wax valves in each reaction chamber (six in total), and a waste chamber for collecting the rest of the saliva sample. (c) One unit of the dispensing and reaction chamber. Illustration of (d) trapping and (e) dispensing processes. (f) One example of sample trapping and dispensing processes (Supplementary Video S2). The blue liquid is the saliva with the blue dye. The orange liquid is the RT-LAMP master mix with orange dye for better visualization..... 88

**Figure 5-7.** Overall SLIDE workflow. (a) Step 1: the patient self-collect  $\sim 120 \mu\text{L}$  of saliva into a cartridge using saliva collection aid. The users tighten the screw cap and connect the lure luck to the micro pump. Step 2: Insert the cartridge into the analyzer. Step 3: Connect the SLIDE analyzer with a smartphone through Bluetooth to initiate the test. (b) Step by step instruction of APP interface, including personal information collection, sample collection guidance, Bluetooth connection, test initiation, receiving and plotting real-time amplification data on the phone screen, and upload all data to the cloud. .... 90

**Figure 5-8.** The Flow chart of the automatic workflow from sample collection, sample preparation, sample dispensing, RT-LAMP reaction, and result storage..... 92

**Figure 5-9.** SLIDE device performance evaluation. (a) Real-time RT-LAMP results with different concentrations of the spiked saliva samples (1 virion/ $\mu\text{l}$  to 104 virion/ $\mu\text{l}$ ) using a SLIDE analyzer. The threshold to classify an amplification curve as positive or negative was 50 RFU based on the NTC sample (Supplementary Figure S5). (b) The extracted hit rate at various virus particle concentrations to establish LoD. (c) The inversely proportional relationship between the threshold time ( $T_t$ ) and virus particle concentration was obtained from the SLIDE analyzer. (d) The Pearson correlation analysis of the threshold time ( $T_t$ ) between the manual operation with PCR machine and automatic method using SLIDE analyzer. (e) Two clinical samples, one known positive(top) and one known negative(bottom), were tested by the SLIDE device. The RT-PCR assay performed the initial diagnosis as the reference. The experiment follows the process flow schematic shown in Figure 5-7. .... 93

**Figure 5-10.** The real-time amplification result for the mock samples at low concentrations from 1 to 10 virion/ $\mu$ l using the SLIDE analyzer. The final results were labeled on the figure based on our voting system..... 94

**Figure 5-11.** Real-time RT-LAMP results with different concentrations of the Spiked saliva samples (1 copies/ $\mu$ l to 104 copies/ $\mu$ l) using a PCR machine. The Spiked saliva samples were manually prepared in the heating block for 5 min at 95°C. 10  $\mu$ l of the sample was taken by pipette and transferred into the 30  $\mu$ l of the RT-LAMP master mix (b) The extracted hit rate at various virus particle concentrations to establish LoD. (c) The inversely proportional relationship between the time to positive and virus particle concentration. .... 94

**Figure 5-12.** Two clinical samples, one known positive(top) and one known negative(bottom), were tested by the SLIDE device. The RT-PCR assay performed the initial diagnosis as the reference. The experiment follows the process flow schematic shown in Figure 5-8 and Supplementary Video S1. .... 95

**Figure 5-13.** Validation of nanopore counting of the end-product of the RT-LAMP reaction from the saliva sample. (a) negative control (NTC), and (b) positive control after the 30 min ..... 97

**Figure 5-14.** PCB design for all the sub modules: color sensor module, LED module control PCB module. .... 101

## LIST OF TABLES

<b>Table 1-1.</b> Different readout method comparison .....	3
<b>Table 2-1.</b> Reagent setup of LAMP master mix.....	10
<b>Table 2-2.</b> Primer sets for <i>Pf</i> -, and <i>Pv</i> -specific LAMP amplification .....	10
<b>Table 2-3.</b> Parameter values for fitting the logistic function fit in Figure 2-8 .....	26
<b>Table 3-1.</b> RT- PCR primer sets targeting N1 regions of SARS-Cov-2 .....	33
<b>Table 3-2.</b> RT-LAMP primer sets targeting N and E regions of SARS-Cov-2.....	34
<b>Table 3-3.</b> RT- LAMP Master mix.....	34
<b>Table 3-4.</b> Statistics of analyzing 127 clinical nasopharyngeal swab samples .....	46
<b>Table 3-5.</b> Summary of clinical sample testing with RT-PCR and nanopore method .....	47
<b>Table 4-1.</b> Parameters used for Arrhenius fitting in Figure 4-2e .....	61
<b>Table 4-2.</b> Comparison between normal breakdown and laser-assisted breakdown physics .....	64
<b>Table 4-3.</b> Parameters used in Figure 3a & Figure 3b.....	65
<b>Table 4-4.</b> Parameters used in Figure 3c .....	65
<b>Table 5-1.</b> RT- LAMP Master mix in SLIDE Test .....	78
<b>Table 5-2.</b> Time to positive with mock sample using manual operation.....	95
<b>Table 5-3.</b> Time to positive with different concentration of mock sample using SLIDE .....	96
<b>Table 5-4.</b> Performance comparison between SLIDE analyzer with commercially available NAT devices .....	98
<b>Table 5-5.</b> Bill of materials for analyzer .....	100

## ACKNOWLEDGEMENTS

This doctoral degree has been a life-changing experience, a long journey that would not have been possible without the support of many people. My gratitude cannot be expressed in these few lines, but I will give it a try.

First, I would like to recognize the invaluable guidance of my supervisor, Professor Weihua Guan. He has taught me the methodology to think, study, and conduct research. He has always inspired and guided me to be a hardworking, responsible, and passionate researcher. It was a great honor to work with him, and I am incredibly thankful for what he has offered me. I would also like to give my special regards to Dr. Tom Jackson. His expertise and support were vital in inspiring me to think outside the box and form a unique creative process from multiple perspectives.

For this dissertation, I would like to thank my defense committee members: Dr. Aida Ebrahimi, Dr. Pak Kin Wong, and Dr. Mehdi Kiani, for their time, guidance, and constructive comments. I would like to extend my wholehearted gratitude to all my lab members, current and previous, for their encouragement, contribution, and suggestions for many aspects of my life. Also, I would like to thank all of the collaborators for sharing their knowledge, skills, and tips. Thanks to all of you for having welcomed me into this academic family. Without you, this journey would not have been the same.

The work presented in this dissertation was supported in part by the National Institutes of Health (NIH) under Grant R6AI147419 and National Science Foundation (NSF) under grant No. 1902503, 1912410 and 1710831. The views and opinions of the author expressed herein do not state or reflect those of federal fundings, and shall not be used for advertising or product endorsement purposes.

Finally, I am incredibly grateful to all of my friends and family. You have been a solid pillar of support throughout my life, and I thank all of you for your unconditional love, care, and encouragement throughout the many years.

Zifan Tang

# Chapter 1 Introduction and Overview

## 1.1. Background

Communicable diseases with their infectious etiology cause around 4 million deaths each year globally [1]. Notable examples of recent communicable outbreaks include ongoing pandemics COVID-19 [2] and HIV [3], Ebola(2013- 2015), Zika virus(2013-2015), H1N1 Influenza (2009-2010), MERS (2007) [4], and other ongoing challenges including respiratory diseases (Tuberculosis, Measles, etc.), diarrheal diseases (Rotavirus, E. coli, etc.), mosquito-borne pathogens (Malaria, etc.), and sexually transmitted infections (Chlamydia, Gonorrhea, Syphilis).

Traditionally, the detection of these targets can be achieved by techniques including (1) cell culture [5], (2) enzyme-linked immunosorbent assay (ELISA) [6], (3) lateral-flow immunoassay (LFA) [7], and (4) nucleic acid amplification testing (NAAT) [8]. Cell culture, NAAT, and lateral-flow immunoassay are direct methods. They can detect the pathogens directly by observing the pathogen nucleic acids and the antigens from the pathogen, respectively. ELISA is an indirect method that detects antibodies developed by the patients[9]. In general, direct detection offers higher confidence for the active infection than indirect detection but requires more resources for testing (e.g., time, equipment, cost, trained personnel). Cell culture is one of the earliest developed testing methods and requires well-equipped laboratories and long incubation times up to days, which is not suitable for fast response. The LFA and the ELISA are based on antibodies binding to the target antigen or protein of interest [9, 10]. For ELISA, the major concern is the non-specific protein adsorption, which leads to low specificity. For LFA, since there is no amplification step involved, resulting in lacks the sensitivity required for many diagnostic

applications. Among these three approaches, NAAT is perhaps the most powerful method due to its relatively short time to result, high sensitivity, and specificity. For many pathogens, NAAT is the preferred gold-standard testing method.

The NAAT typically has three essential steps: (1) Cells or virus particles are lysed, and nucleic acids (NAs) are purified and concentrated from the patient sample. (2) target sequence amplification uses polymerase chain reaction (PCR) to generate billions of DNA copies. (3) Real-time/endpoint detection. If the pathogen is present, many DNA copies will be generated. The amplified NAs are typically detected by the optical method. Ideally, this whole process can be performed in two hours in a well-equipped medical center by a well-trained healthcare worker. However, due to many places lacking facilities, the tests cannot be performed immediately during the initial visit. It has to go through all the logistics around specimen collection, transport to a centralized laboratory, and returning results, which takes up to 7 days. This delay often leads to missed opportunities to immediately make treatment decisions and prevent the diseases from spreading [11]. Delays in obtaining the results can increase the risk of virus transmission. The longer patients wait, the more likely they will not self-isolate when they are most infectious and will resume daily activities before receiving test results. The long turn-around time for laboratory testing becomes particularly problematic in low-resource settings and during the pandemic outbreak. In the recent COVID-19 pandemic [12], we have observed the long shipping times, lack of trained personnel to process samples and a shortage of diagnostic testing supplies. All countries have been facing an unmet need to achieve a timely and effective screening response to enable the pandemic tracking, individual quarantining, appropriate treatments, contact tracing, etc. Therefore, a fully integrated self-testing NAAT device is strongly needed to optimize clinical care, guide infection control to the ongoing COVID-19 spread, and also fight for the future pandemics.



Traditional NAT are often read out using different optical methods, such as changes in turbidity caused by magnesium pyrophosphate precipitate [13], changes in fluorescence using dyes [14-16], colorimetric pH indicators [17, 18], or gel electrophoresis followed by UV detection [19]. Each of these methods would require a minimum concentration of the signaling reporters for the readout system to distinguish between positives and negatives. Depending on different readout systems (*e.g.*, naked eye [20] versus highly sensitive fluorescence detector [21, 22]), the  $c_{min}$  could range from mM to nM. This required minimal signaling reporter concentration can be linked to the time to positive (TTP) as  $c_{min}=TTP \times v_r$ , in which  $v_r$  is the average reaction rate of the assay. It is evident that reducing the detection  $c_{min}$  is preferred towards quick time to positive. In this regard, the intrinsic single-molecule sensitivity of nanopore sensors [23, 24] is highly intriguing since it enables a significantly reduced  $c_{min}$  and thus reduces the time required for making the positive/negative call. Moreover, unlike other methods to read the additional reporters or by-product of the amplification, the nanopore is a label-free method that can directly probe molecule itself (concentration and size). This will not only significantly decrease the false positive rate caused by incorrectly produced by product or reporter, but also provide another opportunity to achieve multiplexing based on the amplicons size. Last but not least, this fully electronic nanopore readout method can be integrated and scaled up to a portable system (**Table 1-1**).

**Table 1-1.** Different readout method comparison

	SENSITIVITY ( $C_{MIN}$ )	SPECIFICITY	MECHANISM	PORTABLE
<b>OPTICAL SENSOR[25] (POCT)</b>	100 nM	++	Mg2+ precipitate	Y
<b>OPTICAL SENSOR (BENCHTOP) [14-16]</b>	100 pM	++	Fluorescence dye	N
<b>FET[26]</b>	1 pM	++	pH	Y
<b>NAKED EYE[17, 18]</b>	1 $\mu$ M	++	pH (Colorimetric)	Y
<b>NAKED EYE[13]</b>	1 $\mu$ M	++	Turbidity	Y
<b>GEL ELECTROPHORESIS</b>	100 pM	+++	Molecule size and concentration	N
<b>NANOPORE[27]</b>	10 pM	+++	Molecule size and concentration	Y

This thesis mainly focuses on exploring the possibility of developing a fully integrated NAAT system using solid-state nanopores for rapid, label-free nucleic acid self-testing. The main contribution of this thesis is as follows.

First, we demonstrated the RT-LAMP-coupled nanopore counting method for label-free nucleic acid testing. This approach lends itself to most amplification strategies as long as the target template is specifically replicated in numbers. For qualitative positive/negative classification of a testing sample, the nanopore sensor was used to measure the concentration by the digital counting method. We found that LAMP-coupled glass nanopore counting has the potential to be used in qualitative as well as quantitative tests. Due to its intrinsic single molecule sensitivity, the nanopore sensor could make a faster positive/negative call than bulk optical methods. The highly sensitive and specific sensing strategy would open a new avenue for solid-state nanopore sensors towards a new form of compact, rapid, low-cost nucleic acid testing at the point of care.

To further explore a more reliable and integratable method for nanopore fabrication, we developed an optical system for single nanopore fabrication and characterization. We developed and validated a physical model to project the confidence level for single nanopore fabrication using a laser-assisted breakdown method. The physical model and experimental data suggest that a combination of high laser power and a low electric field is statistically favorable for forming a single nanopore at a programmed location. With the knowledge of the optimized conditions for single nanopore localization, we experimentally programmed to fabricate and probe a single nanopore at an arbitrary spot.

Thirdly, we developed a fully integrated SARS-CoV-2 nucleic acid testing (NAT) device using a self-collected saliva sample. This platform consists of a ready-to-use reagents cartridge, an easy-to-use smartphone interface, and an ultra-compact and less-expensive analyzer. It can automatically

handle the complexity of heat-inactivated sample preparation, pressure-driven sample dispensing and mixing, as well as real-time RT-LAMP reaction and detection, and data processing, storage, and upload. We achieved a limit of detection (LoD) of 5 virus particles/ $\mu\text{l}$  of saliva sample in 45 minutes with the optical readout system. Based on our first study, the turnaround time is expected to decrease further with the integrated nanopore readout system.

## **1.2. Overview of work presented**

The first part of the thesis (Chapters 2 and 3) discusses the efforts to demonstrate a loop-mediated isothermal amplification LAMP-coupled glass nanopore counting strategy for infectious disease applications. Chapter 2 explores the underlying mechanism of digital counting and uses malaria as a model sample for proof of concept. Chapter 3 studied the sensitivity, specificity, limit of detection, and diagnosis ability of the LAMP-coupled nanopore method using SARS-CoV-2. To improve the reliability and fidelity of nanopore fabrication, in Chapter 4, we developed and validated a physical model to project the confidence level for single nanopore fabrication using the laser-assisted breakdown method. In Chapter 5, we develop a fully integrated "sample-to-answer" mobile NAT platform for highly sensitive and specific SARS-CoV-2 self-testing. The novel strategy for the streamlined sample process includes sample preparation, sample dispensing, amplification, and detection. Finally, Chapter 6 offers conclusions based on the work presented in the preceding chapters and perspectives for future development.

## **Chapter 2 Loop-Mediated Isothermal Amplification-Coupled Glass Nanopore Counting Towards Sensitive and Specific Nucleic Acid Testing**

In this chapter, we demonstrate a novel loop-mediated isothermal amplification (LAMP)-coupled glass nanopore counting strategy that could effectively address these challenges. By using the glass nanopore in the counting mode (versus the sizing mode), the device fabrication challenge is considerably eased since it allows a certain degree of pore size variations and no surface functionalization is needed. The specific molecule replication effectively breaks the diffusion-limited mass transport thanks to the exponential growth of the target molecules. We show the LAMP-coupled glass nanopore counting has the potential to be used in a qualitative test as well as in a quantitative nucleic acid test (NAT). This approach lends itself to most amplification strategies as long as the target template is specifically replicated in numbers. The highly sensitive and specific sensing strategy would open a new avenue for solid-state nanopore sensors towards a new form of compact, rapid, low-cost nucleic acid testing at the point of care.

## 2.1. Introduction

Due to its conceptual simplicity and label-free operations, nanopore sensors have attracted intense research interest in electronic single-molecule detection. The nanopore sensor is typically operated by applying a potential difference across the two chambers to electrophoretically drive charged biopolymers through the nanoscale orifice. The readout is a current time trace with dips corresponding to single-molecule translocation, usually called an event. Analysis of features within each identified event (e.g., dip magnitude, shape, and duration) provides the basis for interpreting the molecule length, shape, charge, and reactivity to the nanopore surface [28]. Among various nanopore types, due to their mechanical robustness, tunable size, and potential for integration and miniaturization, solid-state nanopores [29] made with silicon nitride [30-32], glass [33-35], and graphene [36] have become a versatile analytical tool for analyzing nucleic acids and proteins.

While solid-state nanopores have achieved tremendous success, there exist three common challenges. The first is pore size variations from batch to batch. Despite significant advancement in solid-state nanopore fabrication techniques [37], repeatable pore size control remains challenging. Since the analyte is detected by the exclusion of ions from the sensing pore volumes, the pore size change would cause the sensing signal varying from one experiment to the other, making the interpretation of the sensing results difficult. The second is the nanopore sensor specificity. The specificity was usually encoded into the dwell time or current dip shapes. A common approach for achieving the specificity is through introducing specific binding sites on the nanopore wall surface [38, 39]. However, controlling the location and number of binding sites within the nanopore sensing volume is not without challenges. The additional steps of surface functionalization could limit the device yield [40]. In addition, a specifically modified nanopore means that nanopore can only be used for a fixed target without being generally applicable. Another approach for introducing the specificity is through specific probe molecules. For example,

engineered double-strand DNA carriers were used for sensing specific proteins [41, 42] and specific DNAs [43]. The third challenge is the prolonged sensor response time at low analyte concentrations [29, 44]. Although the nanopore sensor itself has single molecule sensitivity, the diffusion-limited mass transport in nanopore sensors could severely impact the sensor response time [44-46]. It was estimated that if the analyte concentration is sub-picomolar, it will take more than 1-hour to observe a single event [47].

To extend the capabilities of solid-state nanopores and realize practical devices, alternative sensing strategies are highly desirable. One such strategy is to increase the number of specific target molecules present. In fact, target molecule replication was a mature and proven strategy in nucleic acid amplification tests (NAATs). As one of the most sensitive methods available, NAATs have a wide range of applications ranging from infectious disease diagnosis, food pathogen screening, and forensic investigations to homeland security. NAAT employs enzymatic polymerization reaction in which a few copies of templates (low analyte concentration) can be replicated specifically into a large number of amplicons (high analyte concentration). There have been a variety of molecule replication strategies developed. In addition to the traditional polymerase chain reaction (PCR), isothermal methods such as loop-mediated isothermal amplification (LAMP) [48, 49], nucleic acid sequence-based amplification (NASBA) [50], and recombinase polymerase amplification (RPA) [51] have shown great promise for field use since they do not require thermocyclers and often are very fast.

In this work, we reported a LAMP-coupled glass nanopore counting method for highly sensitive and specific nucleic acid testing. By using the glass nanopore in its simplest form of event counting (versus analyzing the shape features of the current blockade), the device fabrication challenge is considerably eased since it allows a certain degree of pore size variation (as long as it can still resolve single molecules) and requires no surface functionalization. The LAMP replication

simultaneously offers the requisite specificity, and effectively breaks the diffusion-limited mass transport at low analyte concentration thanks to the exponential growth of the target molecules. We examined the ability of the glass nanopore to capture the LAMP reaction dynamics. We found that LAMP-coupled glass nanopore counting has the potential to be used in a qualitative as well as quantitative test. The amplification-coupled nanopore counting approach would open a new avenue towards compact and robust electronic nucleic acid testing at the point of care.

## 2.2. Material and methods

**Materials and chemicals.** Quartz capillaries with inner and outer diameter of 0.5 and 1 mm were used in our experiment (Sutter Instrument, USA). Pipette holder (QSW-T10N) was purchased from Warner Instruments. Ag/AgCl electrodes were home-made with 0.2 mm Ag wires (Warner Instruments, USA). Micro-injector with 34 gauge was purchased from World Precision Instruments. 5kbp DNA (0.5  $\mu\text{g}/\mu\text{l}$ ) were purchased from ThermoFisher. KCl and Tris-EDTA-buffer solution (pH 8.0) were purchased from Sigma-Aldrich. All solutions were filtered with a 0.2  $\mu\text{m}$  syringe filter (Whatman). Mineral oil was purchased from Sigma-Aldrich. The *Pf* genomic DNAs (100 ng/ $\mu\text{l}$ ) and *Pv* genomic DNAs (4.7ng/ $\mu\text{l}$ ) were gifts from Dr. Cui's lab at Penn State, extracted by phenol-chloroform based procedure.

**LAMP assay.** The LAMP reaction mix (25  $\mu\text{l}$ ) contains isothermal buffer (20 mM Tris-HCl, 10 mM  $(\text{NH}_4)_2\text{SO}_4$ , 50 mM KCl, 2 mM  $\text{MgSO}_4$ , 0.1% Tween 20, pH 8.8), PCR grade  $\text{H}_2\text{O}$ ,  $\text{MgSO}_4$  (7 mM),  $\text{MnCl}_2$  (0.75 mM), calcein (25  $\mu\text{M}$ ), deoxyribonucleotide triphosphates (dNTPs, 1.4 mM), Bst 2.0 DNA polymerase, DNA template, and primer sets (0.2 mM F3 and B3c, 1.6 mM FIP and BIP, 0.8 mM LPF and LPB). **Table 2-1** shows the reagent recipe for the LAMP assay. The *Pf*-

specific and *Pv*-specific primer sets were listed in **Table 2-2**. The LAMP assay was performed at a constant temperature of 65°C.

**Table 2-1.** Reagent setup of LAMP master mix

Component	Concentration	Volume
PCR grade water	1 x	9.25 µl
Primer sets	-	6.50 µl
Isothermal buffer	1 x	2.50 µl
MgSO <sub>4</sub>	7.00 mM	1.75 µl
Calcein	25.00 µM	0.63 µl
MnCl <sub>2</sub>	0.75 mM	1.88 µl
dNTP mix	1.40 mM	3.50 µl
<i>Bst</i> DNA polymerase	0.32 Unit/µl	1.00 µl

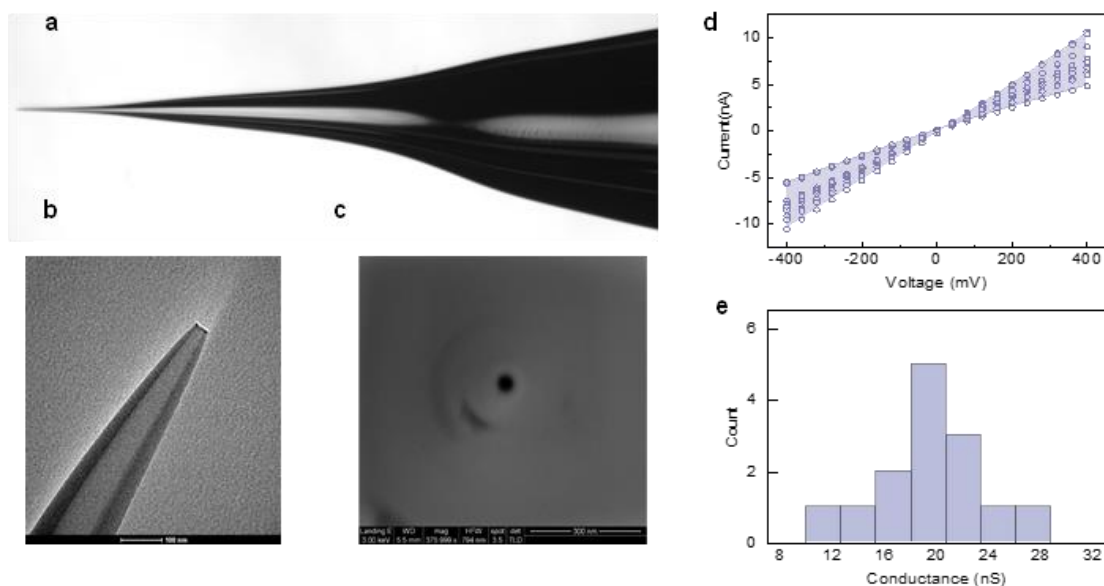
**Table 2-2.** Primer sets for *Pf*-, and *Pv*-specific LAMP amplification

Species	Primer	Sequence (5' → 3')
<i>P. falciparum</i> [52]	F3	CTCCATGTCGTCTCATCGC
	B3c	AACATTTTTTTAGTCCCATGCTAA
	FIP (F1c – F2)	ACCCAGTATATTGATATTGCGTGACAGCCTTGCA ATAAATAATATCTAGC
	BIP(B1 – B2c)	AACTCCAGGCGTTAACCTGTAATGATCTTTACGT TAAGGGC
	LF	CGGTGTGTACAAGGCAACAA
	LB	GTTGAGATGGAAACAGCCGG
<i>P. vivax</i> [53]	F3	GGTACTGGATGGACTTTATAT
	B3c	GGTAATGTTAATAATAGCATTACAG
	FIP (F1c – F2)	CCAGATACTAAAAGACCAACCCACCATTAAGTA CATCACT
	BIP (B1 – B2c)	GCTAGTATTATGTCTTCTTTCACTTAATATACCA AGTGTTAAACC
	LF	GATAACATCTACTGCAACAGG
	LB	CTACTGTAATGCATCTAAGATC



**Glass nanopore fabrication.** The quartz capillaries were cleaned by piranha for 30 minutes to remove any organic contaminants and then repeatedly rinsed with DI water and dried in an oven at 120 °C for 15 min. The capillary was pulled by a laser pipette puller (P-2000, Sutter Instruments, USA) using a two-line program: (1) Heat 750, Filament 5, Velocity 50, Delay 140, and Pull 50; (2) Heat 710, Filament 4, Velocity 30, Delay 155, and Pull 215. This recipe typically produces nanopore size around 10 nm. Despite known batch-to-batch variations in size, the counting method is valid as long as the nanopore can resolve the single molecule event.

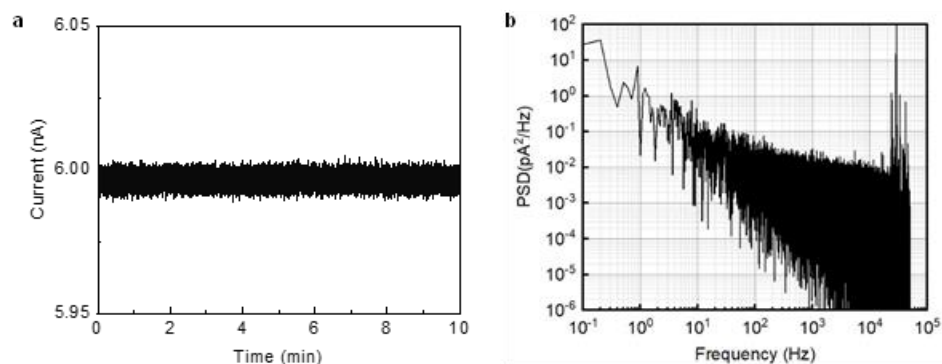
I-V, SEM, and TEM characterization. Microscope image is shown in **Figure 2-1 (a)**. TEM characterization (**Figure 2-1(b)**) was also performed to obtain detailed information for the nanopore geometry. For SEM imaging, 5 nm of Iridium was sputtered onto the nanopore surface to prevent drifts caused by charging. SEM imaging (**Figure 2-1(c)**) was then performed under a working distance between 3 and 5 mm, magnifications of 88,415, beam currents of 2.5 pA, and an acceleration voltage of 3 kV. The nanopore conductance was measured by taking a standard I-V curve in 1M KCl buffered with Tris-EDTA. Typical conductance of the fabricated nanopore is in the range of  $20 \pm 10$  nS (**Figure 2-1 (c-d)**).



**Figure 2-1.** (a) Microscope, (b) TEM and (c) SEM image of the nanopipette. I-V characterization for all glass nanopore used. (d) Current-voltage curves for the glass nanopore in 1 M KCl with Tris-EDTA-buffer solution. (e) Conductance distribution of the glass nanopores. The nanopore size clearly varies from batch to batch. Typical conductance of the fabricated nanopore is in the range of  $20 \pm 10$  nS.

**Electrical recording and data analysis.** A constant voltage was applied across the nanopore constriction with a 6363 DAQ card (National Instruments, USA). The ionic current traces were recorded by an amplifier (Axopatch 200B, Molecular Device, USA). The analog output of the amplifier was sampled with the 6363 DAQ card and a customized data acquisition software (LabVIEW). The sampling rate for the measurement was 100 kHz. The signal was low-pass filtered at 10 kHz. The measurement system was inside a home-made Faraday cage to shield the environment noise. We also analyzed the noise performance of the ionic current measurement (**Figure 2-2 (a)**). Typical RMS noise in our experiments is around 4.2 pA, low enough to distinguish the typical single molecule events with dip magnitude  $>10$  pA. Our noise performance (**Figure 2-2 (b)**) was comparable to these in the previous studies [47]. A custom-built MATLAB

(MathWorks) program was developed to reconstruct the sensing data and to analyze the event rate, current dip duration, and depth for the single molecule events.



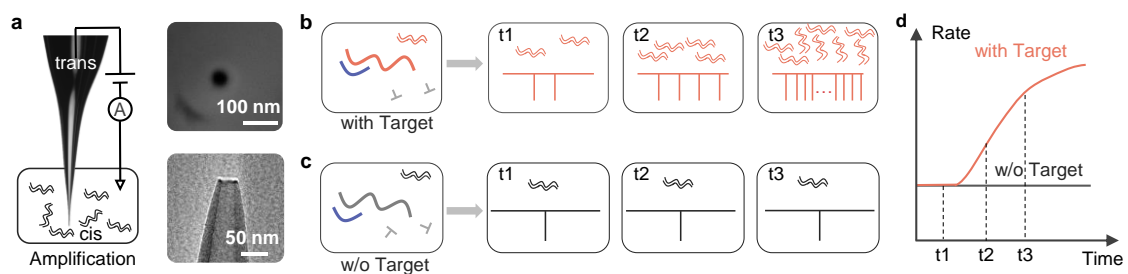
**Figure 2-2.** Typical noise performance of the glass nanopore sensor in 1 M KCl Tris-EDTA buffer at 400 mV. (a) Current traces, the RMS noise was around 4.2 pA, (b) Power spectrum density for the ionic current signal.

**Nanopore-LAMP experiment.** The LAMP master mix (24  $\mu$ l) and the target template (1  $\mu$ l) was dispensed into the PCR tube, with an additional 25  $\mu$ l mineral oil added to prevent evaporation and cross-contamination. The PCR tube was placed in a dry block incubator preheated at 65°C. The LAMP reaction was terminated at different times by heating at 95°C for 5 min. The product solution was adjusted to 1 M salt concentration for nanopore measurement. The same glass nanopore was used for all samples amplified at various times. To ensure the signal observed was not due to spurious amplification, we performed the gel electrophoresis in 2% agarose after the amplification.

### 2.3. Working principle

As one of the resistive pulse sensors, nanopores were usually used for two purposes: size determination [43, 54] and counting [55-57]. While analyte sizing is sensitive to the pore size, analyte counting is less so. Our approach used the glass nanopore in its simplest function of

counting to quantify the amplicon abundance, which was conventionally quantified by the fluorescence sensing using probes like TaqMan or intercalating dye like SYBR Green. Note that batch-to-batch precise glass nanopore size control is not required in the counting mode as long as it is able to resolve the single molecule event. The glass nanopore used in our experiment is typically 10 nm in diameter. Existing theory [58] and experiment [56] have shown that the DNA molar concentration ( $C$  in mol/m<sup>3</sup>) is related to the event rate ( $R$  in s<sup>-1</sup>). Therefore, it is possible to infer the amplicon concentration by measuring the event rate. Note that we used the term ‘event rate’ rather than ‘capture rate’ to describe the counting rate of molecules, because ‘capture rate’ could refer to concentration normalized rate [58, 59] in previous studies (Note S1). Figure 2-3a shows the schematic diagram of the experimental setup with conically shaped glass nanopore as the single molecule counting device. The amplification reaction is sealed with mineral oil to avoid evaporation and cross-contamination. For a positive reaction (Figure 2-3b), the increase of amplicons manifests itself as the increase of the event rate. For the negative reaction (Figure 2-3c), the event rate remains unchanged or undetectable. The rate determined at certain time spots during the amplification is an electronic measurement of the corresponding amplicon concentrations (Figure 2-3d).

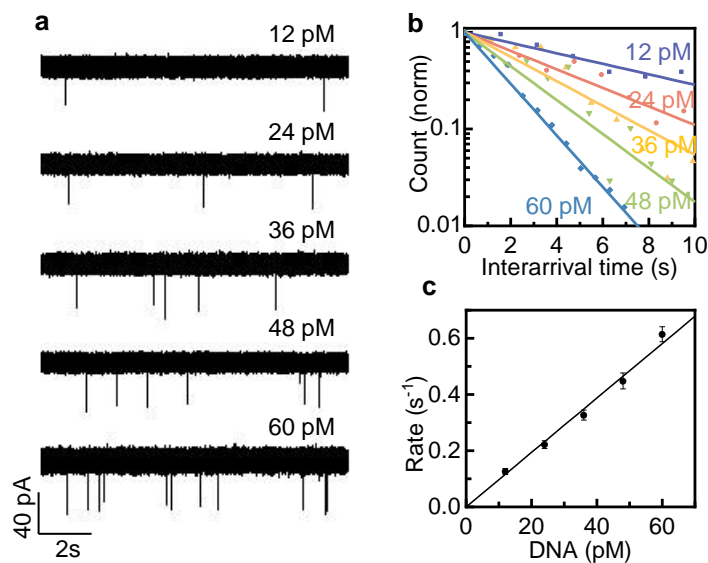


**Figure 2-3.** Illustration of the working principle of nanopore counting of amplicons. (a) Schematic measurement setup as well as the SEM and TEM of the glass nanopore. Amplicons are electrophoretically driven through the glass nanopore one by one, resulting in discernible events of the ionic current blockade. The event rate is proportional to the amplicon concentration. (b) Events in a positive target case. (c) Events in a negative target case. (d) Schematic event rate as a function of amplification time (or cycle).

## 2.4. Result and discussion

### 2.4.1. DNA Concentration as a function of event rate

Before the amplification experiment, we first addressed whether the single molecule counting rate could be used as a reliable readout for DNA concentration in our glass nanopores. We performed studies on 5 kbp DNAs with a serial of concentrations ranging from 12-60 pM. A quick eyeball on the current time traces in **Figure 2-4a** shows that the inter-arrival time between two events become shorter when concentration increases; in other words, the event rate is faster at higher concentration. The extracted inter-arrival time distribution shows a remarkable exponential distribution for each concentration (**Figure 2-4b**), indicating a Poisson process, consistent with previous observations in the silicon nitride nanopore [60]. Each concentration case was then fitted with an exponential distribution,  $P(t) = \lambda e^{-\lambda t}$ , where  $\lambda$  is the expected single-molecule event rate. **Figure 2-4c** shows the single-molecule event rate as a function of the DNA concentrations. Note that a limited concentration range was probed in **Figure 2-4**. The average molecular distance ranges from 3  $\mu\text{m}$  to 5.2  $\mu\text{m}$  and therefore interactions between molecules are negligible for the following rational. In a 1 Molar solution, there are  $6 \times 10^{23}$  molecules per liter of liquid, or 0.6 molecules per  $\text{nm}^3$ . Therefore, the volume per molecule is  $1.66 \text{ nm}^3$  at 1 M. For any molar concentration  $C$ , the volume per molecule is  $1.66 \text{ nm}^3/C$ . Take the cubic root of this volume per molecule, and we can obtain the average separation of molecules as  $d = 1.18/C^{1/3}$ , where  $C$  is in molar and  $d$  is in nanometer. The average molecular distance at 12 pM is thus estimated to be 5.2  $\mu\text{m}$ . Similarly, the average molecular distance at 60 pM is estimated to be 3  $\mu\text{m}$ . As a result, molecule concentration is indeed expected to be linearly related to the event rate [58].

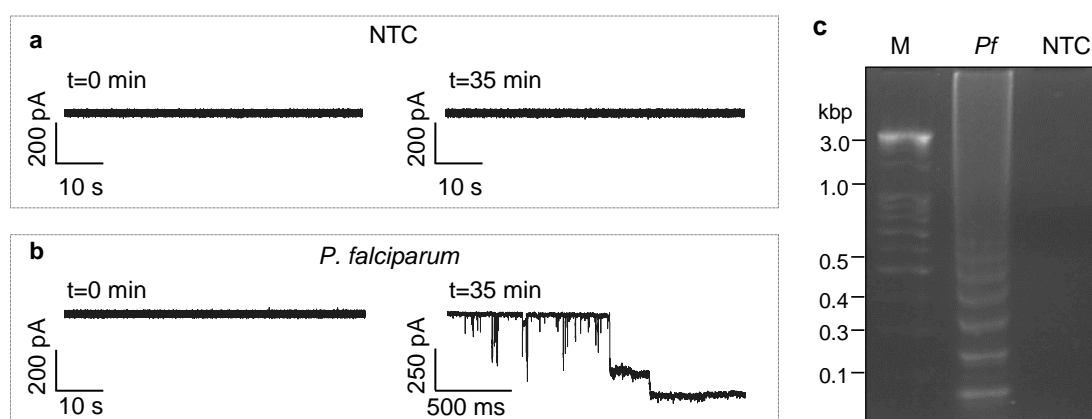


**Figure 2-4.** Continuous recordings of current trace under 500 mV bias with 5 kbp-DNA through glass nanopore at 1M KCl in Tris-EDTA-buffer solution. (a) Segments of the current trace at different DNA concentrations. (b) The normalized probability distribution of the inter-arrival time at different concentrations, with corresponding exponential fits. (c) The average event rate as a function of DNA concentration, showing a linear dependence ( $R^2 = 0.985$ ).

#### 2.4.2. Concept validation

As an alternative to thermal-cycling based PCR method, isothermal assays such as LAMP is very promising for developing a sensitive molecular test in resource-limited settings [48, 49, 61, 62]. We set out to test if the glass nanopore could detect the end-product of the LAMP reaction. First, we tested the no-template control (NTC) sample when it was freshly prepared ( $t=0$  min) and after 35 min of LAMP reaction. As shown in **Figure 2-5a**, no events were observed for 60 s of recording. This confirmed the LAMP reagents, such as deoxynucleotide triphosphates (dNTPs), polymerase enzyme and primers were not detectable by the glass nanopore. This is likely because the 10 nm-sized nanopore is too big for these background targets. After confirming the background master mix did not produce measurable events, we continued to test the positive control sample with *Plasmodium falciparum* genomic DNA. As shown in **Figure 2-5 b**, no detectable events were

noticeable before the LAMP reaction ( $t=0$  min), further confirming the LAMP master mix does not interfere with the measurement. However, after 35 min of LAMP reaction of this positive control sample, clear events were immediately observable in the first second of measurement. **Figure 2-5c** shows the gel image of the final LAMP products for both positive and negative controls. The sharp contrast in the event rate between **Figure 2-5a** and **Figure 2-5b** confirms the glass nanopore is able to detect the LAMP end products qualitatively.



**Figure 2-5.** Concept validation of nanopore counting of amplicons. Time traces for (a) negative no-template control (NTC), and (b) positive control before and after the 35 min LAMP reaction. The clogging issue was observed in the positive controls. (c) Gel electrophoresis image of the LAMP products (2% agarose gel).

### 2.4.3. Resolving the pore-clogging by voltage cycling scheme

Nanopore clogging is a common issue during long-term measurements. In testing the end product of the positive control sample (**Figure 2-5b**), two abrupt current drops sequential occurred and the current stopped returning to its baseline after only a few seconds of the continuous current recording. A careful examination of the current time trace reveals that the event rate is about  $68 \text{ s}^{-1}$  before the drop, much higher than the rate shown in, indicating the amplicon concentration is very high. This is not surprising because the number of amplicons grows significantly during the LAMP

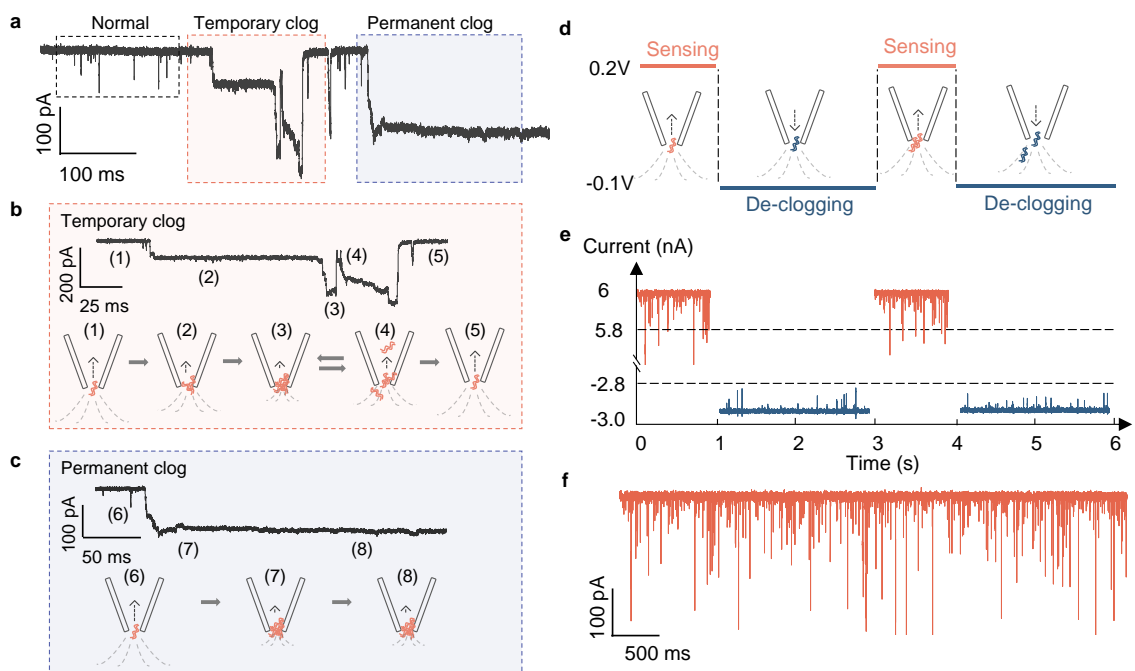
reaction. At this high concentration, the DNAs are highly likely to be jammed near the nanopore entrance, leading to partial or full clogging of the nanopore. This jamming effect [63] caused a potential problem for reliable event rate determination for long-term measurement.

Another more representative current time trace from the LAMP end product was shown in **Figure 2-6a**, which contains a full picture of different translocation scenarios. The normal DNA translocation through the nanopore usually takes about 500  $\mu$ s. The temporary clog case is expanded in **Figure 2-6b**. Segment 1 has the baseline current corresponding to the open nanopore condition. The ionic current shifts down by around 50 pA for segment 2, indicating a partial clogging of the nanopore. The baseline current drops another 100 pA in segment 3 with more DNAs coming at the nanopore and get jammed. However, these temporary jams eventually get cleared after some time, and the baseline current returns to its open-pore value (segment 5). In contrast, the permanent clog case is magnified in **Figure 2-6c**, in which the baseline current stopped coming back to its open-pore level.

Both temporary and permanent clog issues will negatively impact the nanopore's capability to count the amplicons continuously. To resolve this issue, we developed a voltage cycling scheme for long-term recording (**Figure 2-6d**), similar to a previously reported approach [64]. The duration of the positively applied voltage (200 mV) that drives the DNA into the glass nanopore was typically limited to 1 s, in which the single molecule events were recorded. This was followed by a de-clogging step using a negative voltage (-100 mV) with a typical duration of 2 s to allow DNAs to drift in reverse direction and to re-randomize via diffusion. **Figure 2-6e** shows the current time trace in two consecutive voltage cycles on the same LAMP product. **Figure 2-6f** shows the overlay of the current traces over 5 s with a total of 487 events. As shown, the reconstructed sensing current shows no baseline shift, which suggests the voltage cycling scheme can resolve the clogging issue and is suitable for long-time measurement. It is noteworthy that under the voltage cycling scheme,



we did not observe any permanent clog issue for all hour-long experiments we performed. All the following data presented was generated under this scheme after reconstruction.



**Figure 2-6.** Resolving the nanopore clogging by voltage cycling scheme. (a) A representative current trace showing normal, temporary clog and permanent clog. (b) Expanded view of the temporary clog. (c) Expanded view of the permanent clog. (d) Illustration of the voltage cycling scheme. The voltage is cycled between 1 s of 200 mV for sensing and 2 s of -100 mV for de-clogging. (e) A typical current trace using the voltage cycling scheme. (f) Reconstructed 5 s current trace by sequentially combining the current obtained under the 200 mV sensing voltage. A total of 487 events could be identified without clogging issue.

#### 2.4.4. Probing LAMP reaction dynamics

After establishing a reliable approach for rate measurement, we tested if the nanopore counting could resolve the LAMP dynamics. Using the *P. falciparum* genomic DNA, LAMP assays were performed for a duration ranging from 10 min to 37.5 min at 65°C, the product of which is counted using the same glass nanopore. The event rate at 95% confidence interval was calculated as  $(n \pm 1.96(n)^{1/2})/T$  since these events follow the Poisson process [35, 65], where  $n$  is the number of events

observed, and  $T$  is the total elapsed time. The relative uncertainty of inferring the rate  $R$  is proportional to  $n^{-1/2}$ . For each reaction time, we counted at least 150 events to ensure measurement uncertainty  $<8\%$ . Figure 2-7 Shows all the for all-time current traces. **Figure 2-8a** shows segments of the current time trace for each reaction time It is evident that the event rate increases with extended reaction time (note the scale difference among the plots).

**Figure 2-8b** shows the extracted event rate as a function of LAMP reaction time. The rate shows more than 3 orders of magnitude increase when the reaction time goes from 10 min to 37.5 min. The event rate (which is a readout of the LAMP amplicon quantities) versus the reaction time can be fitted remarkably well with a logistic growth model. As we know, LAMP reaction is an auto-cycling process which involves multiple pathways for gene replication, and this reaction amplifies the DNA from the single copy to a billion copies in less an hour. The logistic growth model is widely used to describe the population's growth rate decreases as population size approaches its carrying capacity imposed by limited resources [66]. At the early phase, the number of amplicons exponentially increases with time. However, as the reaction goes, it starts to be limited by remaining reagents in the master reaction mix (dNTPs, primers, and enzymes). The rate of amplicon synthesis will eventually cease. The growth rate as the function of time can be express as

$$\frac{dN(t)}{dt} = \beta N(t)(\Omega - N(t)) \quad (2-1)$$

in which  $N(t)$  is the number of the amplicons at time  $t$ ,  $b$  is the constant rate of growth,  $\Omega$  is the saturation level of amplicon numbers. This means the growth rate is affected by both the existing amplicon numbers  $N(t)$  and the remaining resources  $\Omega - N(t)$ . The solution to Eq. 1 can be written as a 4 parameter logistic function [67, 68]

$$N(t) = A + \frac{\Omega - A}{1 + e^{-\beta(t-t_0)}} \quad (22)$$

in which  $A$  is the lower bound of the amplicon numbers,  $t_0$  is the time at the maximum growth rate. In the nanopore digital counting, the event rate  $R$  has a linear relationship with the concentration as

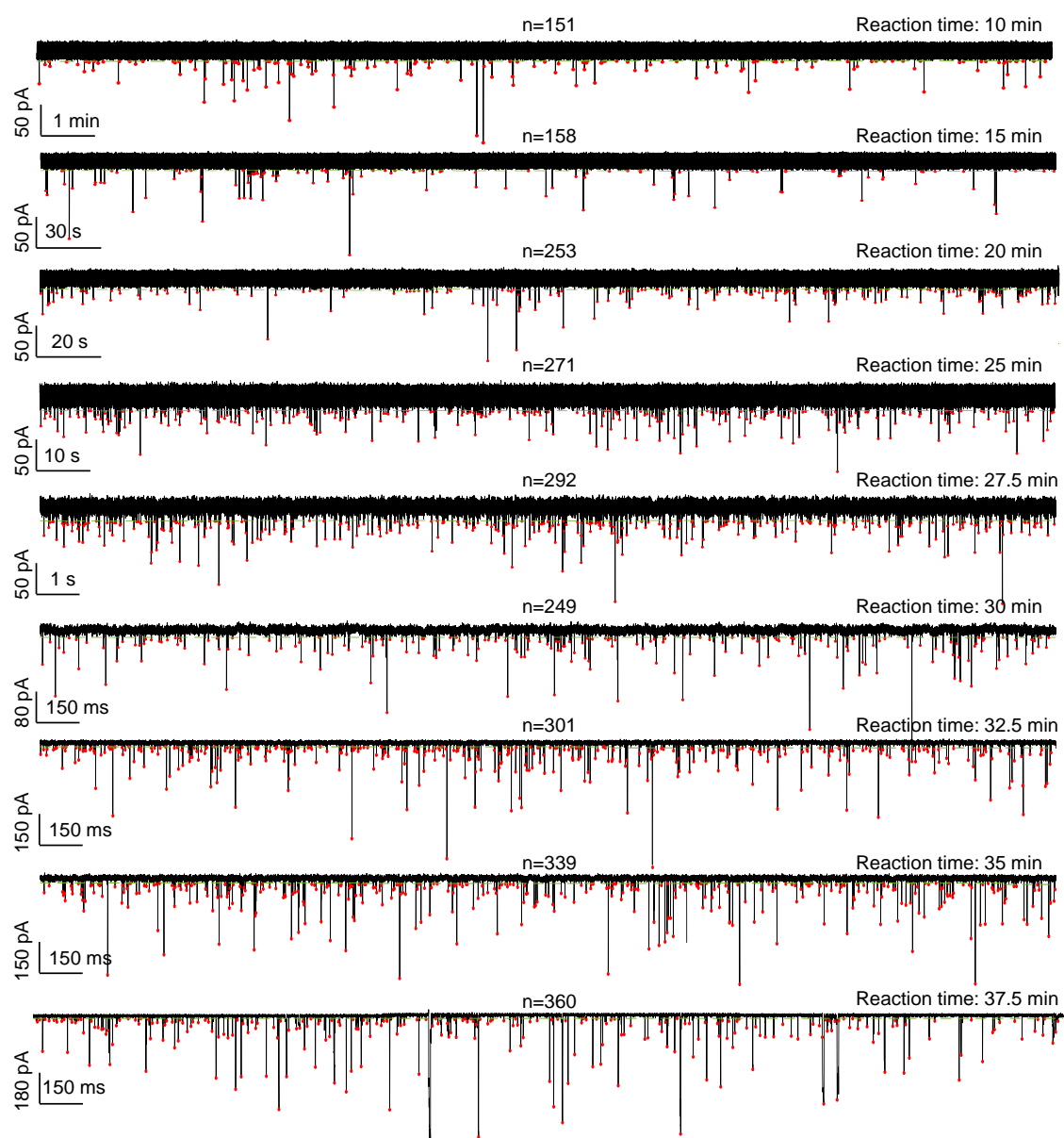
$$R = \alpha N(t)/V_{Reaction} \quad (2-3)$$

where  $\alpha = 2\pi D r^*$ , and  $r^*$  is the capture radius which contains information about the molecular diffusion coefficient, the nanopore geometry and the experimentally applied voltage, and  $V_{Reaction}$  (with unit  $m^3$ ) is the LAMP mixture volume, which is 25  $\mu l$  in our experiment. Combining Eq. 2 and Eq. 3, the event rate can be written as:

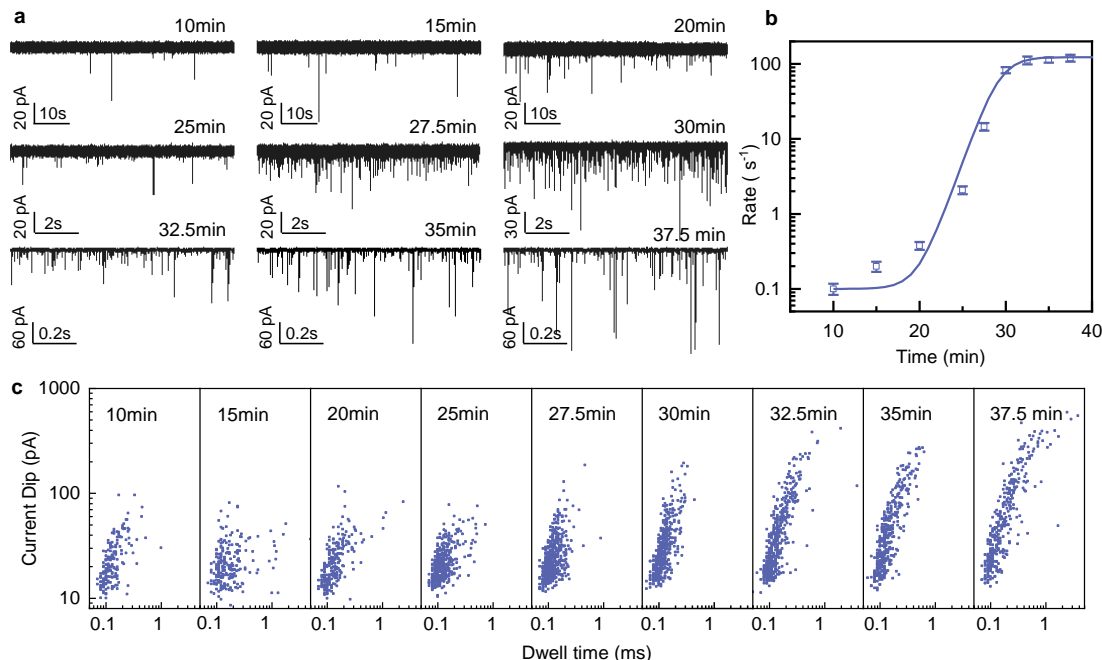
$$R(t) = R_L + \frac{R_H - R_L}{1 + e^{-\beta(t-t_0)}} \quad (2-4)$$

in which  $R_L = \alpha A/V_{Reaction}$  is the lower bound of the event rate.  $R_H = \alpha \Omega/V_{Reaction}$  is the saturation level of the event rate. Eq. 4 combines both the nanopore characteristics and the LAMP amplification dynamics and is used for fitting the amplification curve in nanopore counting. The agreement to the logistic growth model suggests the LAMP cycling reaction could not sustain a constant exponential growth and is indeed subject to the limited number of dNTPs, polymerase enzymes and primers available in the 25  $\mu l$  LAMP reaction mix.

Another interesting feature observed in **Figure 2-8a** is the widely distributed current dip magnitude and dwell time for single molecule events. **Figure 2-8c** shows the current dip-dwell time scatter plot at each LAMP reaction time. As the amplification time increase, a substantial increase of population with higher current dip and longer dwell time was observed, indicating longer DNAs are produced when the reaction continues. This is indeed expected for the LAMP reaction, in which the final product obtained is a mixture of stem-loop DNA with various stem lengths and various cauliflower-like structures with multiple loops. The structures are formed by annealing between alternatively inverted repeats of the target sequence in the same strand [48, 49].



**Figure 2-7.** Summary of all current time traces obtained after indicated LAMP reaction time (the Pf genomic DNAs concentration is the 100 ng/ $\mu$ l). The green dash line is the noise threshold and the red dots represent the peak location of the current dip. (n: total number of translocation events detected). Note the differences in time scale.

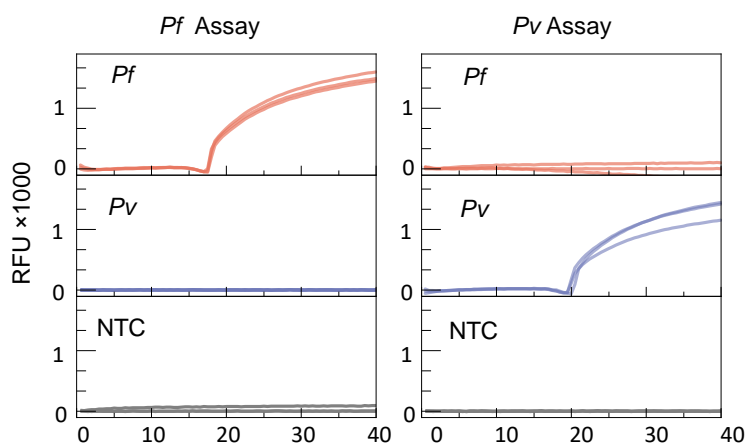


**Figure 2-8.** Nanopore counting to probing the LAMP reaction dynamics. (a) Current traces at various amplification times. (b) The event rate as a function of the amplification time. The event rate increased exponentially before reaching a saturated level. The solid line is fitting to the logistic growth model ( $RL=0.1s^{-1}$ ,  $RH=123.2s^{-1}$ ,  $\beta=0.75min^{-1}$  and  $t_0=29.2$  min). (c) Scatter plots showing current dip magnitude vs. dwell time at various reaction times.

#### 2.4.5. Qualitative testing

To demonstrate the potential utility of the LAMP-coupled nanopore counting approach for qualitative (yes/no) specific nucleic acid testing, we examined two of the most spread species of malaria: *P. falciparum* (*Pf*) and *P. vivax* (*Pv*). Before the nanopore experiment, we first validated the *Pf*- and *Pv*-specific LAMP primer sets in a benchtop real-time PCR instrument (Bio-Rad (**Figure 2-9**)). Each species-specific assay was then tested with three different types of samples (*Pf*, *Pv*, and *NTC*). We used the nanopore to analyze the end product of the LAMP assay after 35 min of reaction at 65°C. **Figure 2-10a** and **Figure 2-10b** show the resulting current time traces for *Pf*-specific assay and *Pv*-specific assay, respectively. The events with a rate of  $31.2 s^{-1}$  (*Pf* in *Pf*-specific assay) and  $8.5 s^{-1}$  (*Pv* in *Pv*-specific assay) were observed when the assays match with the intended

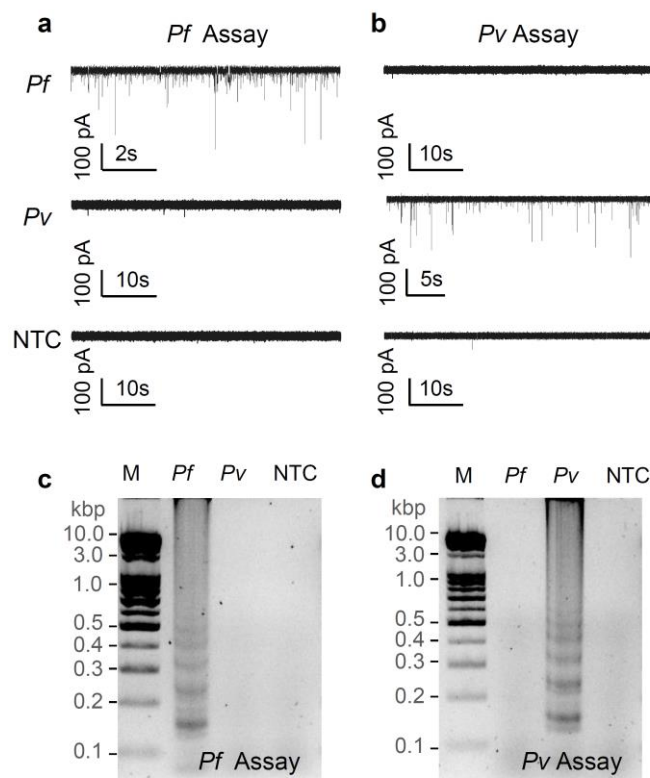
species. No cross-reactivity was observed. To further validate that the signal observed was not due to the random noise. We performed gel electrophoresis in 2% agarose gel. As shown in **Figure 2-10c** and **Figure 2-10d**, clear ladder-like patterns with multiple bands of different molecular sizes were observed due to the stem-loop DNA structures with several inverted repeats within LAMP amplicons[48, 49]. In contrast, no bands were observed in the non-specific and NTC reaction.



**Figure 2-9.** Validation of the *Pf* and *Pv* LAMP assays using *Pf* and *Pv* genomic DNA in benchtop real-time PCR machine (NTC: no template control).

#### 2.4.6. Quantitative testing

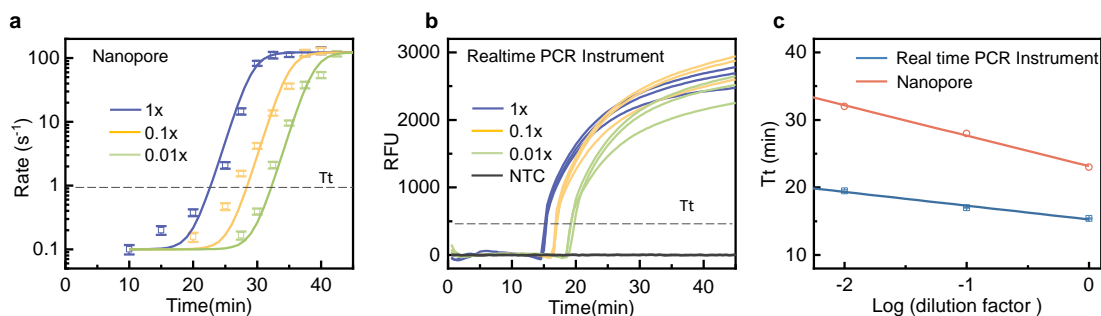
To evaluate the potential quantitative application of the nanopore counting platform, we performed the nanopore-LAMP assay on the mitochondrial gene by using a 10-fold serial dilution of purified *P. falciparum* genomic DNA. The nanopore-LAMP performance (**Figure 2-11a**) is benchmarked to the tube-based quantitative LAMP (qLAMP, **Figure 2-11b**) on a benchtop real-time PCR instrument using calcein as an indicator. Both the fluorescence-based method and the nanopore method show the expected right-shift of the amplification curve when reducing the gene copy numbers. The event rate data at different time spots were summarized in Table 2-3. In addition, as



**Figure 2-10.** Qualitative specific nucleic acid testing using the nanopore-LAMP. (a) Current traces obtained from nanopore reading for Pf-specific assay, and (b) for Pv-specific assay. The event rate difference between the positive and the negative is evident. (c) Gel electrophoresis image (2% agarose gel) for Pf-specific assay and, (d) for Pv-specific assay.

shown in **Figure 2-11a**, the event rate results from all diluted samples tested by the nanopore can be fitted remarkably well by the logistic growth model (with all  $R^2 > 0.95$ , Table 2-3). **Figure 2-11c** shows the extracted standard curves from both the nanopore and fluorescence methods. The threshold time is determined by the time corresponding to the reading of 500 RFU in the fluorescence method and  $1 \text{ s}^{-1}$  in the nanopore method, respectively. The amplification over a range of serially diluted DNA samples showed excellent linearity in both methods ( $R^2=0.98$  for fluorescence method and  $R^2=0.99$  for nanopore method). The linearity in the nanopore method suggests it could be used for quantitative analysis of DNA. The different slope between the

nanopore-LAMP and the benchtop thermal cycler-based LAMP is likely due to setup difference in the thermal and detection dynamics.



**Figure 2-11.** Comparison between the nanopore method and fluorescence-based method. (a) The results acquired from the nanopore detection. The solid lines were fittings to the logistic function (with fitting parameters summarized in Table S2). 1X, 0.1X, and 0.01X denote the dilution factors of the templates. 1× is equivalent to 100 ng/μl *Pf* genomic DNAs. (b) Amplification curves obtained from the fluorescence method using benchtop real-time PCR machine. (NTC: no template controls). (c) Standard curves extracted from the nanopore platform and the fluorescence platform. The linearity in the nanopore method suggests it could be used for quantitative analysis of DNA.

**Table 2-3.** Parameter values for fitting the logistic function fit in Figure 2-8

	$R_L (s^{-1})$	$R_H (s^{-1})$	$\beta (min^{-1})$	$t_0 (min)$	Fitting $R^2$
1X	0.1	123.2	0.75	29.2	0.99
0.1X	0.1	123.2	0.75	35.3	0.97
0.01X	0.1	123.2	0.75	39.8	0.95

#### 2.4.7. Limit of detection considerations

While the limit of detection (LoD) was not experimentally explored as it is highly assay dependent, the LoD is impacted by two factors in nanopore counting. The first is the false positive rate when no amplicons exist, similar to the dark count rate in the single photon counters [69]. The false detection events are due to the noise in the testing apparatus as well as the background reagents. In



our experiment, the false positive rate when testing the NTC sample is  $<0.01$  during a 60 min test. The second factor is the Poisson noise during the counting. Since the relative uncertainty of inferring the rate is proportional to  $n^{-1/2}$ , a large enough event number ( $n$ ) should be recorded to establish a sufficiently robust statistical basis [70]. Assuming a minimal event number  $n$  and a practical measurement time of  $T$ , a minimal event rate  $n/T$  is required, corresponding to the lower bound of detectable amplicons. In our study, we use  $0.1 \text{ s}^{-1}$  as minimal event rate so that we can obtain at least 10 events during a 100 s-long test. Future work could incorporate multiple parallel nanopores[71, 72] to improve the time resolution towards the real-time analysis.

## 2.5. Summary

In summary, our findings demonstrated the effectiveness of using single-molecule-counting glass nanopore to probe the number of specifically replicated amplicons from the loop-mediated isothermal amplification. We show that the nanopore counting approach can capture the DNA replication dynamics in the LAMP and has the potential to be used in a qualitative as well as a quantitative nucleic acid test. The LAMP-coupled glass nanopore counting strategy addressed common challenges in solid-state nanopore sensors regarding the batch-to-batch nanopore size variation, the specificity, and the prolonged sensor response time at low analyte concentrations. By keeping the nanopore as simple as possible and coding the specificity information into the molecule numbers, the LAMP-coupled glass nanopore counting method provides a promising optics-free method for highly sensitive and specific nucleic acid testing at the point of care. While this work focused on the LAMP and the glass nanopore, we believe the amplification-coupled nanopore counting approach could be well extended to other molecule replication strategies and other solid-state nanopore types.

### **Chapter 3 Rapid Detection of SARS-CoV-2 by RT-LAMP Coupled Solid-State Nanopores**

In chapter 2, I demonstrated the basic concept of using LAMP-coupled nanopore sensor for malaria nucleic acid test, but not yet studied quantitatively of this method. In this chapter, we dived into the RT-LAMP coupled glass nanopore digital counting method, and quantitatively studied the analytically sensitivity (Limit of detection), analytically specificity, diagnostic sensitivity, and diagnostic specificity and well as diagnostic ability. Here the RT-LAMP assays targeting nucleocapsid (N) genes of SARS-CoV-2 was used in the system. The RT-LAMP amplicons were digitally counted by glass nanopore and benchmarked the event rate with a threshold. Due to its intrinsic single molecule sensitivity, nanopore sensors could capture the amplification dynamics more rapidly (quick time to positive). We validated this method with both spiked saliva samples and COVID-19 clinical nasopharyngeal swab samples. With the spiked saliva sample, our method shows the about 65 cp/μl limit of detection and 100% analytical specificity. With 127 clinical samples and RT-PCR as the gold standard, our nanopore platform was able to detect SARS-CoV-2 with 98% diagnostic sensitivity, and 92% diagnostic specificity. With its integration capability, the electronic nanopore digital counting platform has significant potential to provide a rapid, sensitive, and specific point-of-care assay for SARS-CoV-2.

### 3.1. Introduction

Coronaviruses are enveloped positive-sense RNA viruses, which are commonly associated with acute respiratory infections in humans. In late December 2019, several local health facilities reported patients with pneumonia of unknown causes in Wuhan, Hubei Province, China [12]. The causative pathogen has been identified as a novel enveloped RNA beta coronavirus. Given the similarity to the previously isolated severe acute respiratory syndrome coronavirus (SARS-CoV), the new virus has been named SARS-CoV-2. This new virus causes coronavirus disease 2019 (COVID-19), and it was rapidly announced as a public health emergency of international concern by the World Health Organization (WHO). As of August 2021, there are a total of 198,778,175 confirmed cases, and 4,235,559 deaths of SARS-CoV-2 reported globally [73]. In this pandemic of SARS-CoV-2, accessible, early, and accurate diagnosis is crucial to facilitate robust public health surveillance and rapid testing. The current gold-standard technique for SARS-CoV-2 testing is the reverse transcription-polymerase chain reaction (RT-PCR) [74]. Despite its high sensitivity and specificity, laboratory-based RT-PCR requires highly trained personnel, dedicated facilities, and instrumentations, thus limiting the testing capacity. To enhance the test accessibility, isothermal amplification techniques such as reverse transcription loop-mediated isothermal amplification (RT-LAMP) is widely studied as alternatives for COVID-19 testing [21, 75]. The isothermal method has great potential as a point-of-care tool because it is a rapid, sensitive, and specific technique. During the early outbreak phase of the COVID-19 pandemic, a significant research effort focused on designing, validating, optimizing the RT-LAMP primers [18, 76]. These efforts soon expanded to the scope of exploring alternative sample specimens [77-79] and simplifying the sample purification [22, 80]. In addition, the CRISPR based detection has been incorporated with the RT-LAMP to improve its specificity performances [81], and the high-throughput sequencing

has been incorporated with the RT-LAMP (LAMP-sequencing) to facilitate population-level of usage [20].

The results of the RT-LAMP amplification are often read out using different optical methods, such as changes in turbidity caused by magnesium pyrophosphate precipitate [13], changes in fluorescence using dyes [14-16], colorimetric pH indicators [17, 18], or gel electrophoresis followed by UV detection [19]. Each of these methods would require a minimum concentration of the signaling reporters ( $c_{min}$ ) for the readout system to distinguish between positives and negatives. Depending on different readout systems (*e.g.*, naked eye [20] versus highly sensitive fluorescence detector [21, 22]), the  $c_{min}$  could range from mM to nM. This required minimal signaling reporter concentration can be linked to the time to positive (TTP) as  $c_{min} = TTP \times v_r$ , in which  $v_r$  is the average reaction rate of the assay. It is evident that reducing the detection  $c_{min}$  is preferred towards quick time to positive. In this regard, the intrinsic single-molecule sensitivity of nanopore sensors [23, 24] is highly intriguing since it enables a significantly reduced  $c_{min}$  and thus reduce the time required for making the positive/negative call. Existing works on nanopores have demonstrated that nanopores can easily capture the analyte at the pM range [23, 82]. Our previous work has demonstrated a LAMP-coupled nanopore sensor for malaria nucleic acid test [27]. The integration and miniaturization potential of the label-free, electronics-based nanopore sensors could open a new avenue for enhancing the accessibility of the molecular testing at the point of care.

In this study, we report an RT-LAMP coupled nanopore platform for rapid detection of SARS-CoV-2. We compared the time to positive and sensitivity performances of two one-pot RT-LAMP assays targeting the nucleocapsid and envelop genes. For qualitative positive/negative classification of a testing sample, the nanopore sensor was used to measure the amplicon size and concentration by the digital counting method. Thanks to its intrinsic single molecule sensitivity, the nanopore sensor could make a faster positive/negative call than bulk optical methods. We

validated this method with both spiked saliva samples and COVID-19 clinical nasopharyngeal swab samples. With 127 clinical samples and RT-PCR as the gold standard, our nanopore platform was able to detect SARS-CoV-2 with 98% diagnostic sensitivity, and 92% diagnostic specificity. We believe the RT-LAMP coupled electronic nanopore digital counting platform has significant potential to provide a rapid, sensitive, and specific detection of SARS-CoV-2.

## **3.2. Material and method**

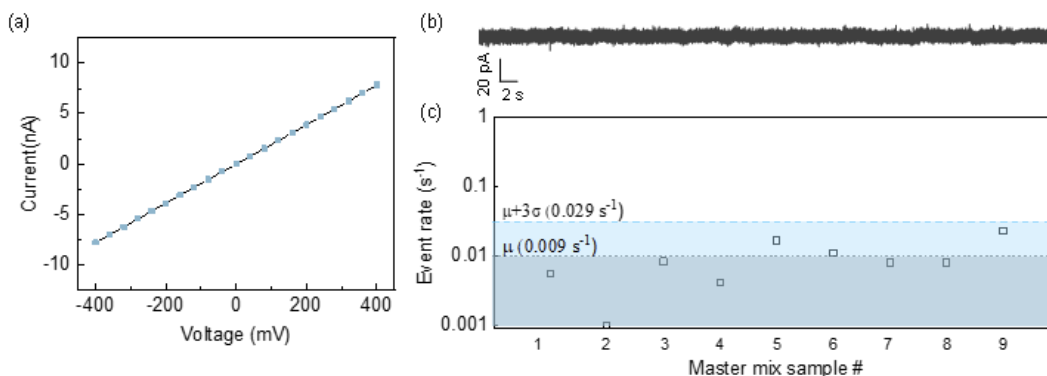
### **3.2.1. Materials and chemicals**

Quartz capillary with inner and outer diameter of 0.5 and 1 mm was purchased from Sutter Instrument. Pipette holder (QSW-T10N) and 0.2 mm Ag wire was purchased from Warner Instruments. Micro-injector with 34 gauge was purchased from World Precision Instruments. KCl and Tris-EDTA-buffer solution (pH 8.0) were purchased from Sigma-Aldrich. All solutions were filtered with a 0.2  $\mu\text{m}$  syringe filter (Whatman). Mineral oil was purchased from Sigma-Aldrich. Heat-inactivated SARS-CoV-2 (ATCC® VR-1986HK™) RNA was purchased from ATCC. Synthetic human coronavirus 229E RNA (103011), NL63 RNA (103012) and 229E RNA (103013) were purchased from Twist Bioscience. QIAamp Viral RNA Kit was purchased from Qiagen. ThermoFisher MagMAX Viral/Pathogen Nucleic Acid Isolation Kit was purchased from ThermoFisher.

### **3.2.2. Glass nanopore fabrication and characterization**

The quartz capillaries with inner and outer diameters of 0.5 and 1 mm were first cleaned by piranha for 30 minutes to remove any organic contaminants, then repeatedly rinsed with DI water and dried

in an oven at 100 °C for 15 min. A laser pipette puller (P-2000, Sutter Instruments, USA) was used to fabricate the nanopore using a two-line program: (1) Heat 750, Filament 5, Velocity 50, Delay 140, and Pull 50; (2) Heat 715, Filament 4, Velocity 30, Delay 145, and Pull 225. This recipe typically produces nanopore size around 10 nm (**Figure 3-1**).



**Figure 3-1.** (a) The glass nanopores were characterized using an I-V scan in 1 M KCl, corresponding to a nanopore with about 10 nm in diameter. (b) Representative current time traces of master mix (negative control) samples. (c) Event rate of 9 negative control samples. The mean ( $\mu$ ) is 0.009 s<sup>-1</sup>, standard deviation ( $\sigma$ ) is 0.007 s<sup>-1</sup>, and  $\mu+3\sigma$  was 0.029 s<sup>-1</sup>.

### 3.2.3. Nanopore sensing and data analysis

The glass nanopore was held by a pipette holder and immersed in a PCR tube, forming the *cis* and *trans* chambers. Micro-injector with 34 gauge was used to inject the solution into the nanopore, and both sides of the chambers were filled with 1 M KCl. Two Ag/AgCl electrodes were inserted into the KCl solution. A typical voltage of 200 mV was applied across the nanopore constriction with a 6363 DAQ card (National Instruments, USA). The ionic current traces were amplified by Axopatch 200B (Molecular Device, USA), low-pass filtered at 10 kHz, and digitalized by the 6363 DAQ. The data was acquired by a customized LabVIEW software (National Instruments, USA). The nanopore measurement system was inside a homemade Faraday cage to shield the

environmental noise. A custom-built MATLAB (MathWorks, USA) program was developed to analyze the current drop, duration time, ECD, and event rate.

### 3.2.4. SARS-CoV-2 RT-PCR

We used the United States CDC primer sets targeting the N1 region of the SARS-CoV-2 (Table 3-1). The 20  $\mu$ l of the RT-PCR reaction mix consists of 5  $\mu$ l of the RNA template, 1.5  $\mu$ l of primer mix (50  $\mu$ M forward primer, 50  $\mu$ M reverse primer, 20  $\mu$ M probes), 10  $\mu$ l of qScript™ XLT One-Step RT-qPCR Tough Mix (2X), and 3.5  $\mu$ l of H<sub>2</sub>O. The RT-PCR process was performed for 45 cycles in the Bio-Rad CFX96 Real-Time PCR system. Each cycle consists of 3 seconds denaturation step at 95 °C and 30 seconds annealing step at 55 °C.

**Table 3-1.** RT- PCR primer sets targeting N1 regions of SARS-Cov-2

Primer	Sequence
2019-nCoV-N1-F	5'-GAC CCC AAA ATC AGC GAA AT-3'
2019-nCoV-N1-R	5'-TCT GGT TAC TGC CAG TTG AAT CTG-3'
2019-nCoV-N1-P	5-FAM-ACC CCG CAT TAC GTT TGG TGG ACC-BHQ1-3'

### 3.2.5. SARS-CoV-2 RT-LAMP

The total volume of the RT-LAMP assays contains a 24  $\mu$ l master mix and 1  $\mu$ l RNA sample. The master mix includes isothermal buffer, PCR grade H<sub>2</sub>O, MgSO<sub>4</sub> (7 mM), Styo-9 green (0.5  $\mu$ M), deoxyribonucleotide triphosphates (dNTPs, 1.4 mM), Bst 2.0 DNA polymerase (0.4 U/ $\mu$ l), Warmstart reverse transcriptase (0.3 U/ $\mu$ l), primer sets (0.2 mM F3 and B3c, 1.6 mM FIP and BIP, 0.8 mM LF and LB (Table 3-2). Table 3-3 summarized the RT-LAMP recipe. The reaction was performed at a constant temperature of 65°C using either a benchtop PCR instrument (Bio-Rad

CFX96) or a customized heat block. All the reactions were added with an additional 25 µl mineral oil to prevent evaporation and cross-contamination.

**Table 3-2.** RT-LAMP primer sets targeting N and E regions of SARS-Cov-2

<b>Primer</b>		<b>Sequence (5'-3')</b>
<b>Gene N</b>	<b>F3</b>	AACACAAGCTTTCGGCAG
	<b>B3</b>	GAAATTTGGATCTTTGTCATCC
	<b>BIP</b>	TGCGGCCAATGTTTGTAAATCAGCCAAGGAAATTTGGGGAC
	<b>FIP</b>	CGCATTGGCATGGAAGTCACCTTTGATGGCACCTGTGTAG
	<b>LF</b>	TTCCTTGTCTGATTAGTTC
	<b>LB</b>	ACCTTCGGGAACGTGGTT
<b>Gene E</b>	<b>F3</b>	AACACAAGCTTTCGGCAG
	<b>B3</b>	GAAATTTGGATCTTTGTCATCC
	<b>BIP</b>	TGCGGCCAATGTTTGTAAATCAGCCAAGGAAATTTGGGGAC
	<b>FIP</b>	CGCATTGGCATGGAAGTCACCTTTGATGGCACCTGTGTAG
	<b>LF</b>	TTCCTTGTCTGATTAGTTC
	<b>LB</b>	ACCTTCGGGAACGTGGTT

**Table 3-3.** RT- LAMP Master mix

<b>Components</b>	<b>Working Concentration (25µl)</b>
FIP/BIP primers	1.6 µM
F3/B3 primers	0.2 µM
LF/LB primers	0.4 µM
Isothermal Amplification	1x
MgSO <sub>4</sub>	6 mM
Betaine	0.4 M
dNTP	1.4 mM
syto-9 green fluorescent	0.5 µM
Bst 2.0 DNA polymerase	10 U
WarmStart Reverse Transcriptase	7.5 U
UP Water	6 µl



### **3.2.6. Spiked saliva sample testing**

The saliva samples were collected from healthy volunteers. The saliva RNAs were extracted by the QIAamp Viral RNA Mini Kit according to the manufacturer protocol. The final concentration of extracted RNA was measured by Nanodrop 2000 (Thermo Fisher Scientific) as 87 ng/ $\mu$ l. The heat-inactivated SARS-CoV-2 RNAs and non-SARS-CoV-2 human coronavirus synthetic controls were spiked into the extracted saliva RNA solution at various concentrations ranging from 10 to  $10^5$  copies/ $\mu$ l. Typically 1  $\mu$ l of the mock RNA sample was used in the reaction unless otherwise stated.

### **3.2.7. Clinical nasopharyngeal sample testing and statistical analysis**

Nasopharyngeal swab samples were obtained from the Penn State Milton S. Hershey Medical Center in Hershey, PA at various times from October 2020 to February 2021. The use of these deidentified specimens was approved by the institutional review board (IRB) of the Pennsylvania State University Hershey Medical Center (study number STUDY00016633). All these nasopharyngeal swab samples were initially tested with the FDA EUA-Authorized Simplexa RT-PCR COVID-19 Direct assay (DiaSorin Molecular, Cypress, CA, USA). The collected nasopharyngeal samples were stored in the viral transport medium (VTM) and frozen at  $-80^{\circ}\text{C}$  before use. The viral RNAs were extracted by ThermoFisher MagMAX™ Viral/Pathogen Nucleic Acid Isolation Kit in the Animal Diagnostic Laboratory (BSL 3) at Penn State, University Park in accordance with a protocol approved by the Institutional Biosafety Committee. The diagnostic sensitivity is defined as  $\text{TP}/(\text{TP}+\text{FN})$ . The diagnostic specificity is defined as  $\text{TN}/(\text{TN}+\text{FP})$ . TP, TN, FP, FN represents true positive, true negative, false positive, and false negative, respectively.

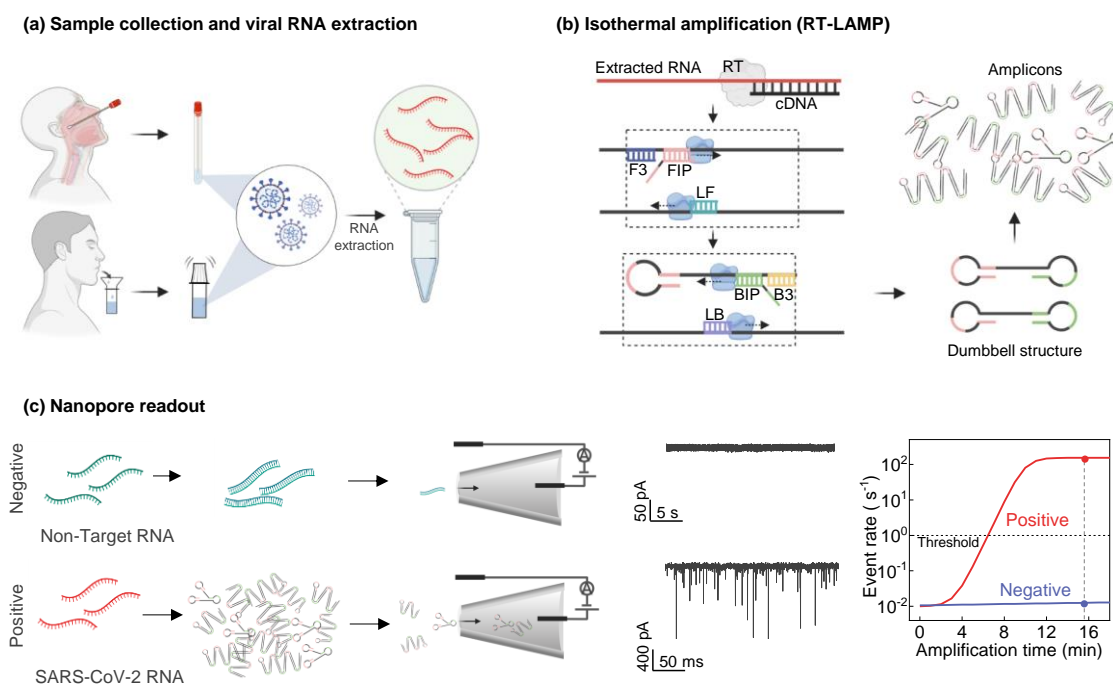
### 3.3. Result and discussion

#### 3.3.1. Overall workflow from sample to nanopore counting

**Figure 3-2** illustrates the overall workflow of the platform from sample collection to RT-LAMP coupled nanopore detection. The SARS-CoV-2 viral RNA was firstly extracted and purified from either the nasopharyngeal swab sample [77, 79, 83] or the saliva sample [78, 80, 83, 84] (**Figure 3-2a**). A subsequent isothermal RT-LAMP amplification was performed at 65 °C. In the presence of a few copies of SARS-CoV-2 viral RNA, a dumbbell-like DNA structure will be synthesized as a template for further amplification. The final product obtained from the RT-LAMP reaction is a mixture of stem-loop DNAs with various stem lengths and various cauliflower-like structures with multiple loops (**Figure 3-2b**), formed by annealing between alternately inverted repeats of the target sequence in the same strand [49]. Typically, amplicons can be amplified as much as  $10^9$  times within an hour [85].

Afterward, the nanopore counting analysis was performed to examine the concentration of the resulting amplicons. This is based on the fact that the nanopore event rate has a linear relation with the analyte concentration in the diffusion-limited region [27, 82]. **Figure 3-2c** shows two representative cases: a non-target negative control and a positive sample. For the negative control sample, no amplification would occur, resulting in an unchanged product concentration. We found the nanopore event rate for the negative control is negligible ( $<0.029 \text{ s}^{-1}$  at 99.7% confidence level, **Figure 3-1**) after 15 minutes of reaction. This ultra-low event rate suggests that the background molecules in the RT-LAMP master mix will not interfere with the nanopore analysis of amplicons. On the other hand, the event rate for the positive sample increased significantly to  $110 \text{ s}^{-1}$ . This result indicates that amplicons concentration indeed increased after 15 minutes of reaction, and the concentration change can be clearly captured by our nanopore event rate. The right panel of **Figure**

**3-2 c** shows the nanopore event rate as a function of RT-LAMP reaction time. We adopted an event rate threshold of  $1 \text{ s}^{-1}$  as the criteria for a positive call in our study unless otherwise stated. This threshold is much higher than the background event rate in the negative control ( $<0.029 \text{ s}^{-1}$ ) such that the false-positive rate can be minimized.



**Figure 3-2.** Workflow of RT-LAMP coupled nanopore method for SARS-CoV-2 detection. (a) Sample collection, preparation, and RNA extraction from either the nasopharyngeal swab sample or the saliva sample. (b) RT-LAMP amplification. One step RT-LAMP reaction is performed at  $65^{\circ}\text{C}$  for 15 min. (c) Nanopore readout. In a negative control sample, no amplification occurs, resulting in a negligible event rate. In a positive case, amplicons increased significantly, resulting in a sharp increase in event rate. The right panel shows the nanopore event rate as a function of RT-LAMP reaction time. The event rate threshold was set at  $1 \text{ s}^{-1}$  as the criteria for a positive call.

### 3.3.2. SARS-CoV-2 RT-LAMP assay validation

We first validated the RT-LAMP assay against the SARS-CoV-2 RNA. We adopted two LAMP primer sets targeting the N and E gene of SARS-CoV-2, respectively [86]. **Table 3-2** and **Table 3-3** summarized the primer information and the RT-LAMP reaction setup. background presented

the triplicated real-time RT-LAMP results on a 10× serial dilution of heat-inactivated SARS-CoV-2 RNA samples (stock concentration:  $2 \times 10^5$  copies/ $\mu$ l) using a benchtop PCR instrument. As shown in **Figure 3-3c**, the N primer set showed a better performance than the E primer set in terms of sensitivity and speed. The E primer set was not able to pick up 20 copies per reaction, while the N primer set can detect 2 out of 3 replicates at 20 copies. Moreover, the time to positive (TTP) value of N primer sets was less than 10 minutes for all input concentrations, whereas E primer sets took more than 13 minutes even for the most concentrated case ( $2 \times 10^5$  copies).

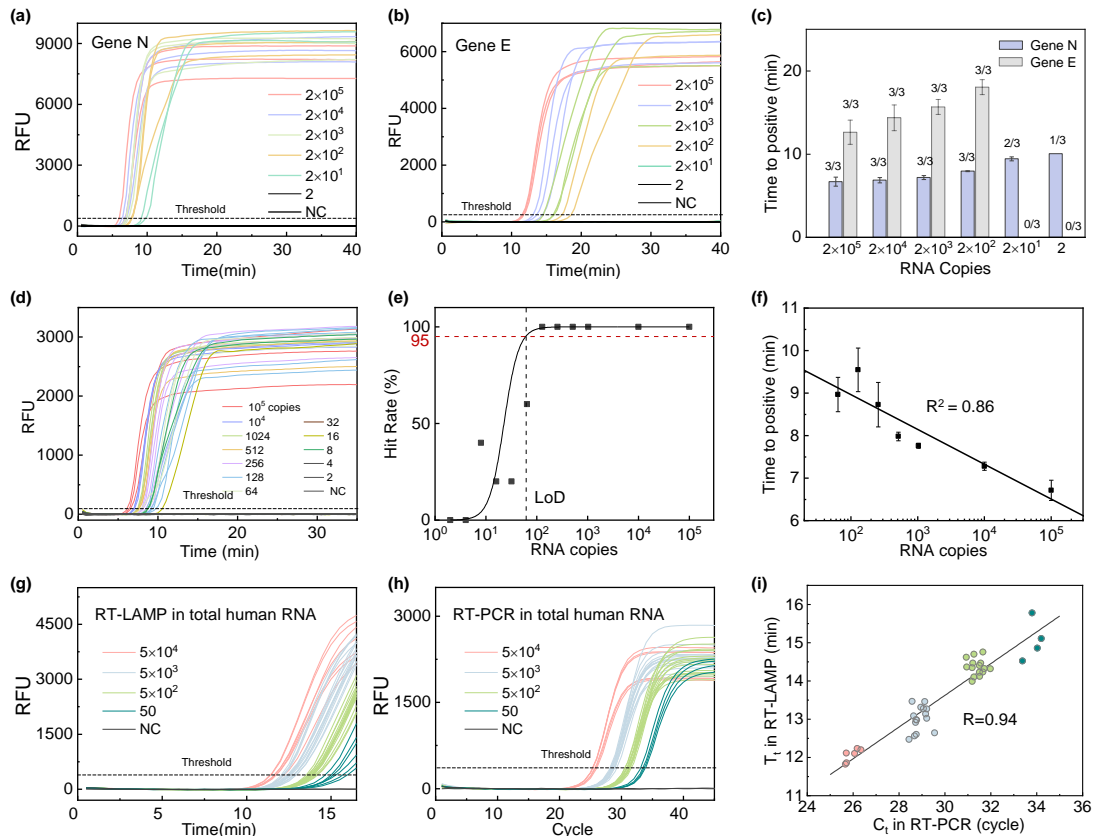
Based on this comparison, we chose the N primer set for our SARS-CoV-2 RT-LAMP assay in the following studies. To determine the limit of detection (LoD) of this assay, we performed the real-time RT-LAMP reaction with a 2× serially diluted RNA sample down to 2 copies. As shown in **Figure 3-3d**, concentrations above 128 copies/reaction were all amplified successfully, and concentrations below 4 copies/reaction were not able to be picked up. To estimate the assay LoD, we fitted a logistic curve for the hit rates at different RNA copies [87]. The hit rate is defined as the number of amplified samples over all samples. As shown in **Figure 3-3e**, the LoD of the N primer set RT-LAMP assay is determined to be 65 copies/reaction at the 95% confidence level. This LoD is on par with other reported RT-LAMP assays targeting N regions [20, 75, 88]. In addition, we also examined the threshold time as a function of the RNA concentrations. As shown in **Figure 3-3f**, the threshold time decreased from 10 min to 7 min when the RNA concentration increased from  $10^5$  to 2 copies. A linear fit produced the  $R^2$  with 0.86, indicating that a semi-quantitative RT-LAMP test is feasible.

To evaluate the effectiveness of RT-LAMP assay in human total RNA background and benchmark it with the gold standard RT-PCR assay from United States CDC (Table 3-1), we prepared 10-fold serial dilutions of SARS-CoV-2 RNAs in human total RNA background. The human total RNA was extracted from healthy saliva samples by a commercial kit. The final concentration of salivary

RNA measured by the Nanodrop was 87 ng/ $\mu$ l. A total of 42 samples at four different concentrations were tested. Figure 3-3g and Figure 3-3h showed the RT-LAMP and RT-PCR results, respectively. As shown in Figure 3-3i, the RT-LAMP threshold time and the RT-PCR threshold cycle showed a Pearson correlation coefficient of 0.94, indicating an excellent quantitative agreement between RT-LAMP and RT-PCR results, despite the human total RNAs background.

### 3.3.3. Nanopore counting of RT-LAMP amplicons

After validating the SARS-CoV-2 RT-LAMP assay, we set out to perform the nanopore counting analysis on the resulting amplicons. A testing sample with an RNA concentration of  $10^4$  copies was amplified for different reaction times ranging from 0 to 16 min. The reaction was stopped by heating the reaction to 95 °C for 5 minutes. The end products were examined by gel electrophoresis. As shown in **Figure 3-4a**, the gel started to show a typical ladder pattern with many bands of different sizes after 8 minutes of RT-LAMP reaction. These bands became darker as the reaction times increased, indicating a successful amplification occurred.



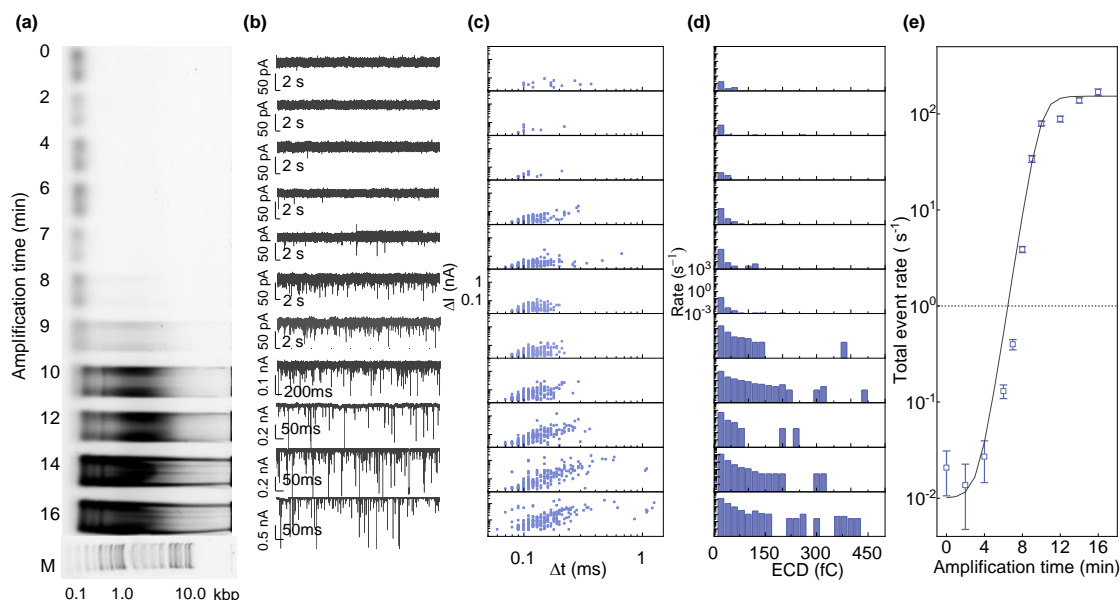
**Figure 3-3.** RT-LAMP assay validation. (a) N primer set results, and (b) E primer set results with viral RNA concentrations ranging from 2 and 105 copies per reaction. (c) Time to positive value comparison between the N primer set (blue bars) and the E primer set (grey bars) at different RNA concentrations. The N primer set showed better performances in terms of sensitivity and time to positive. (d) Real-time RT-LAMP result with a finer serial dilution ( $2\times$ ) using N primer set. (e) The extracted hit rate at various RNA concentrations to establish the assay LoD, which is determined to be 65 copies at 95% confidence level. (f) Time to positive value with N primer sets at concentrations ranging between 102 and 105 copies per reaction. A good linearity is obtained, indicating that a semi-quantitative test is feasible. (g) Real-time RT-LAMP result in saliva RNA background. (h) Real-time RT-PCR result in saliva RNA background. (i) The correlation between the RT-PCR and RT-LAMP measurement in total saliva RNA background.

These end products were then examined by the glass nanopore sensor. The amplicon solution was adjusted to 1M salt concentration to facilitate the nanopore measurement [82]. A typical nanopore readout was performed under 200 mV bias until at least 100 events were detected or 30 minutes of measurement was reached. A minimal event number of 100 ensures  $<10\%$  uncertainty of event rate determination [82]. **Figure 3-4b** presents the representative current traces of amplicons at different

reaction times (note scale differences). It is evident that more events showed up as we increased the reaction time. To perform the nanopore counting, we first characterized the events by their current drop ( $\Delta I$ ) and dwell time ( $\Delta t$ ). As shown in **Figure 3-4c**, there is a clear population shift in the  $\Delta I$  vs.  $\Delta t$  scattering plot, indicating the distribution change of the amplicon size. This shift is expected since the LAMP product is a mixture of stem-loop DNA with various stem lengths and various cauliflower-like structures with multiple loops [49, 85].

To quantify the amplicon size distributions and their relative abundance, we used the event charge deficit (ECD, defined as  $\int_{\Delta t} \Delta I(t) dt$ ) to represent the approximate amplicon size [89]. An ECD bin size of 20 fC was used to characterize each subpopulation. The event rate of the ECD subpopulation was obtained by normalizing the corresponding event numbers by the nanopore measurement time. This normalization process gives us the capability to benchmark nanopore measurements performed with different readout times. **Figure 3-4d** shows the distribution of event rate vs. ECD at different reaction times. Two interesting features can be observed. First, the event rate of all sub-populations increases as the amplification time increases. For instance, the event rate for ECDs below 20 fC was  $0.016 \text{ s}^{-1}$  at 0 minutes and increased to  $129.50 \text{ s}^{-1}$  at 16 minutes. The event rate for ECDs between 400 and 420 fC was  $0 \text{ s}^{-1}$  at 0 minutes and increased to  $0.25 \text{ s}^{-1}$  at 16 minutes. This change indicates the amplicon concentration of each size increased, and the RT-LAMP product was dominated by smaller amplicons (note the *log* scale in rate in **Figure 3-4d**). Second, the sub-populations with  $\text{ECD} > 60 \text{ fC}$  started to be captured by the nanopore measurement after 6 minutes of reaction. The event rate of the sub-populations increased about 10 times compared to 0 minutes. However, gel electrophoresis analysis (**Figure 3-4a**) was not able to distinguish the population increase at the same conditions, only weak bands starting to be visible after 8 minutes of reaction. This suggested that the nanopore readout is more sensitive than the gel analysis, and nanopore measurement can capture the amplification dynamic faster.

We further analyzed the total event rate by the summation of all sub-populations event rates ( $R_{tot} = \sum_i R_i$ ). As shown in **Figure 3-4e**, the total event rate increased more than three orders of magnitude from  $0.021 \text{ s}^{-1}$  to  $168.23 \text{ s}^{-1}$  as the reaction time went from 0 minutes to 16 minutes. We fitted the total event rate as a function of RT-LAMP reaction time by the logistic growth model [27, 68] with  $R(t) = R_L + (R_H - R_L)/(1 + e^{-\beta(t-t_0)})$ , where  $R_L$  ( $0.01 \text{ s}^{-1}$ ) and  $R_H$  ( $152.8 \text{ s}^{-1}$ ) are the low and high bound of the event rate,  $t_0$  (9.94 min) is the time when the growth rate is at maximum, and  $\beta$  ( $1.45 \text{ min}^{-1}$ ) is the maximum steepness of amplification rate. The fitted  $R_L$  value of  $0.01 \text{ s}^{-1}$  was close to the event rate of 9 negative controls ( $\mu+3\sigma = 0.029 \text{ s}^{-1}$ , **Figure 3-1**), where mean ( $\mu$ ) and standard deviation ( $\sigma$ ) of the event rate is  $0.009 \text{ s}^{-1}$  and  $0.007 \text{ s}^{-1}$  respectively. It is worth mention that choosing a proper threshold for making a positive/negative call is a trade-off between turnaround time and specificity. For example, if we set the threshold based on the negative controls ( $0.029 \text{ s}^{-1}$ ), a positive decision can be made in 5 minutes, but it may lead to a high false-positive rate. In this study, we set a threshold of  $1 \text{ s}^{-1}$  (100 times higher than the  $R_L$ ) to minimize the false positive rate.

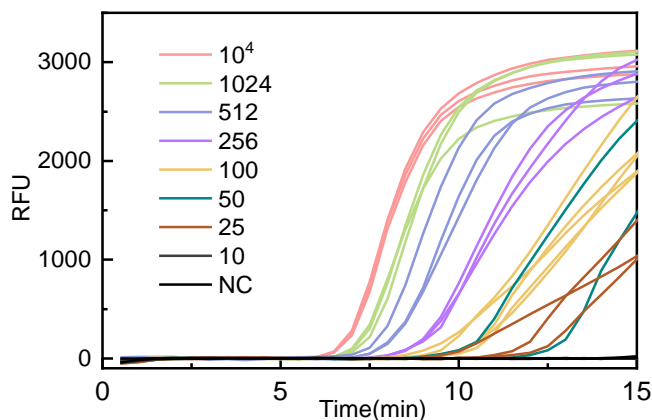




**Figure 3-4.** Nanopore counting of RT-LAMP amplicons. (a) Gel electrophoresis (2% agarose gel) result of the RT-LAMP products, at various reaction times from 0 mins to 16 mins. (b) Corresponding current time traces measured in nanopores with 200 mV bias (Note the scale differences). (c) Corresponding current drop vs. dwell times distribution at different reaction times. (d) Corresponding event rate distribution as a function of ECD values. (e) The total event rate as a function of the reaction time. The solid line is fitting to the logistic growth model  $R^2=0.95$ .

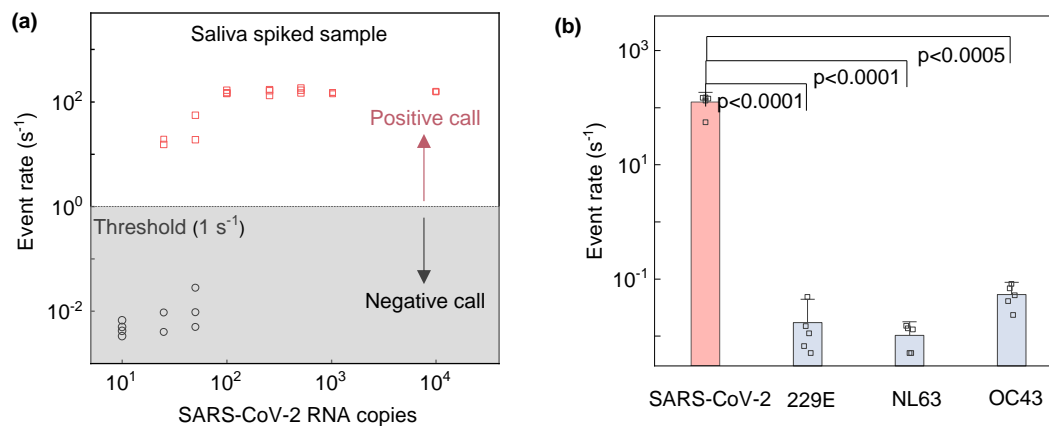
### 3.3.4. Evaluation with spiked saliva samples

We evaluated the nanopore sensor analytical sensitivity using the SARS-CoV-2 spiked saliva sample. These spiked saliva samples were prepared by adding 2-fold serially diluted heat-inactivated SARS-CoV-2 RNA into the total RNA background extracted from the healthy saliva samples. The final viral RNA concentrations range from  $10^5$  copies/ $\mu\text{l}$  to 10 copies/ $\mu\text{l}$ . The RT-LAMP reactions were performed with 1  $\mu\text{l}$  of the viral RNA sample at  $65^\circ\text{C}$  for 15 mins (**Figure 3-5**) followed by the nanopore counting for event rate determination. Each concentration was tested at least three times. The limit of detection was established as the lowest number of concentrations that >95% percent sample was tested positive. **Figure 3-6a** shows the measured event rate as a function of different SARS-CoV-2 RNA concentrations. As shown, at the concentration of 100 copies/ $\mu\text{l}$ , 5 out of 5 samples were determined to be positive since all have event rates larger than  $1 \text{ s}^{-1}$ , whereas 2 out of 5 samples at the concentration of 50 copies/ $\mu\text{l}$  were detected as positives. The LoD was thus determined to be 100 copies/ $\mu\text{l}$  with the SARS-CoV-2 spiked saliva sample. This LoD with saliva RNA in the background is similar to the LoD obtained by testing the purified viral RNA sample (65 copies/ $\mu\text{l}$ , **Figure 3-3e**). These results confirmed that (1) the RT-LAMP assay is specific to the SARS-CoV-2 RNA, and (2) the saliva RNA background has negligible impact on event rate determination since SARS-CoV-2 RNA specific amplicons dominated the RT-LAMP product.



**Figure 3-5.** Real-time result of the RT-LAMP reaction using the SARS-CoV-2 spiked saliva sample at different concentrations.

For the analytical specificity test, we used three different human coronaviruses (229E, NL63, and OC43) RNAs spiked in the saliva RNA background. We tested five replicates, each at the concentration of  $10^5$  copies/ $\mu\text{l}$ . As shown in **Figure 3-6b**, a sharp contrast between the event rates of SARS-CoV-2 and other human coronavirus samples can be observed. The average event rate of SARS-CoV-2 cases was  $110 \text{ s}^{-1}$ , and the average event rate of the 229E, NL63, and OC43 was  $0.03 \text{ s}^{-1}$ ,  $0.01 \text{ s}^{-1}$ , and  $0.05 \text{ s}^{-1}$ , respectively. The t-test showed that the event rate of the SARS-CoV-2 samples is statistically significant compared to the other three human coronaviruses samples. This result confirmed an excellent analytical specificity of the RT-LAMP coupled nanopore sensor against the SARS-CoV-2.



**Figure 3-6.** Analytical sensitivity and specificity test with saliva spiked sample. (a) Event rate of the RT-LAMP amplicons at various concentrations of SARS-CoV-2 in total saliva RNA background. An event threshold of 1 s<sup>-1</sup> is used for positive/negative call. (b) The event rate for SARS-CoV-2 and three other non-SARS-CoV-2 targets with a concentration of 10<sup>5</sup> copies in total saliva RNA background. All non-SARS-CoV-2 targets showed event rates much less than 1 s<sup>-1</sup> and were correctly classified as negatives.

### 3.3.5. Clinical validation with nasopharyngeal swab samples

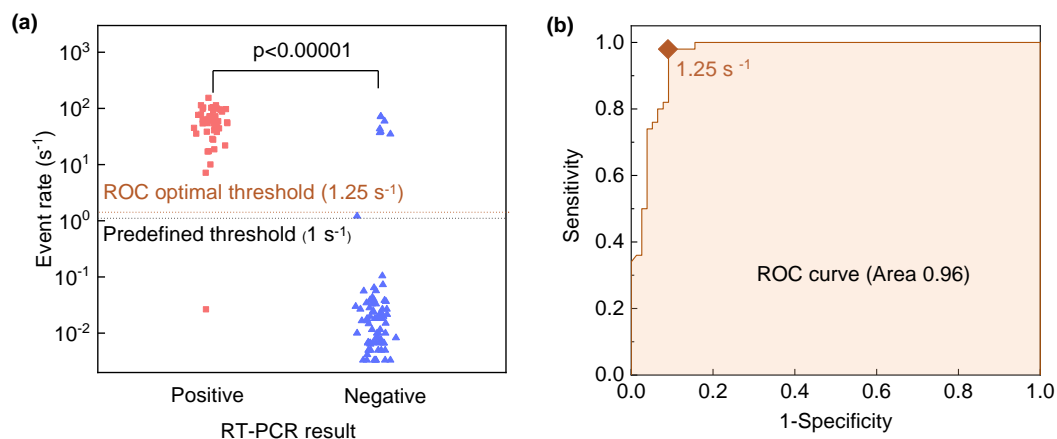
To evaluate the utility of the nanopore sensor against real clinical samples, we tested a total of 127 nasopharyngeal swab clinical samples obtained from Penn State Hershey Medical Center. These clinical samples were coded to remove information associated with patient identifiers. The FDA EUA-Authorized RT-PCR with Simplexa COVID-19 Direct assay (DiaSorin Molecular, Cypress, CA, USA) performed at initial diagnosis is considered the reference method to benchmark our nanopore sensors. A total of 50 positive and 77 negative samples were tested. The viral RNAs from these clinical samples were firstly extracted by ThermoFisher MagMAX™ Viral/Pathogen Nucleic Acid Isolation Kit. We then performed the RT-LAMP reactions at 65°C for 15 mins and measured event rates of the products by nanopore counting (**Figure 3-7a**). As shown, it is clear that the event rate of positives was significantly higher than that of the negatives ( $p < 0.00001$ ). With a predefined event rate threshold of 1 s<sup>-1</sup>, 49 out of 50 positives were detected as true positives, and 70 out of 77

negatives were detected as true negatives(). The diagnostic sensitivity, and specificity of the nanopore sensor compared to the reference method was 98% (95% CI=94.1%-100%) and 90.9% (95% CI= 84.5%-97.3%).

We further evaluated the receiver operating characteristic (ROC) curve [90, 91] to find the optimal event rate threshold for positive/negative cutoff by varying the threshold from 0.001 to 500 s<sup>-1</sup> (**Figure 3-7b**). As shown, increasing the event rate threshold will improve the diagnostic specificity but deteriorates the diagnostic sensitivity. The optimal event rate threshold corresponds to the case where both the specific and sensitivity is closest to 1 [90, 91]. Based on this approach, we obtained the ROC optimal event rate threshold as 1.25 s<sup>-1</sup>. Note that the optimal threshold is highly relevant to the sample set. With this optimized threshold, the testing statistics were re-assessed and summarized in **Table 3-4**. As shown, the statistics using the ROC threshold are very similar to those with a predetermined threshold of 1 s<sup>-1</sup>. The area under curve (AUC) was measured to be 0.96, indicating the RT-LAMP coupled nanopore sensor is highly sensitive and specific against SARS-CoV-2.

**Table 3-4.** Statistics of analyzing 127 clinical nasopharyngeal swab samples

Nanopore result	Pos/Pos	Neg/Pos	Pos/Neg	Neg/Neg	Sensitivity (95%CI)	Specificity (95%CI)
<b>Predefined threshold</b>	49/50	1/50	7/77	70/77	98.0% (94.1-100)	90.9% (84.5-97.3)
<b>ROC threshold</b>	49/50	1/50	6/77	71/77	98.0% (94.1-100)	92.2% (86.2-98.2)



**Figure 3-7.** Diagnostic sensitivity and specificity test with clinical nasopharyngeal swab samples. (a) Event rate of the RT-LAMP amplicons for a total of 127 samples. These samples were initially tested with RT-PCR (50 positives and 77 negatives). A predefined event rate threshold of 1 s<sup>-1</sup> and a ROC optimized event rate threshold of 1.25 s<sup>-1</sup> were used in nanopore sensors to classify the samples. (b) ROC curve analysis of the test result. The area under the ROC curve (AUC) is 0.96.

**Table 3-5.** Summary of clinical sample testing with RT-PCR and nanopore method

Sample#	RT-PCR	Nanopore (s <sup>-1</sup> )	Sample#	RT-PCR	Nanopore (s <sup>-1</sup> )	Sample#	RT-PCR	Nanopore (s <sup>-1</sup> )
1	P	27.81	44	P	97.20	87	N	0.007
2	P	18.65	45	P	114.00	88	N	0.008
3	P	17.05	46	P	103.20	89	N	0.003
4	P	17.20	47	P	91.80	90	N	0.022
5	P	7.13	48	P	113.25	91	N	0.003
6	P	10.00	49	P	96.40	92	N	0.018
7	P	63.00	50	P	103.40	93	N	0.010
8	P	154.50	51	N	0.012	94	N	0.007
9	P	98.00	52	N	0.005	95	N	0.003
10	P	87.67	53	N	0.023	96	N	0.005
11	P	62.75	54	N	0.007	97	N	0.010

12	P	106.50
13	P	105.25
14	P	93.33
15	P	0.06
16	P	76.67
17	P	54.88
18	P	71.11
19	P	77.20
20	P	72.29
21	P	72.00
22	P	72.50
23	P	65.20
24	P	28.80
25	P	40.56
26	P	44.50
27	P	45.00
28	P	54.17
29	P	21.80
30	P	35.60
31	P	38.25
32	P	38.00
33	P	44.20
34	P	54.20
35	P	60.80
36	P	54.83

55	N	59.667
56	N	0.007
57	N	0.037
58	N	72.000
59	N	0.020
60	N	0.015
61	N	0.017
62	N	0.033
63	N	38.833
64	N	0.020
65	N	0.030
66	N	0.057
67	N	0.024
68	N	0.007
69	N	0.043
70	N	0.039
71	N	0.003
72	N	0.033
73	N	0.019
74	N	37.000
75	N	0.018
76	N	0.007
77	N	0.025
78	N	0.008
79	N	0.007

98	N	0.005
99	N	0.007
100	N	0.027
101	N	0.010
102	N	0.074
103	N	0.106
104	N	0.057
105	N	0.035
106	N	0.065
107	N	0.038
108	N	0.038
109	N	1.210
110	N	0.018
111	N	0.017
112	N	0.018
113	N	0.012
114	N	0.040
115	N	0.027
116	N	0.027
117	N	0.015
118	N	0.008
119	N	0.008
120	N	0.006
121	N	71.800
122	N	0.005

37	P	56.50
38	P	60.50
39	P	59.25
40	P	49.71
41	P	55.25
42	P	53.83
43	P	63.25

80	N	0.003
81	N	0.005
82	N	35.000
83	N	43.556
84	N	0.003
85	N	0.005
86	N	0.004

123	N	0.003
124	N	0.022
125	N	0.010
126	N	0.028
127	N	0.007

### 3.4. Summary

In summary, we have demonstrated a highly sensitive, specific, and rapid SARS-CoV-2 detection platform by coupling the RT-LAMP with glass nanopore sensors. The optimized RT-LAMP assay targeting the nucleocapsid gene showed an LoD of 65 copies at the 95% confidence level. It also possessed an excellent specificity against other human coronavirus RNA targets. The nanopore digital counting method was able to pick up the amplification process much quicker than the bulk optical method due to its intrinsic single molecule level of sensitivity. Validation of the nanopore platform with 127 clinical nasopharyngeal swab samples demonstrated its excellent diagnostic performances using RT-PCR as the gold standard. With further integration of the electronics and miniaturization of the device, RT-LAMP coupled nanopore digital counting method has great potential for developing next-generation point of care molecular diagnostics for diseases such as COVID-19.

## **Chapter 4 On Stochastic Reduction in Laser-Assisted Dielectric Breakdown for Programmable Nanopore Fabrication**

While the glass nanopipette demonstrated foundational premise of the concept in Chapter 1&2, SiNx is a more suitable nanopore material since it is easier to be integrated and interfaced with electronics and fluidics. In this chapter, I investigated the laser-assisted controlled breakdown (LACBD) fabrication for single nanopore localization. I also developed a physical model to estimate the probability of forming a single nanopore under different combinations of the laser power and the electric field. Both the model and our experimental data suggest that a combination of a high laser power and a low electric field is statistically favorable for forming a single nanopore at a programmed location. Addressing the reliability and fidelity issue in the controlled dielectric breakdown (CBD) method is critical towards the scalable SiNx nanopore fabrication, which is essential towards developing integrated point of care devices.



## 4.1. Introduction

Solid-state nanopores offer promising label-free detection of single molecules such as DNAs [27, 92-96], RNAs [97, 98], proteins [99, 100], and DNA-protein complexes [101, 102]. Conventional solid-state nanopore fabrication methods involve focused electron beams [103] or ion beams [37, 104] for physical bombardment. However, due to limited throughput and high complexity, nanopore-based sensing has limited accessibility for ordinary labs. An alternative controlled breakdown (CBD) method for nanopore fabrication was demonstrated to tackle these challenges [105-109], relying on the electric field-induced physical breakdown of the dielectric material. Nevertheless, the stochastic nature of the breakdown makes it challenging to predetermine the number and location of the nanoscale pinhole [105, 110-114]. A single nanopore is desirable for most single-molecule experiments. Besides, many nanopore-based applications such as tunneling current sensing [115, 116] and plasmonic nanopores [117-122] would require the nanopore to be localized specifically around an existing structure. So far, CBD-based nanopore localization efforts were predominately made by focusing the electric field through using tip-based technology [123, 124], selectively thinning the membrane [125], or fabricating pyramid structures on the membrane [126]. These methods often require additional apparatus or lithography patterning processes, thus limiting their flexibility and tunability.

Several recent studies have demonstrated that a focused laser beam can be used for nanopore fabrication in  $\text{SiN}_x$  membranes. This can be simply performed in the air without an additional electric field or in the electrolyte solutions with an external electric field for the dielectric breakdown. For example, Yuan *et al.* showed that directly drilling the  $\text{SiN}_x$  membrane in the air can fabricate sub 100 nm nanopore by applying Watt-level nanosecond laser pulses [127]. Ying *et al.* demonstrated that infrared laser-assisted controlled breakdown could significantly reduce the probability of forming multiple nanopores [128]. Gilboa *et al.* showed that a focused laser beam

with mW-intensity could irreversibly etch SiN<sub>x</sub> membranes in 1 M KCl, resulting in nanopores formation. They also found that the etching process was susceptible to the relative content of Si over N atoms in the SiN<sub>x</sub> membrane [129]. Yamazaki *et al.* showed that the SiN<sub>x</sub> etching rate was influenced by the supporting electrolyte and suggested the photothermal effect was responsible for the SiN<sub>x</sub> dissolution process [31]. These prior studies, while different in their laser specifications, electric field strength, unambiguously suggested laser-assisted CBD could help control the nanopore position and reduce the possibility of forming multiple pores.

In this work, we investigated the impact of the surrounding environment, the electric field, and the laser power on the probability of forming a single nanopore at the focused laser spot, with the aim to optimize the laser-assisted dielectric breakdown. We developed a physical model to project the confidence level of creating a single nanopore at different combinations of laser power and electric field. The model relies on material-specific properties (Weibull statistical parameters) and experimental-specific parameters (laser-induced photothermal etching rate). With the guidance of this model, we experimentally probed the nanopore number and location using the ionic current enhancement method [130, 131]. Both the model and experimental results suggested that a high laser power and a low electric field is a favorable combination for creating a single nanopore at the focused laser spot. Our findings would provide insights into optimizing the laser-assisted dielectric breakdown towards solid-state nanopore fabrication and localization.

## 4.2. Materials and methods

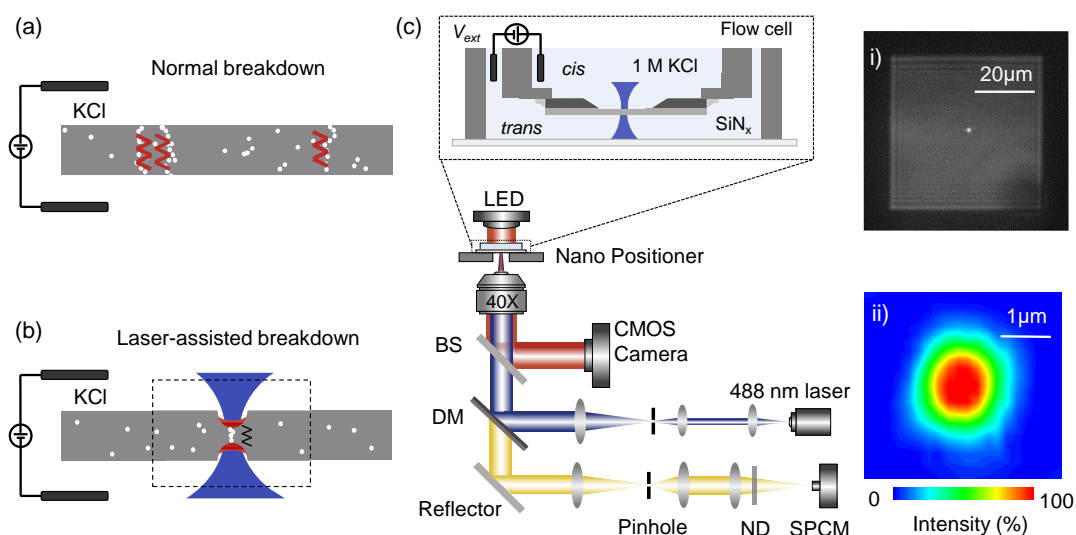
### 4.2.1. Materials and Chemicals

Low-stress SiN<sub>x</sub> membranes on 200 μm thick lightly doped silicon substrates were used in our experiments (Norcada, Canada). The SiN<sub>x</sub> membranes are 15 nm and 30 nm in thickness with a 50×50 μm<sup>2</sup> window. Before mounting into our custom-built PMMA based flow cell, the SiN<sub>x</sub> membranes were cleaned in oxygen plasma for 120 s at 50 W to facilitate the wetting of the membrane surface. Ag/AgCl electrodes were house-made with 0.2-0.375 mm Ag wires (Warner Instruments, Hamden, USA). λ-DNA (48.5 kbp, 0.3 μg/μl) was purchased from ThermoFisher. PBS, KCl, and Tris-EDTA solution (pH 8.0) were purchased from Sigma-Aldrich. Ecoflex-5 used as an insulating sealant of the SiN<sub>x</sub> chip was obtained from Smooth-On, Inc. Prior to use, all solutions were filtered with a 0.2 μm Anotop filter (Whatman plc).

### 4.2.2. Instrumentation

The SiN<sub>x</sub> membrane chip was sealed onto a custom-built flow cell with a transparent quartz coverslip bottom, forming the *cis* and *trans* chambers. Both sides of the chambers were filled with KCl solution. Two Ag/AgCl electrodes were inserted into the KCl solution and electrically connected to a source meter unit (Keithley 2636) through a BNC cable. The chamber opposing the Si etch pit was grounded in our work unless otherwise stated. 488 nm (Coherent OBIS 488 LS) laser beams were focused onto a spatial pinhole (1-25+B-1+M-0.5, National Aperture) by an objective lens (M-5X, Newport) to reject out-of-focus light. The laser beams were re-collimated by an achromatic doublet (AC254-075-A, Thorlabs) and focused by an objective lens (RMS40X-PF, Thorlabs). The radius of the laser beam spot was 1 μm (FWHM, inset (ii) of **Figure 4-1c**). The

flow cell was mounted onto a 3D manual positioner above the microscope objective. The emitted light was collected by the same objective and directed at a CMOS camera (DCC1545M, Thorlabs) by a dichroic mirror (BB2-E02, Thorlabs). The entire assembly was shielded inside a Faraday cage to minimize electromagnetic interferences.



**Figure 4-1.** Schematic drawing of the nanopore fabrication by (a) normal breakdown and (b) laser-assisted breakdown. The drawings are for illustrative purposes and not to scale. (c) Schematic of the custom-built nanopore fabrication and characterization system. (BS: beam splitter, DM: dichroic mirror, ND: neutral-density filter). The focused laser spot at an arbitrary location on the membrane (inset i) and the Gaussian intensity profile of the laser (inset ii).

#### 4.2.3. Photoluminescence Characterization

The PL characterization was obtained by a customized LabVIEW program (National Instruments) that controls the motion of the nano positioner as well as collects the photon counting signals. The typical parameters for obtaining the scanned PL results in our experiments are 100 nm step size, 1 mW laser power, and 2 ms integration time. The counted emission photons were normalized to the integration time and the incident laser power (cpms/mW: counter per millisecond/ milliwatt).

#### 4.2.4. Atomic Force Microscopy Characterization

AFM measurements were performed on a Dimension Icon (Bruker) AFM microscope using Peak Force tapping mode. A triangular-shaped ScanAsyst-Air tip was used in this study. During the measurement, the peak force set point was set to 2 nN. The scan was performed at a scan rate of 0.226 Hz and 512 lines per sample.

#### 4.2.5. Nanopore Fabrication and Validation.

The buffer used in the etching rate experiment was performed in 2M KCl with 10 mM Tris and 1 mM EDTA (pH 7.4). All the nanopores (both with and without laser-assisted) were fabricated by the moving Z-Score method with 1 M KCl with 10 mM Tris and 1mM EDTA. The flowchart of the automated procedure for moving Z-score can be found in our previous work[110]. The feedback time of the customized LabView program is 20 ms. The number and the location of nanopores were validated by ionic current mapping. The typical parameters used for ionic current mapping were 2-4 mW laser power, 100 mV voltage, and 10-20  $\mu\text{m/s}$  scanning speed.

#### 4.2.6. DNA Sensing

$\lambda$ -DNA was added to the *cis* chamber to a final concentration of 100 pM. The Ag/AgCl electrodes were then connected to the Axopatch 200B amplifier (Molecular Devices, CA) with a 300 mV bias voltage. The amplified signal was filtered with a 4-pole Bessel set at 10 kHz and digitalized by a 16-bit/100 MHz DAQ card (NI 6363, Texas Instruments). Data analysis was carried out by using customized MATLAB code to extract the duration and depth of each current blockade events.

## 4.3. Result and discussion

### 4.3.1. Principle of Laser-Assisted Dielectric Breakdown

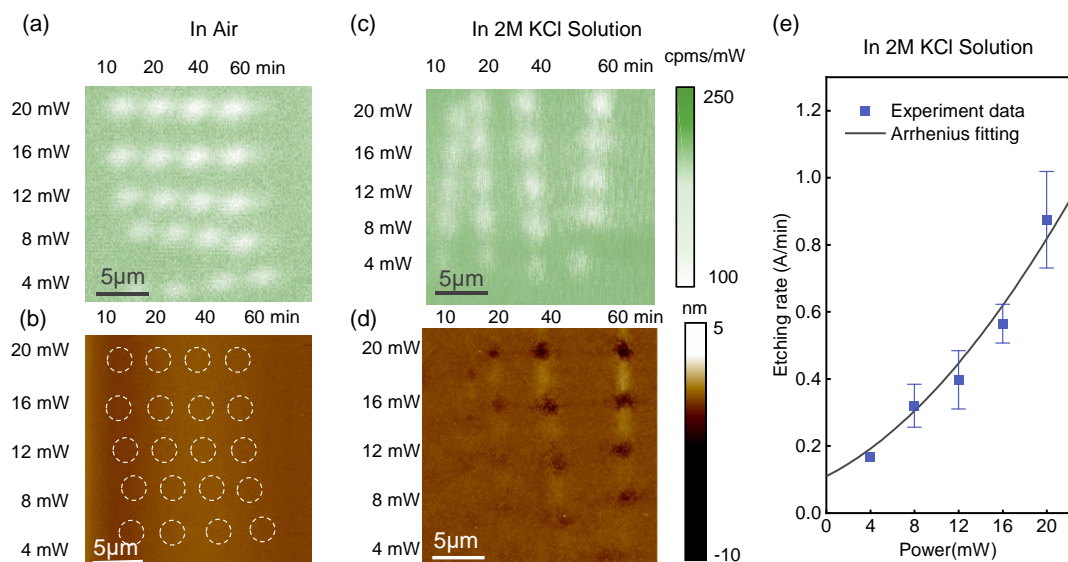
The dielectric breakdown under the influence of a biasing electric field is a well-studied phenomenon. A nanoscale pinhole could be created in the membrane when the density of accumulated defects reaches a critical value [105]. However, defect generation is a random process [111-113], which leads to poor control over the location of nanopore formation (**Figure 4-2a**). Multiple pores can be formed due to the stochastic subsequent nanopore creation between the occurrence of the first breakdown and the time when the applied voltage is terminated. Several works have demonstrated the laser-assisted dielectric breakdown for solid-state nanopore localization [31, 128, 129, 132]. The laser-localized thinning down facilitates the electric field enhancement at the laser spot. Since the defect generation efficiency increases exponentially with the electric field, the laser spot would have a much higher probability of first reaching the breakdown critical trap density (**Figure 4-1b**).

**Figure 4-1c** shows the schematic of our custom-built nanopore fabrication and characterization setup. A 488 nm Gaussian-profile laser beam was focused onto the SiN<sub>x</sub> membrane assembled in an optically accessible flow cell. A CMOS camera was used to provide a bright-field view. A single photon counting module (SPCM) was used for photoluminescence (PL) characterization of the material. A pair of Ag/AgCl electrodes across the membrane was used to apply a voltage for the dielectric breakdown. This setup enabled us to perform the laser-assisted dielectric breakdown, scanning PL for material characterization, and laser-enhanced ionic current mapping [130, 131] for nanopore location in a single platform (see **Methods** for details of the setup).

### 4.3.2. Kinetics of Laser-Induced Photothermal Etching of SiN<sub>x</sub> in Electrolyte

While the laser-induced thinning of SiN<sub>x</sub> in the electrolyte solution was universally observed, the underlying mechanism is controversial [31, 129]. To better understand the thinning kinetics in our experiments, we performed the laser radiation experiments on 30 nm-thick SiN<sub>x</sub> membranes with a focused 488 nm laser both in the air and in the electrolyte solution.

In the air, we sequentially radiated a 5×4 array at five different laser powers (4-20 mW) and varying exposure time (10-60 min). We then characterized this sample with scanning PL [133] and atomic force microscopy (AFM). Figure 4-2a shows the PL result. Evident PL reductions were observable at the laser exposed locations. However, the AFM characterization (Figure 4-2b) showed no visible thickness change at the laser spots. This existence of the PL change and the absence of thickness change suggests that the focused laser with power up to 20 mW only altered the microscopic electronic structures of the SiN<sub>x</sub> (photochemical effect) in the air<sup>45</sup>, rather than physical etching.



**Figure 4-2.** (a) Photoluminescence (PL) probed after exposing the SiN<sub>x</sub> to the laser in the air. (b) AFM characterization of the sample exposed in the air (dash circles are the laser exposed regions). The counted emission photons were normalized to the integration time and the incident laser power

(cpms/mW: counter per millisecond/milliwatt). No significant morphology change was observed. (c) PL probed after exposing the SiN<sub>x</sub> to the laser in 2 M KCl solution. (d) AFM characterization of the sample exposed in 2 M KCl solution. The material etching was visible in the laser spots. (e) Extracted SiN<sub>x</sub> etching rate as a function of the laser power. Note that the measured etching rate is the maximum etching rate in the membrane thickness direction. The solid line is the Arrhenius fitting. The PL map was obtained by scanning at 1 mW laser power with 200 nm step and 2 ms integration time.

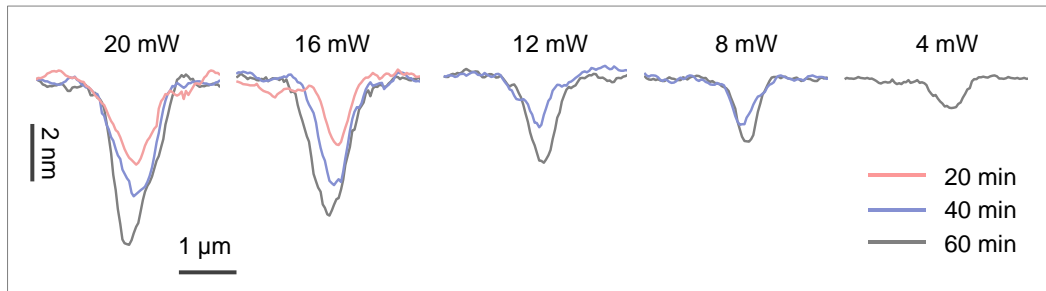
For the solution experiment, a 5×4 array was exposed in 2 M KCl with 10 mM Tris and 1 mM EDTA with the same laser dose as in the air. As shown in **Figure 4-2c** and **Figure 4-2d**, both the PL intensity and the AFM-obtained membrane thickness showed significant reductions in the laser-exposed area. This result suggested that the 20 mW laser not only altered the microscopic electronic structures [133] but also ‘etched’ the SiN<sub>x</sub> membrane in the 2 M KCl solution. To examine if the laser ‘etching’ of the SiN<sub>x</sub> in the electrolyte stems from the photothermal decomposition of the material, we performed a finite-element simulation to estimate the photothermal heating of the solution (**Figure 4-4**). We found the temperature (175°C) caused by the 20 mW laser is far below the SiN<sub>x</sub> decomposition temperature (1500 °C) [31]. As a result, the laser ‘etching’ of the SiN<sub>x</sub> in 2 M KCl in our experiment could not be ascribed to the photothermal decomposition of the material. In fact, the contrast of the experiments performed in the air and in the solution suggested that the laser-SiN<sub>x</sub> reactivity is a convoluted photochemical and photothermal process. The focused laser not only alters the microscopic electronic structures of the SiN<sub>x</sub> (photochemical effect), but also provides the heat for promoting the photothermal etching. It is no surprise that the surrounding environment would play a significant role due to their different heat dissipation coefficient and chemical composition [31].

To establish the relationship between the laser power and the etching rate in our experiment, we examined the AFM-obtained etching profile (**Figure 4-3**). The etching rate, defined by the maximal depth in the center of the etching profile, can be well fitted with the laser power to the Arrhenius equation [134],

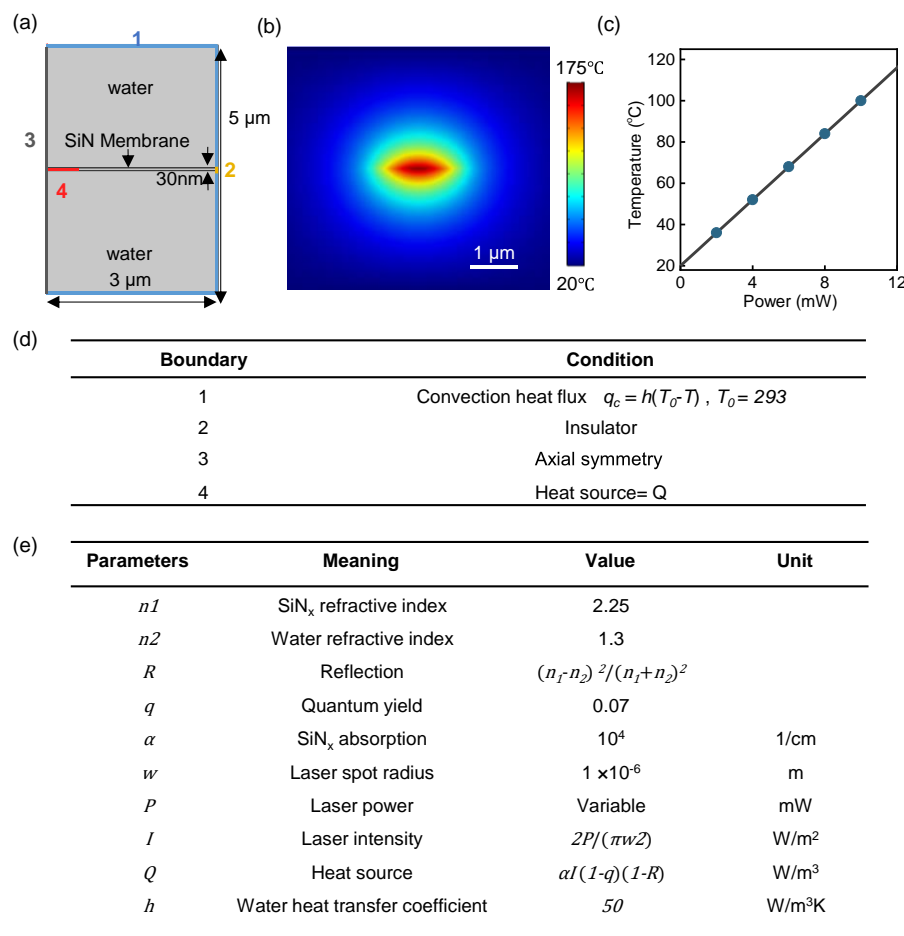


$$k = Ae^{-\frac{E_a}{R(bP+T_0)}} \quad (4-1)$$

where  $k$  is the etching rate ( $\text{\AA}/\text{min}$ ),  $A$  is the Arrhenius constant for the reaction ( $\text{\AA}/\text{min}$ ),  $E_a$  is the activation energy (kJ/mol),  $R$  is the gas constant,  $b$  is the photothermal coefficient (K/mW),  $P$  is the laser power (mW),  $T_0$  is the room temperature. Note that  $bP+T_0$  is the laser-induced temperature. The activation energy  $E_a$  fitted from **Figure 4-2e** was estimated to be 13.7 kJ/mol (see Table 4-1 for Arrhenius fitting parameters). Note that these parameters are  $\text{SiN}_x$  material-specific and experimental setup-specific and could vary from one lab to the other [31, 128, 129]. This excellent fitting to the Arrhenius equation suggests that the laser ‘etching’ of the  $\text{SiN}_x$  membrane in the solution results from the chemical reaction between the aqueous electrolyte and  $\text{SiN}_x$  membrane, promoted by the photothermal effect.



**Figure 4-3.** AFM-obtained etching profiles in Figure 4-2.



**Figure 4-4.** Finite-element simulation to study the photothermal heating of the solution. Heat transfer model was implemented by applying the first law of thermodynamics. (a) The physical domain used for simulation. A 30-nm-thick SiN<sub>x</sub> membrane was placed in the middle of the simulation domain and surrounded by water. At the bottom of the SiN<sub>x</sub> membrane, a heat source (Q) with Gaussian distribution of intensity was applied on an area with a radius of 1 μm to simulate the focused laser radiation. (b) Steady-state temperature profile under a 20 mW laser. The peak temperature is located in the center of the spot and quickly decreases to room temperature. The maximum temperature caused by the 20 mW laser was 175 °C, which is far below the SiN<sub>x</sub> decomposition temperature. (c) Peak temperature as a function of laser power. The temperature increases linearly with laser power. The slope of the line is the photothermal coefficient (8.06 K/mW). (d) Boundary conditions used in simulation. (e) Parameters used in simulation.

**Table 4-1.** Parameters used for Arrhenius fitting in Figure 4-2e

Parameters	Meaning	Value	Unit
$A$	Arrhenius constant	31.6	Å/min
$R$	Gas constant	$8.314 \times 10^{-3}$	kJ/mol/K
$E_a$	Activation energy	13.7	kJ/mol
$b$	Photothermal coefficient	8.06	K/mW
$T_0$	Room Temperature	293	K
$P$	Laser power	1-25	mW

### 4.3.3. Confidence Model of Laser-Assisted Dielectric Breakdown

When an insulating membrane is continuously subjected to electric field stress, the number of traps in the membrane increases with time. Once the trap density reaches a critical value, the breakdown occurs [111, 113]. The time to breakdown is a stochastic process governed by the probability of forming a connected path across the membrane, following the Weibull distribution [111, 113],

$$f(t) = \frac{\beta}{\lambda} \left(\frac{t}{\lambda}\right)^{\beta-1} e^{-(t/\lambda)^\beta} \quad (4-2)$$

where  $f(t)$  is the breakdown probability after the electric field is applied for a time  $t$ ,  $\beta$  is the shape parameter which characterizes the steepness of the breakdown transition,  $\lambda$  is the characteristic lifetime at which 63% of membranes have experienced a breakdown. Note that the average breakdown time of a Weibull distribution can be derived from  $\lambda \Gamma(1 + 1/\beta)$ , which corresponds within  $\pm 10\%$  to  $\lambda$  for typical values of  $\beta$ . For simplicity, the characteristic lifetime  $\lambda$  was used to describe the average time to breakdown in the following context.

Two competing processes coincided with the typical laser-assisted dielectric breakdown setup. One is the normal breakdown, and the other is the laser-assisted breakdown (**Figure 4-1a** and **b**). The average time to breakdown in the areas with no laser can be estimated as [105, 111, 135],

$$\lambda_n = B e^{-\gamma E_n} \quad (4-3)$$

in which  $n$  stands for *normal*,  $B$  is integration constant (s), and the  $\gamma$  is the field acceleration factor (nm/V),  $E_n$  is the electric field.

At the laser spot, the electric field  $E_{la}(t)$ , will increase over time due to local etching of the SiN<sub>x</sub>. The breakdown efficiency (*i.e.*, percentage of failure created by unit time) is given by  $1/Be^{-\gamma E_{la}(t)}$ . If the same trap density is required for the breakdown to occur at the laser spot, one could estimate the average time to breakdown at the laser spot by (**Table 4-2**),

$$\int_0^{\lambda_{la}} \frac{dt}{Be^{-\gamma E_{la}(t)}} = \int_0^{\lambda_{la}} \frac{d_0^{-kt}}{d_0} dt \quad (4-4)$$

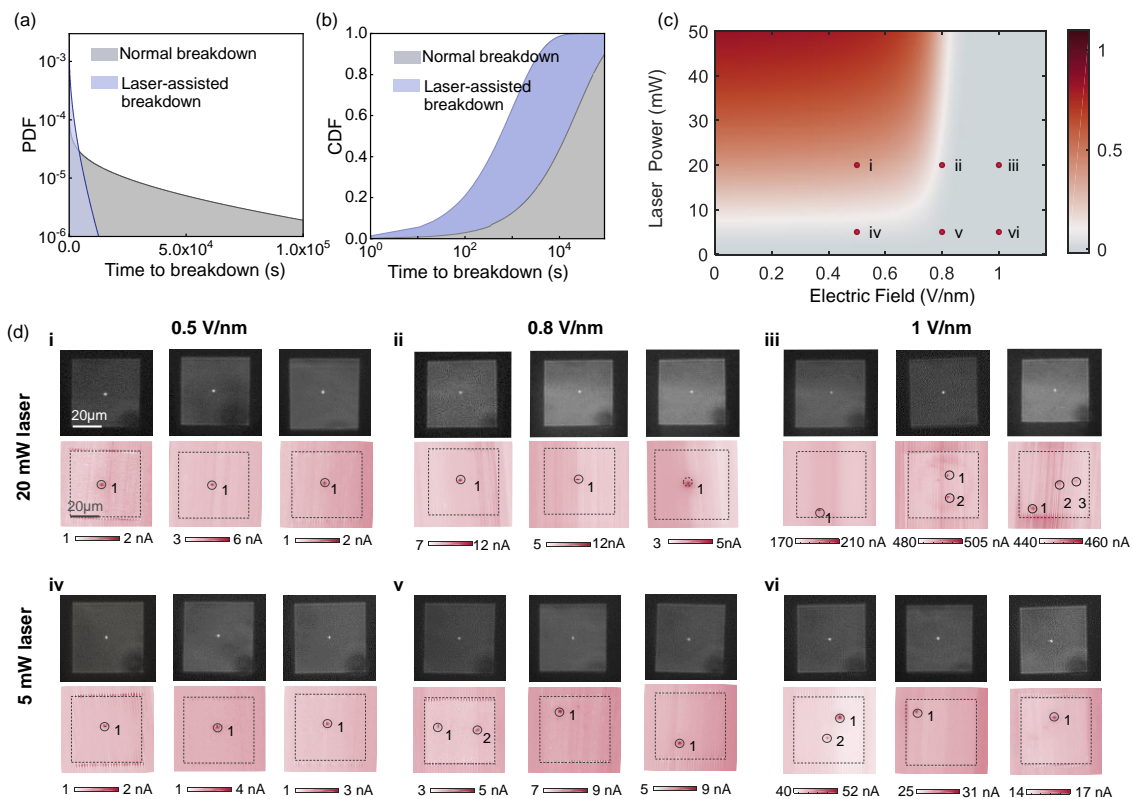
where  $la$  stands for *laser-assisted*,  $k$  is the laser power-dependent etching rate (**Eq.4-1**),  $d_0$  is the membrane thickness.

By estimating  $\lambda_n$  and  $\lambda_{la}$  using **Eq.4-3** and **Eq.4-4**, the time to breakdown distributions for the normal breakdown  $f_n(t)$  and for the laser-assisted breakdown  $f_{la}(t)$  can be assessed by **Eq. 4-2**. However, note that Weibull statistical parameters ( $\beta$  and  $\lambda$ ) remain unknown and could vary from lab to lab due to material and setup differences. One has to estimate these Weibull parameters from existing experimental data. Using our experimentally derived parameters (**Table 4-3**), **Figure 4-5a** shows a representative  $f_n(t)$  and  $f_{la}(t)$  profile. **Figure 4-5b** shows the cumulative distribution function (CDF) of the time to breakdown time. The overlapping of  $f_n(t)$  and  $f_{la}(t)$  indicates the uncertainty of nanopore localization. The smaller the overlap, the higher the probability of nanopore localization will be. One can estimate the confidence for forming the nanopore at the laser spot by using,

$$C = 1 - \int_0^{\infty} \min(f_n(t), f_{la}(t)) dt \quad (4-5)$$

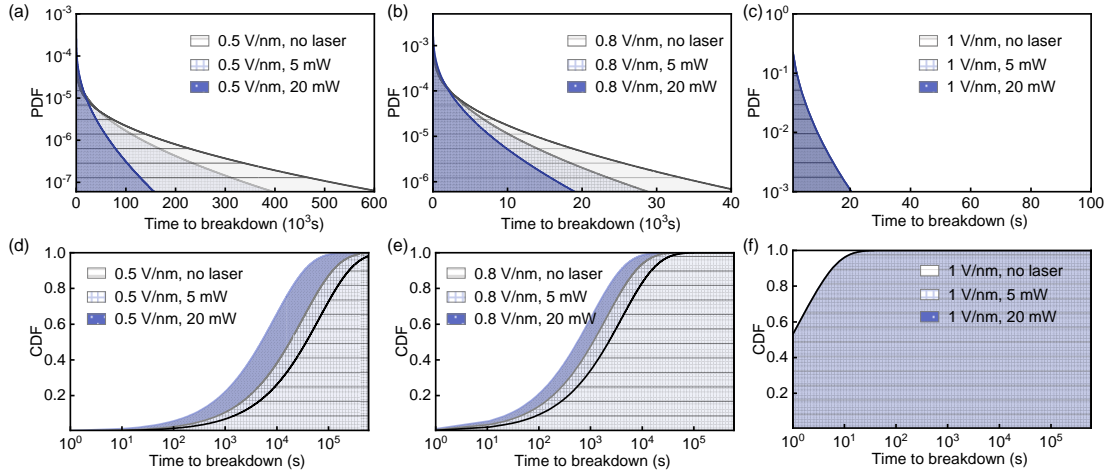
With this model, we can estimate the nanopore localization confidence under various combinations of laser power and electric field using our experiment-derived parameters. **Figure 4-5c** shows a

representative example (parameters for this plot were listed in (Table 4-4)). We observed several interesting features. First, low laser power could not help achieve nanopore localization due to the insignificant photothermal etching. The breakdown behavior in this region is equivalent to the normal CBD. Second, a high electric field always leads to random nanopore generation (confidence $\sim$ 0). This is because a high electric field can immediately break down the material at a random location, making the contribution of the laser-assisted etching irrelevant. Third, at a fixed low electric field, increasing the laser power could always enhance the confidence level. Note that the quantitative result in Figure 4-5c represents a specific case in our experiment and should not be generalized for other setups without knowing the material and experimental-specific parameters.




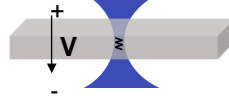
**Figure 4-5.** (a) PDF and (b) CDF of representative Weibull distribution of time to breakdown for the normal and laser-assisted breakdown. (Parameters: Normal breakdown: 0.6 V/nm; Laser-assisted breakdown: 0.6 V/nm and 50 mW laser;  $\lambda_n = 24501s$ ,  $\lambda_{la} = 1362s$ ,  $\beta = 0.63$ ). (c) Calculated confidence map of single nanopore localization at different laser powers and electric fields. Parameters used: integration constant  $B = 5 \times 10^{15}$  s, field acceleration factor  $\gamma = 38$  nm/V,

membrane thickness  $d_0 = 30$  nm, photothermal coefficient  $b = 8.06$  K/mW, shape parameter  $\beta = 0.63$ . (d) laser-assisted breakdown at different electric fields (0.5-1 V/nm) and laser powers (5 and 20 mW). The top panels are microscope images with bright spots showing the locations of the focused laser spot. The bottom panels are ionic current mapping results, performed at 4 mW laser power and 100 mV voltage with  $10 \mu\text{m/s}$  scanning speed. The PDF and CFD of all cases can be found in Figure 4-6.



**Figure 4-6.** (a-c) Probability density function (PDF) and (d-f) Cumulative distribution function (CDF) of Weibull distribution of time to breakdown for normal and laser-assisted breakdown at different electric fields (0.5-1 V/nm) and laser powers (5-20 mW).

**Table 4-2.** Comparison between normal breakdown and laser-assisted breakdown physics

	Normal Breakdown	Laser-assisted breakdown
		
Membrane thickness	$d_0$	$d(t) = d_0 - kt$
Total number of the traps to reach the critical trap density	$N_n = D \times S \times d_0$	$N_{la} = N_n \times \int_0^{t_{la}} \frac{d(t)}{t_{la} d_0} dt$
Electric field	$E_n = \frac{V}{d_0}$	$E_{la}(t) = \frac{V}{d(t)}$
Average breakdown time	$\int_0^{t_n} \frac{dt}{B e^{-\gamma E_n}} = 1$	$\int_0^{t_{la}} \frac{dt}{B e^{-\gamma E_{la}(t)}} = \frac{N_{la}}{N_n} = \int_0^{t_{la}} \frac{d(t)}{d_0} dt$

$d_0$ : Initial membrane thickness; k: Etching rate; S: Area; D: Critical trap density; V: Voltage

**Table 4-3.** Parameters used in Figure 3a & Figure 3b

Parameters	Meaning	Value	Unit	Sources
$k$	Etching rate	2.88	Å/min	Arrhenius fitting result in Figure 2e
$P$	Laser power	50	mW	
$V$	Voltage	18	V	
$d_0$	Initial membrane thickness	30	nm	
$B$	Integration constant	$5 \times 10^{15}$	s	Our experimental data[110]
$\gamma$	Field acceleration factor	38	nm/V	Published result[136]
$\beta$	Shape parameter	0.63	No Unit	Our experimental data[110]
$\lambda_n$	Average breakdown time (Normal)	24501	s	
$\lambda_{la}$	Average breakdown time (Laser-assisted)	1362	s	

**Table 4-4.** Parameters used in Figure 3c

Parameters	Meaning	Value	Unit	Sources
$k$	Etching rate	$Ae^{-\frac{E_a}{R(bP+T_0)}}$	Å/min	Arrhenius fitting result in Figure 2e
$A$	Arrhenius constant	31.6	Å/min	
$R$	Gas constant	$8.314 \times 10^{-3}$	kJ/mol/K	
$E_a$	Activation energy	13.7	kJ/mol	
$b$	Photothermal coefficient	8.06	K/mW	
$T_0$	Room Temperature	293	K	
$P$	Laser power	1-50	mW	
$V$	Voltage	1-35	V	
$d_0$	Initial membrane thickness	30	nm	
$B$	Integration constant	$5 \times 10^{15}$	s	Our experimental data [110]
$\gamma$	Field acceleration factor	38	nm/V	Published result [136]
$\beta$	Shape parameter	0.63		Our experimental data [110]

#### 4.3.4. Probing Specific Cases in the Confidence Model

Based on the confidence model, we experimentally probed the laser-assisted breakdown at different electric fields (0.5-1 V/nm) and laser powers (**Figure 4-5d**). We used our previously reported

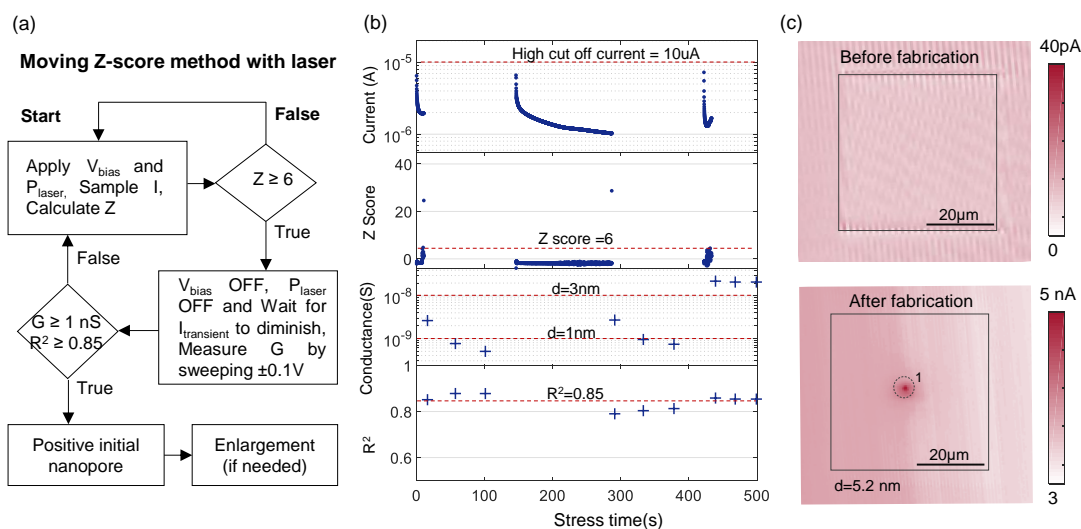
moving Z-score method for breakdown fabrication (flowchart shown in **Figure 4-7**) [110] and used the ionic current mapping method for nanopore location determination [130, 131].

**Figure 4-5d (i-iii)** shows the results from samples under 20 mW laser at different electric fields. The top microscope images show the laser spot location before the nanopore fabrication. The bottom ionic current scanning images show the nanopore location after the fabrication. At low electric field (0.5 V/nm) and intermediate electric field (0.8 V/nm), we observed a single ionic current enhancement in the laser spot. While the laser beam spatial resolution is insufficient to resolve if there are several nanopores within the laser focal spots, we believe it is unlikely to form multiple nanopores within the 1  $\mu\text{m}$  laser focal spot because the center of the etched pit has the highest electric field and is the most likely location for the initial breakdown (**Figure 4-3**). Therefore, the single ionic current enhancement is a good indication of a single nanopore at 0.5 V/nm and 0.8 V/nm. However, at a high electric field (1 V/nm, **Figure 4-5d (iii)**), the ionic current mapping showed that formed pores were not in the laser spot and could be random in numbers. The resulting ionic current is also much larger ( $>100$  nA). This uncontrolled nanopore generation at the high electric fields is consistent with model predictions. At high electric fields, relatively slow laser-assisted thinning can be easily overwhelmed by the fast electrical breakdown (**Figure 4-8**), rendering the benefits of laser irrelevant. We also tested different electric field conditions at a low laser power (5 mW, **Figure 4-5d (iv-vi)**). We observed the same trend that a high electric field can negatively impact the confidence of forming a single nanopore in the laser spot.

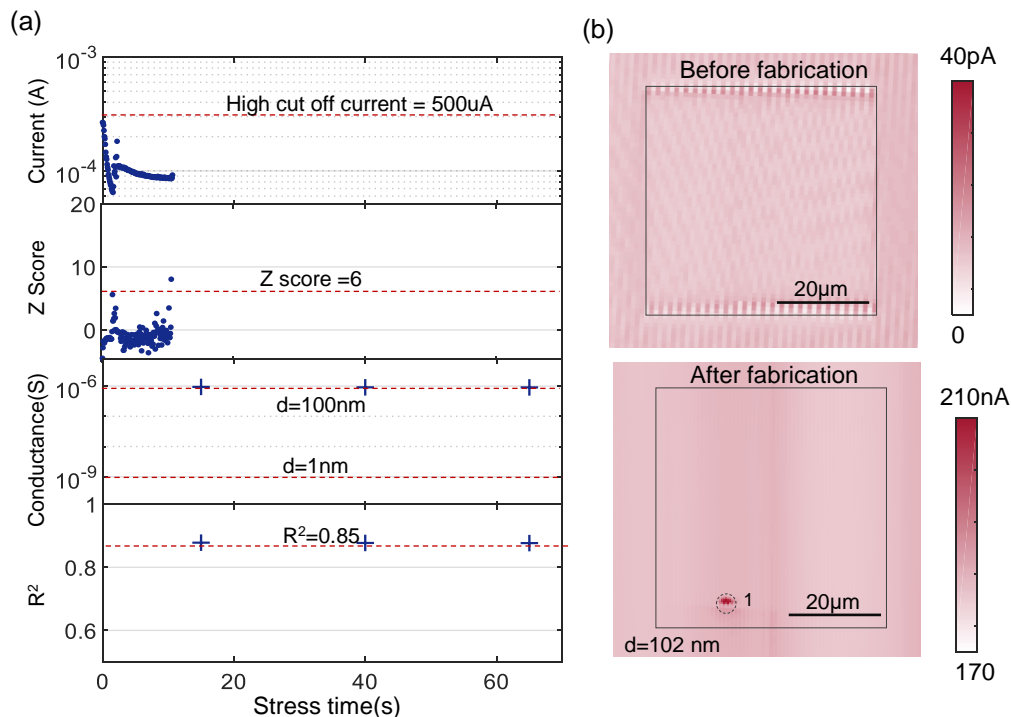
The behaviors of these representative cases and the normal breakdown fabrication result (**Figure 4-9**) showed a good agreement with the model predictions in **Figure 4-5c**. Both the model and experiment results suggested that a combination of high laser power and a low electric field is preferred towards single nanopore localization. Admittedly, a full examination of the confidence



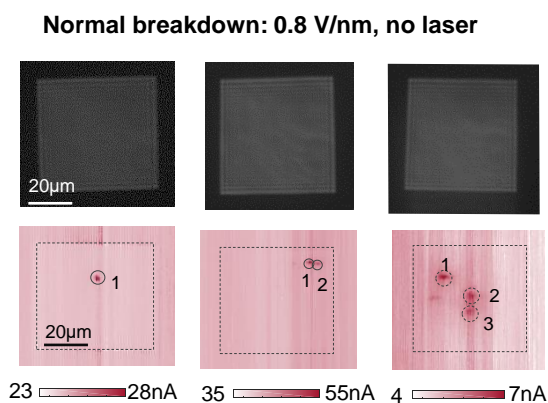
model would require testing many more samples by different labs to establish sufficient statistics in the future.



**Figure 4-7.** (a) Flowchart of the automated procedure for laser-assisted breakdown nanopore fabrication. The moving Z-Score is an online adaptive learning algorithm for detecting the abnormal points in a time-trace. It measures the number of standard deviations each new observation is away from the mean over a pre-defined time window length of  $w$ ,  $Z_k = \frac{I_k - \text{mean}(I_{k-1}:I_{k-w})}{\text{std}(I_{k-1}:I_{k-w})}$ . The detailed description of the moving Z-score method can be found in our previous work [110]. (b) A representative nanopore fabrication process at 0.8 V/nm and 20 mW. The nanopore diameter estimated by the conductance measurement was about 5.2 nm. (c) Scanned ionic current mapping before (top) and after (bottom) the nanopore fabrication. Ionic current mapping experiments were performed at 4 mW laser power and 100 mV voltage with 10  $\mu\text{m/s}$  scanning speed.



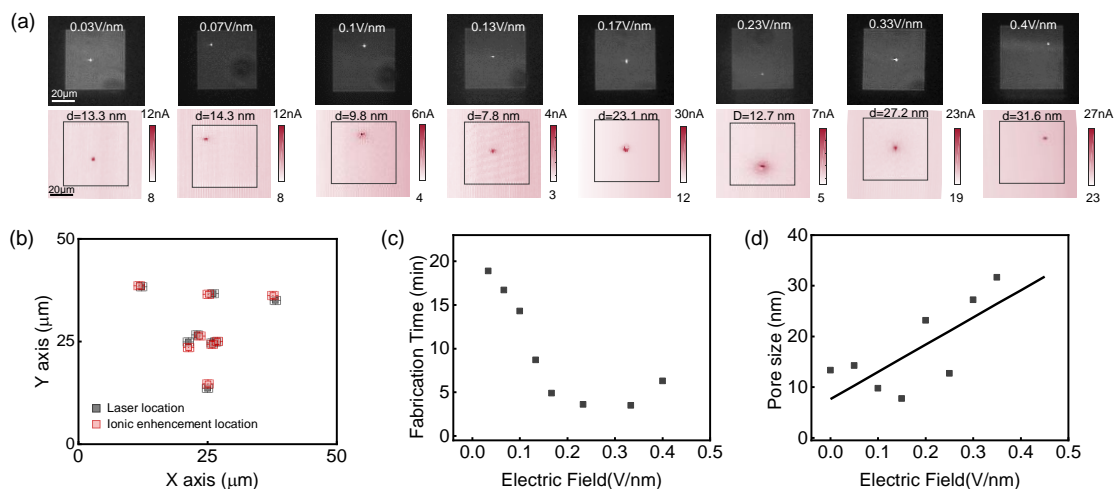
**Figure 4-8.** (a) A representative nanopore fabrication process at 1 V/nm initial electric field and 20 mW laser power. Nanopore was formed around 10 s. The nanopore diameter estimated by the conductance measurement was about 102 nm. (b) Scanned ionic current mapping before (top) and after (bottom) the nanopore fabrication. Ionic current mapping experiments were performed at 4 mW laser power and 100 mV voltage with 10  $\mu\text{m/s}$  scanning speed.



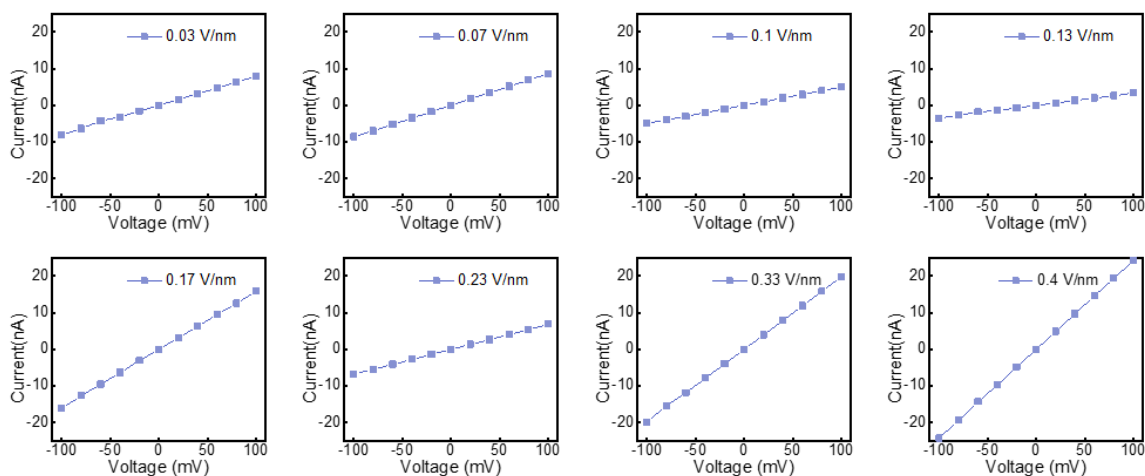
**Figure 4-9.** Normal breakdown at 0.8 V/nm without laser. The top figures are microscope images before fabrication. The bottom color maps are ionic current mapping results, which were performed at 4 mW laser power and 100 mV voltage with 10  $\mu\text{m/s}$  scanning speed.

### 4.3.5. Programmable Nanopore Fabrication

With the knowledge of the optimized conditions for single nanopore localization, we set out to test if the laser-assisted breakdown can be programmed to fabricate a single nanopore at an arbitrary spot. A total of 8 different samples were tested. We intentionally focused the laser spots at different places and varied the electric field from 0.03 V/nm to 0.4 V/nm (*i.e.*, low electric field). The top row of **Figure 4-10a** shows the laser spot location on the SiN<sub>x</sub> membrane before the breakdown. The bottom row of **Figure 4-10a** shows the corresponding ionic current mapping for determining the location and number of the formed nanopores. We observed a single ionic current enhancement in each of these samples, indicating a single nanopore. The nanopore position matched the laser spot location very well (**Figure 4-10b**). These results suggested a low electric field at 20 mW laser in a very robust combination for forming single nanopores at the laser spot in our setup. We also studied the impact of the electric field on the nanopore formation time and the nanopore size. Note that the fabrication time follows the Weibull distribution at a specific electric field [110]. It would require a significant number of breakdown experiments to probe the statistics at each electric field, which is tedious and costly to perform. Instead, we performed a single sampling at each electric field condition and examined the general trend. **Figure 4-10c** shows the relationship between the electric field and fabrication time. In general, the fabrication time decreases with the increasing electric field. **Figure 4-10d** shows the relationship between the electric field and the nanopore size, which was estimated from the ionic conductance measurement (**Figure 4-11**). As shown in **Figure 4-10d**, the nanopore diameter tends to decrease with reducing the electric field. This is because less enlargement can occur after the initial breakdown event happened at low electric field [110].



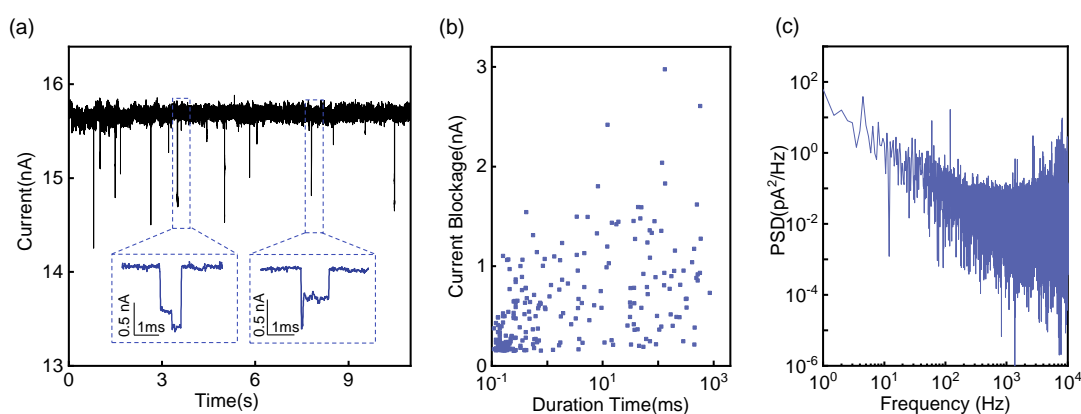
**Figure 4-10.** (a) Programmable laser-assisted breakdown fabrication using 20 mW laser and low electric field ranging from 0.03 V/nm to 0.4 V/nm. The bright spots in the top microscope images show the laser location. The bottom laser enhanced ionic current mappings show the number and location of the fabricated nanopores. All ionic current mapping experiments were performed at 2 mW laser power and 100 mV voltage with 20  $\mu\text{m}/\text{s}$  scanning speed. (b) Overlay of the extracted laser location and the formed nanopore location. The error bar indicates the full width at half maximum (FWHM). (c) The nanopore fabrication time as a function of the electric field. (d) The formed nanopore diameter as a function of the electric field. The nanopore diameter is determined by the IV measurement. The line in (d) is used to guide the eyes.



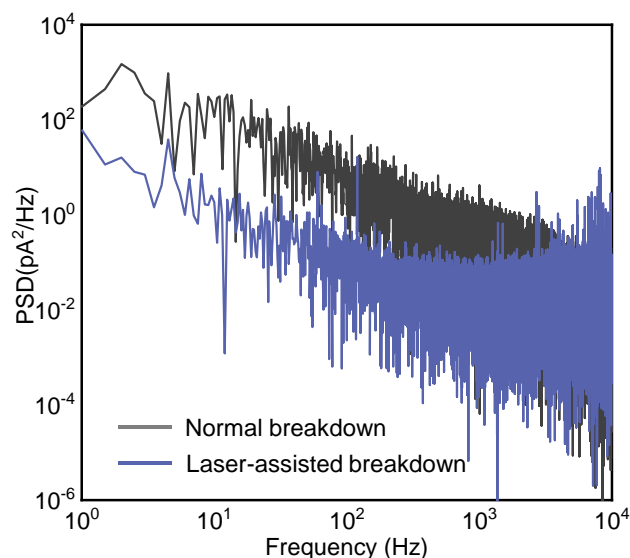
**Figure 4-11.** Conductance measurement. I-V curves of the nanopore fabricated by laser-assisted breakdown method at 20 mW laser and low electric field ranging from 0.03 V/nm to 0.4 V/nm. All measurements were performed in 1M KCl with 10mM Tris, and 1mM EDTA.

#### 4.3.6. DNA Translocation Experiments

To demonstrate the sensing performance of laser-assisted breakdown nanopores. We performed single molecule translocation experiments using 100 pM 48.5 kbp double-stranded  $\lambda$ -DNA. **Figure 4-12a** shows a representative time-trace of current using a nanopore of 10 nm diameter (estimated by the conductance measurement). The initially stable open pore current (15.7 nA) was interrupted by current blockage events of 0.3-3 nA magnitude. The magnified insets in **Figure 4-12a** show typical translocation event. Dual current blockage levels were captured, which reflects that the  $\lambda$ -DNA molecules translocated with the folded structure. **Figure 4-12b** shows a scatter plot of current blockages versus dwell time for a total of 238 translocation events. The average dwell time was 53 ms, and the average blockage was 0.6 nA, comparable to previous studies [31, 132].



**Figure 4-12.** (a) A representative current time-trace for 100 pM 48.5 kbp  $\lambda$ -DNA molecules translocating through a 10 nm nanopore at 300 mV bias. The magnified insets show two typical ionic current blockades during the translocation. (b) Scatter plot of the current blockades versus dwell time for a total of 238 translocation events. (c) Power spectrum density (PSD) of the ionic current obtained at 300 mV with a low-pass filter at 10 kHz.



**Figure 4-13.** Measured power spectral density (PSD) of the normal breakdown and laser-assisted breakdown nanopore. The estimated pore diameter of normal breakdown methods and laser-assisted breakdown method are 9 nm and 10 nm respectively. All experiments were performed with 1 M KCl at 300 mV with a low-pass filter at 10 kHz.

To confirm the current drop indeed stems from the single molecule translocation through a single nanopore and verify the nanopore size, we examined the ratio of blocked pore current ( $i_b=15.1$  nA) to the open pore current ( $i_0=15.7$  nA) as  $i_b/i_0 = 1 - d_{DNA}^2/d^2$ , in which  $d_{DNA}$  and  $d$  are the diameter of DNA (2.2 nm) and the diameter of the nanopore, respectively [137]. The estimated nanopore diameter using the above method is about 11 nm, which is in excellent agreement with the diameter estimated by the IV measurement (10 nm). This agreement confirmed that a single nanopore was formed in the fabrication and the current drop indeed stems from the single molecule translocation.

**Figure 4-12c** shows the power spectrum density (PSD) of the ionic current. The root-mean-square (RMS) noise at 10 kHz bandwidth was about 30 pA, sufficiently small for distinguishing typical single molecule events with dip magnitude  $>300$  pA. It is noteworthy that the nanopores formed by the laser-assisted breakdown method exhibited a stable baseline current and reduced noise,

comparing with nanopores fabricated by the normal breakdown (**Figure 4-13**). The exact mechanism behind the improved noise performance using laser-assisted breakdown fabrication warrants further exploration.

#### **4.4. Summary**

In conclusion, we studied the laser-assisted dielectric breakdown for localizing a single nanopore at a programmed location with the aim of addressing the stochastic issue in the normal breakdown method. A statistic model was developed to estimate the confidence of nanopore localization at different laser powers and electric fields. We experimentally probed three representative regions of the confidence map, and the results were qualitatively consistent with model predictions. Future work will focus on gathering more experimental data to test this model. While the utility of this model is subject to parameter variations in membrane material properties, laser wavelength, and electrolyte, we found that a combination of high laser power and low electric field was generally favorable for forming a single nanopore at the laser spot. The nanopore fabricated by laser-assisted dielectric breakdown exhibited excellent noise performances [138] for single-molecule translocation experiments. We believe this study provided significant experimental insights into optimizing the laser-assisted dielectric breakdown and would enable broader access to robust solid-state nanopore fabrication and sensing applications.

## **Chapter 5 Saliva-Based SARS-CoV-2 Self-Testing with RT-LAMP in A Mobile Device**

The integrated molecular diagnostics device typically has four essential steps: (1) cells or virus particles lysis and DNA or RNA extraction, (2) sample partition by pipetting or microfluidic device, (3) target sequence amplification, (4) real-time detection by optical or other types of sensing mechanism. In Chapter 5, we developed a fully integrated nucleic acid testing (NAT) device for SARS-CoV-2 detection. This platform consists of a ready-to-use reagents cartridge, an easy-to-use smartphone interface, and an ultra-compact and less-expensive analyzer. This system can automatically handle the complexity of heat-inactivated sample preparation, the pressure-driven sample dispensing, real-time RT-LAMP reaction and detection, and data processing. With a turnaround time of ~45 minutes, we achieved a limit of detection (LoD) of 5 virion/ $\mu\text{l}$  of a saliva sample using traditional optical detection method. The performance of the developed prototype (analyzer and cartridge) also evaluated with the using nanopore counting method. Therefore, the success completion of this project will pave the way for ultracompact, rapid, and affordable nanopore-based nucleic acid testing.



## 5.1. Introduction

Coronavirus disease 2019 (COVID-19) became a worldwide pandemic in early 2020 [139], and it was rapidly announced as a public health emergency of international concern by the World Health Organization (WHO) [140, 141]. As of March 2022, there are more than 400 million confirmed cases and 6 million deaths of SARS-CoV-2 reported globally [141]. A lot of effort has been made into vaccine development, and it has been distributed in communities [142]. However, due to the fast mutation nature of the RNA virus and so many asymptomatic cases, all countries still face an unmet need to achieve a rapid, sensitive and reliable way to tackle the global and urgent problem. To reopen the communities and recover the economy, implementing routine level screening of healthy individuals should be a solution to minimize the risk of spreading. So far, Nucleic Acid Amplification Test (NAAT), such as RT-PCR, is the gold-standard technique due to its high sensitivity and specificity [84, 143-145]. However, laboratory-based NAAT requires highly trained personnel, dedicated facilities, and instrumentations. Typically, results can be done within 2 hours, but many counties usually delay up to 7 days due to lack of facilities. Postponing obtaining molecular testing results will increase the virus spread. To alleviate these bottlenecks, the COVID-19 antigen rapid test (Ag-RDT) is one of the practical options [146, 147]. These antigen tests can identify active infection by detecting SARS-CoV-2 viral proteins and can be processed and read visually by patients within 15–20 min using a small portable device [148, 149]. Although these tests are much faster and cheaper, they are generally not as sensitive as molecular tests [147, 150]. Especially after the acute phase, when the viral load decreases, Ag-RDT might lead to high rates of false negatives, which could miss a significant portion of infected patients. To overcome the drawbacks of the conventional nucleic acid amplification test and the rapid antigen test, an ultra-portable, self-contained point-of-care (POC) nucleic acid amplification test for diagnosis of active COVID-19 infection will be the answer for rapid and accurate detection.

The integrated molecular diagnostics device typically has four essential steps: (1) cells or virus particles lysis and DNA or RNA extraction, (2) sample partition by pipetting or microfluidic device, (3) target sequence amplification, (4) real-time detection by optical or other types of sensing mechanism[151, 152]. The integration of the sample preparation is critical to speed up this whole process. Since August 2020, saliva has become an alternative sample type for SARS-CoV-2 detection. Several studies have demonstrated that saliva has comparable performance with nasopharyngeal samples[153]. Compared with the nasal swab sample, the saliva sample is simple to self-collect but can be directly processed without dilution in the transport medium. More importantly, Yale school of public health has significantly simplified the saliva sample preparation step. Only Performing 5 minutes of heat-inactivation of the saliva sample can achieve a low limit of detection (6 copies/ $\mu$ L) using FDA-proved RT-PCR assays [154]. This easy, noninvasive method can largely increase the accessibility of self-testing [22, 77, 78, 83, 84, 154, 155].

Recently, isothermal amplification techniques have been widely used for the point of care setting, for example, reverse transcription loop-mediated isothermal amplification (RT-LAMP) [14, 15, 18, 19, 21, 27, 68, 76, 84, 85, 156-162]. The RT-LAMP process is similar to conventional PCR tests, but the reaction can be performed without commercial thermocyclers. While maintaining specificity and sensitivity comparable to that of the PCR tests, RT-LAMP shows better tolerance for the impurities and a faster time to result. These unique features make RT-LAMP assays quicker, easier to use, and more cost-effective than RT-PCR assays, making them more suitable for POC diagnostics.

In this work, we developed a fully integrated SARS-CoV-2 nucleic acid testing (NAT) device using a self-collected saliva sample. SLIDE platform consists of a ready-to-use reagents cartridge, an easy-to-use smartphone interface, and an ultra-compact and less-expensive analyzer. It automatically handled the complexity of heat-inactivated sample preparation, the pressure-driven

sample dispensing, and real-time RT-LAMP reaction and detection, and data processing, storage, and upload. With a turnaround time of ~45 minutes, we achieved a limit of detection (LoD) of 5 virion/ $\mu$ l of a saliva sample using the traditional optical method. The performance of the developed prototype (analyzer and cartridge) also evaluated with the using nanopore counting method. Therefore, the success completion of this project will pave the way for ultracompact, rapid, and affordable nanopore-based nucleic acid testing.

## **5.2. Experiment section**

### **5.2.1. SARS-CoV-2 samples**

The heat-inactivated SARS-CoV-2 virus particles were spiked into the extracted saliva RNA solution at concentrations ranging from 10 to  $10^5$  copies/ $\mu$ l. Typically 10  $\mu$ l of the mock sample was used in the reaction unless otherwise stated. Heat-inactivated SARS-CoV-2 (ATCC® VR-1986HK™) virus particle was purchased from ATCC. The negative saliva samples were collected from healthy volunteers. These pre-identified clinical saliva samples were approved by the institutional review board (IRB) of the Pennsylvania State University Hershey Medical Center (study number STUDY00016633). These saliva samples were initially tested with the F.D.A. EUA-Authorized Simplexa RT-PCR COVID-19 Direct assay (DiaSorin Molecular, Cypress, CA, USA). The collected saliva samples were frozen at  $-80^{\circ}\text{C}$  before use. All the clinical experiments were performed in the Animal Diagnostic Laboratory (BSL 3) at Penn State, University Park by a protocol approved by the Institutional Biosafety Committee.

### 5.2.2. RT-LAMP reaction mix

The total volume of the RT-LAMP assays contains a 30  $\mu$ l master mix and 10  $\mu$ l saliva sample. The master mix includes isothermal buffer, PCR grade H<sub>2</sub>O, MgSO<sub>4</sub> (7 mM), Syto-9 green (10  $\mu$ M), deoxyribonucleotide triphosphates (dNTPs, 1.4 mM), Bst 2.0 DNA polymerase (0.4 U/ $\mu$ l), Warmstart reverse transcriptase (0.3 U/ $\mu$ l), primer sets (0.2 mM F3 and B3c, 1.6 mM FIP and BIP, 0.8 mM LF and LB, Table 3-2 see for primer design targeting N region). Table 5-1 summarizes the RT-LAMP recipe. The reaction was performed at a constant temperature of 65°C using either a benchtop PCR instrument (Bio-Rad CFX96) or a customized heat block.

**Table 5-1.** RT- LAMP Master mix in SLIDE Test

Components	Working Concentration (40 $\mu$ l)
FIP/BIP primers	1.6 $\mu$ M
F3/B3 primers	0.2 $\mu$ M
LF/LB primers	0.4 $\mu$ M
Isothermal Amplification	1x
MgSO <sub>4</sub>	6 mM
Betaine	0.4 M
dNTP	1.4 mM
syto-9 green fluorescent	10 $\mu$ M
Bst 2.0 DNA polymerase	10 U
WarmStart Reverse Transcriptase	7.5 U
Saliva sample	10 $\mu$ l
UP Water	1 $\mu$ l

### 5.2.3. Instrumentation

The SLIDE analyzer comprises 3D printed structural parts, a CNC machined aluminum heating block, a piezo pump, electronics such as an Arduino Nano (MCU), excitation LEDs, and color sensors for fluorescence detection, Bluetooth. The 3D housing was designed in Solidworks

software and printed using MakerBot MethodX 3D printer (Brooklyn, NY) with MakerBot ABS (acrylonitrile butadiene styrene). The aluminum heating blocks were designed in Solidworks software and fabricated using a CNC machine. Two one-ohm power resistors and one-ohm power resistors and mounted (in series) on the aluminum heating using a thermally conductive adhesive paste for 95°C heating block and 65°C heating block, respectively. Negative thermal feedback control was performed using N-channel power MOSFET (63J7707, Digi-Key) and an MC65F103A 10 k-ohm thermistor (Amphenol Thermometrics, St. Marys, PA) to maintain the desired temperature. PCBs were designed in AutoDesk Eagle CAD software and fabricated by O.S.H. Park L.L.C. (Lake Oswego, OR). The optical module PCB consists of three blue excitation LEDs (FD-5TB-1) purchased from Adafruit Industries (New York, NY) and three-color sensors (TCS 34725) purchased from DigiKey. The piezo pump was purchased from Bartels (Mikrotechnik, Germany). The Bluetooth (Adafruit Bluefruit LE SPI Friend) module was purchased from Adafruit Industries (New York, NY). The whole system was power by a 1300 mAh Lithium polymer battery (ZIPPER, USA). The total cost of each instrument is about \$ 241 (See bill of material **Table 5-5**), and the PCB designs are shown in **Figure 5-14**.

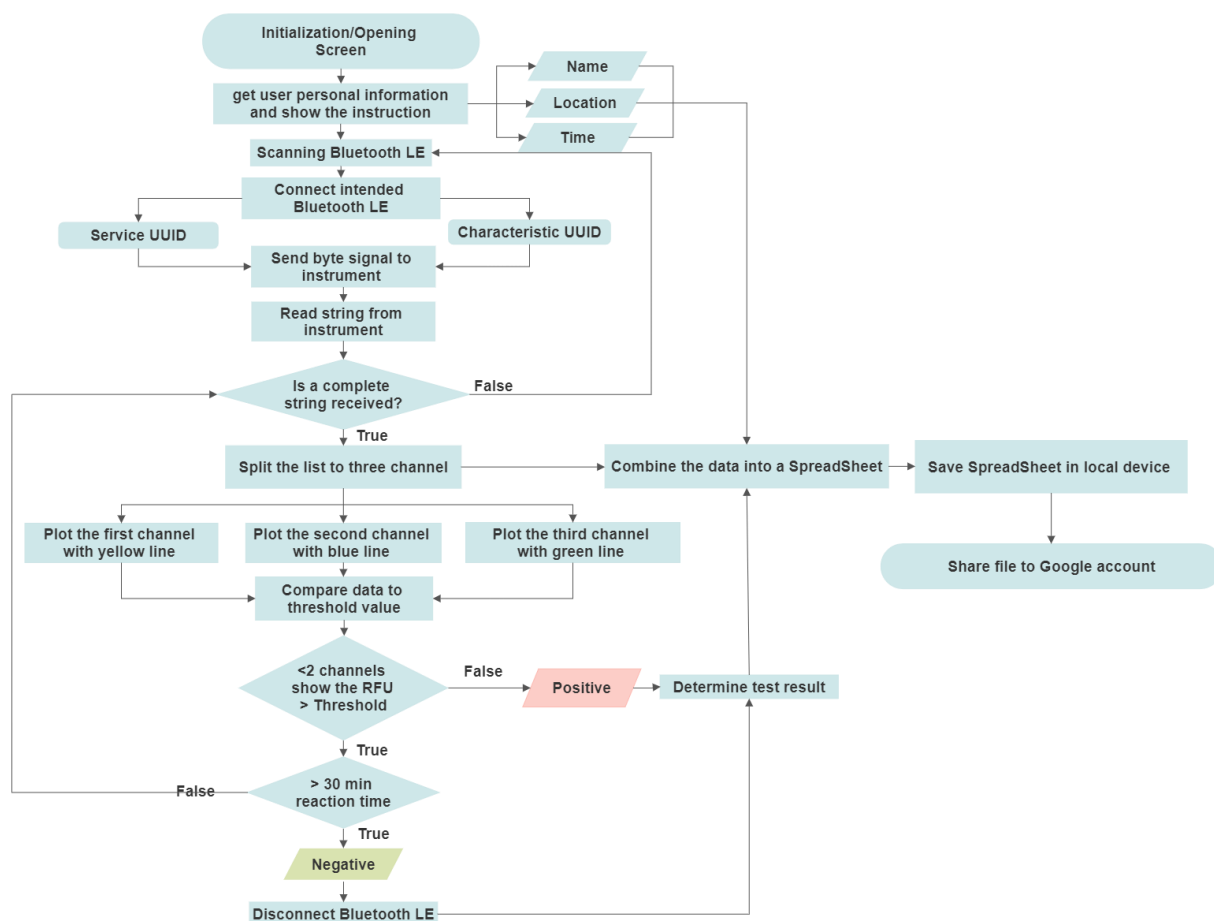
#### **5.2.4. APP development**

Four steps are involved in this android App development. First, the App interface guides users to provide their personal information. Only the name is required from users. The Global Positioning System (GPS) can automatically obtain the time and location information. Second, we set up Bluetooth communication. App interface scans and connects the Bluetooth LE around the analyzer. The communication protocol can be built using the Service UUID and Characteristic UUID of the Bluetooth LE, enabling the data communication function between these two devices. Once the user clicks the confirm button on the screen, the App will send a single bit to the analyzer to initiate the

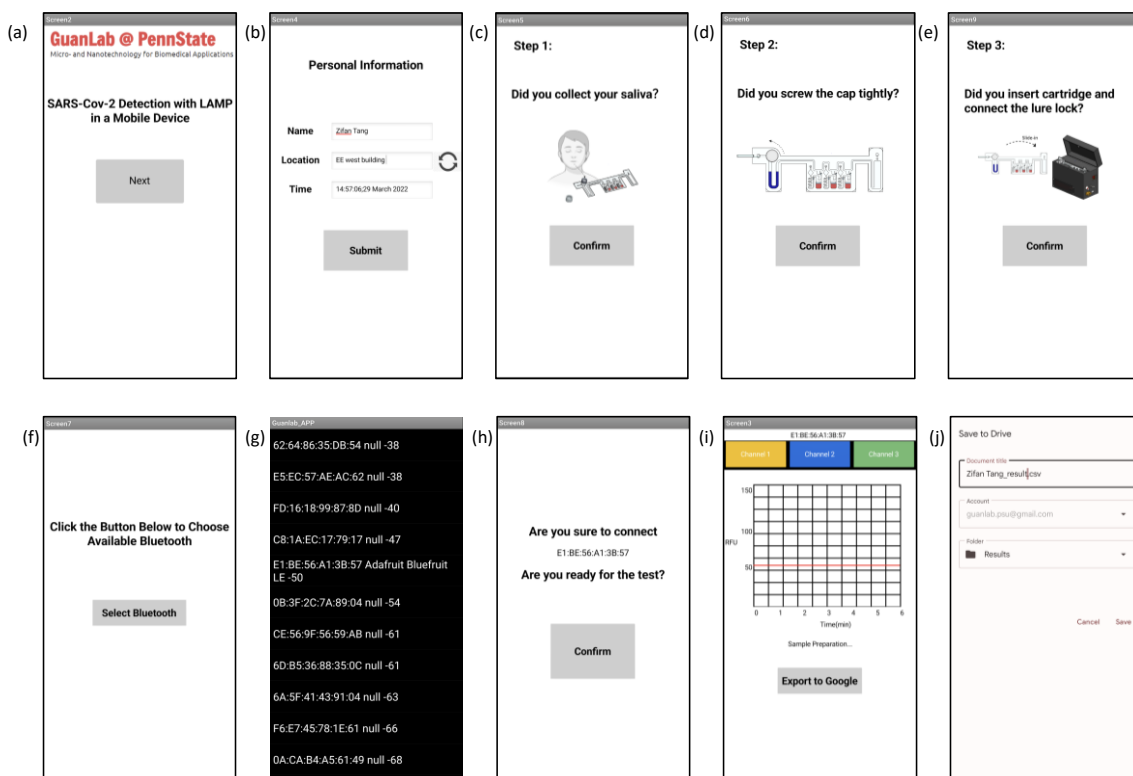
test. The third part is the real-time data transfer and plotting. We added two check bits at the beginning and the end of the string to ensure accuracy. After confirming the check bit of the received string from the analyzer, the string value will be split into three channels and plotted with different colors. Meanwhile, the split data in each channel is compared with the threshold value (RFU 50) to make the decision. If more than or equal to two channels have three successive data greater than the threshold, the test result will be identified as a positive. Otherwise, the App will continue to receive the string value from the analyzer. If no positive result has been determined after 30 minutes of the amplification, the test result will be negative. In the end, the APP will combine personal information, color sensor data in each channel, and test results into a spreadsheet. This file can be saved on the local device and uploaded to a Google drive. The flow chart of this APP development process is shown in **Figure 5-1** Selected screenshots of the APP are presented in **Figure 5-2**.

#### **5.2.5. Microfluidic reagent cartridge**

The microfluidic cartridge was designed by AutoCAD and patterned using a CO<sub>2</sub> laser cutting machine (Universal Laser Systems, Scottsdale, AZ). All layers were aligned and laminated with an adhesive solvent (Weld-On). The assembled cartridge comprises a sample collection chamber (200  $\mu$ l), three trapping chambers (10  $\mu$ l each), three reaction chambers (60  $\mu$ l each), three wax valves 1 (5  $\mu$ l each), three wax valves 2 (5  $\mu$ l each), and wastes chamber (300  $\mu$ l). The sample collection tube was mounted using the Epoxy Adhesive (3M, Saint Paul, MN). All the assay and wax valves are loaded onto the cartridge through the extruded inlet and sealed by the PCR plate seals (Bio-Rad, Hercules, CA).



**Figure 5-1.** The flow chart of the android App development. First, the App interface guides users to provide their personal information. Second, we set up Bluetooth communication. App interface scans and connects the Bluetooth LE around the analyzer. The communication protocol can be built using the Service UUID and Characteristic UUID of the Bluetooth LE, enabling the data communication function between these two devices. The third part is the real-time data transfer and plotting. We added two check bits at the beginning and the end of the string to ensure accuracy. After confirming the check bit of the received string from the analyzer, the string value will be split into three channels and plotted with different colors. Meanwhile, the split data in each channel is compared with the threshold value (RFU 50) to make the decision. If more than or equal to two channels have three successive data greater than the threshold, the test result will be identified as a positive. Otherwise, the App will continue to receive the string value from the analyzer. If no positive result has been determined after 30 minutes of the amplification, the test result will be negative. In the end, the APP will combine personal information, color sensor data in each channel, and test results into a spreadsheet. This file can be saved on the local device and uploaded to a Google drive.

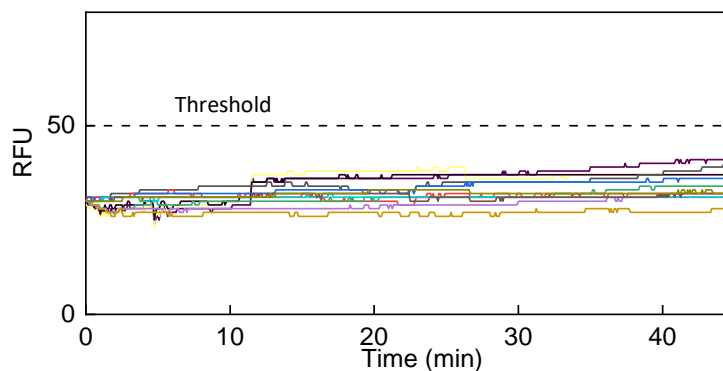


**Figure 5-2.** Mobile phone user interface and result unloading. The Android SLIDE application guides the user through steps to set up and run the test. (a-b) Collect user information. (c-e) Instructions for the user to collect samples. (f-h) Selection of the Bluetooth and the test initiation. (i) Real-time analysis during the test (g) Upload the testing result to local or Google drive.

### 5.2.6. Data processing

To uniform the curve and find the proper threshold for identify the positive from negative result, all the collected raw data is subtracted from the background signal acquired from the average of the first 10 data points and set at RFU 30. The threshold to classify an amplification curve as positive or negative was 50 RFU based on the negative sample (**Figure 5-3**).





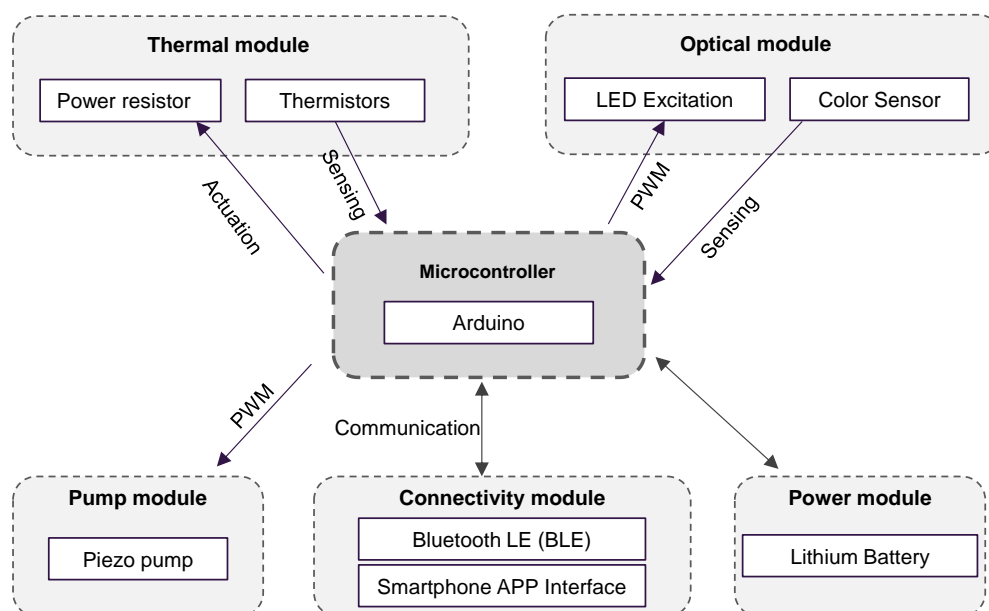
**Figure 5-3.** Representative measurement for 9 negative control samples. All of the samples were measured for 45 minutes. The baseline varies from RFU 28 to 42. Therefore, we set the RFU 50 as the threshold to avoid false positives.

### 5.3. Result and discussion

#### 5.3.1. Overall Design and Module Validations

**Overall Design.** The overall design of the SLIDE analyzer is shown in **Figure 5-5 a**. It consists of five seamlessly integrated modules controlled by a microcontroller unit (MCU): an optical module for fluorescence excitation and detection, two thermal modules, a piezo micro pump module, a power module, and a connectivity module. **Figure 5-4** illustrates the overall block diagram design of the device. The whole system is designed in SolidWorks and prototyped with an in-house 3D printing. **Figure 5-5b** shows a photograph of the assembled SLIDE analyzer and the smartphone interface.

**Optical Module.** The optical module consists of three independent excitation and detection units. Each unit has a LED excitation source ( $\lambda=470$  nm) and a CMOS color sensor for real-time fluorescence monitoring. The excitation and the detection were arranged to be perpendicular to each other to minimize the excitation interference on the fluorescence signal (**Figure 5-5c**). To



**Figure 5-4.** System diagram. An Arduino nano microcontroller incorporates five subsystems: thermal modules, optical module, pump module, connectivity module, and power module.

characterize the quantification ability of the optical module, we tested different calcein concentrations from 0 to 25  $\mu\text{M}$  and measured the fluorescence intensity for 10 minutes. **Figure 5-5** showed the mean and standard deviation of the relative fluorescence unit (RFU) as a function of the calcein concentration. A linear fit with  $R^2 = 0.98$  confirmed the quantitative capability of the optical module.

**Thermal Module.** We designed two independent thermal modules. One is for heat-inactivating the saliva and performing the thermal lysis at 95°C. The other is for controlling the temperature of the RT-LAMP reaction at 65°C. Both modules used a customized aluminum heating block with power resistors attached. The temperature was controlled through a feedback measurement of a thermistor embedded in the heating block. Since the temperature was obtained from the heating block rather than the analyte solution on the cartridge, we characterized the temperature profile difference between these two. As shown in Figure 5-5e, the heating block reached 95 °C after 2

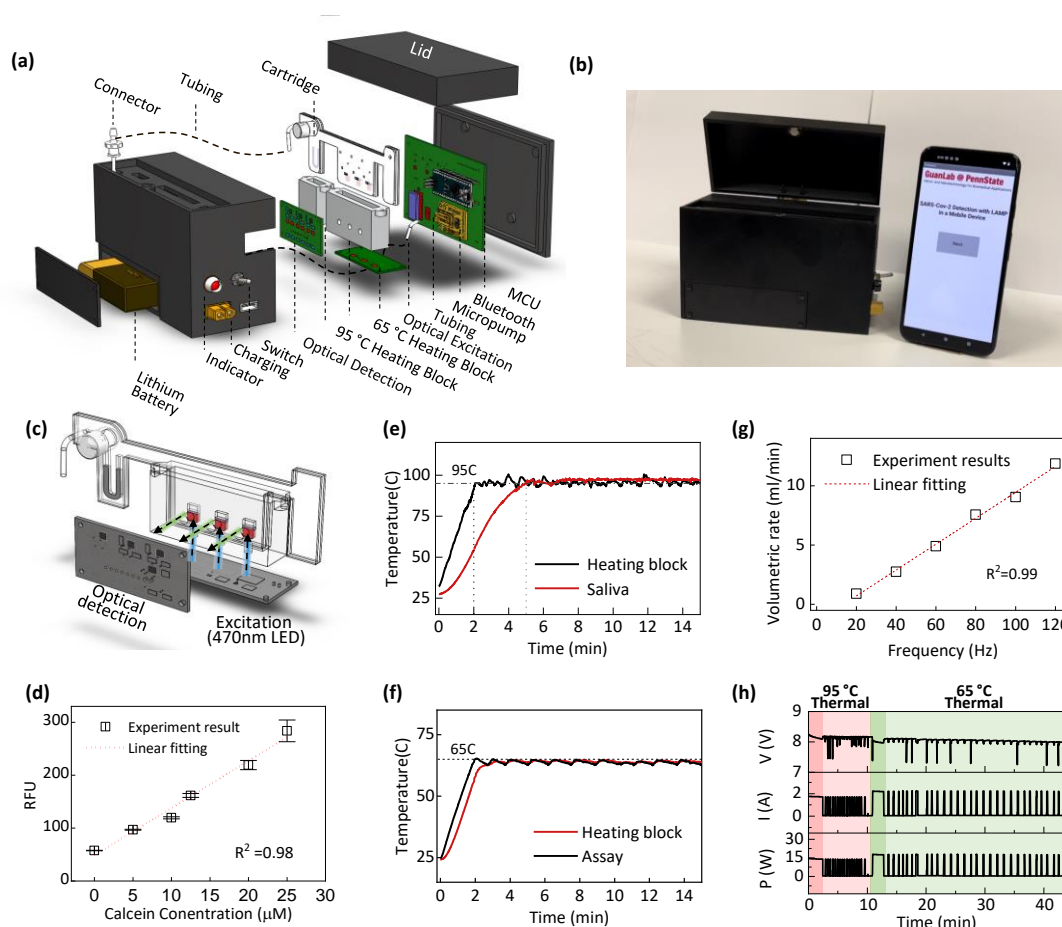
mins of operation, while the saliva in the cartridge took 5 mins. This delay is due to the non-ideal thermal coupling and the different specific heat capacity between the heating block and the cartridge. Nevertheless, the saliva can be sufficiently lysed at 95°C for 5 min within 10 mins from a cold start. For the heating module controlling the RT-LAMP reaction, we observed that the mean and the standard deviation of the temperature in the master mix solution is 64°C and 0.38°C, respectively.

**Micro pump Module.** The sample dispensing and mixing is accomplished on the cartridge using a micro piezo pump. It is connected to the microfluidic cartridge using a Tygon tube and a Luer-lock adaptor. The volumetric rate of the micro piezo pump is controlled by the frequency and the driving voltage (fixed at 140 V in our case). To characterize the micro pump, we tested the volumetric rate at different frequencies. As expected, the volumetric rate increased linearly with the operation frequency ( $R^2= 0.99$ , Figure **5-5g**). This relationship provides us with the capability to modulate the liquid flow rate on the cartridge through programming the operation frequency.

**Power Module.** A rechargeable 1300 mAh Lithium polymer battery (14.43 Wh) was used to power our analyzer. To estimate the power consumption for each run, we used a power meter to characterize the voltage, current, and power during a complete cycle of the test. Figure **5-5h** shows a complete-time trace. As shown, the heating is the most power-hungry process during the operation. Before reaching the target temperature, the heaters continuously work at a high current (1.7 A for 95 °C and 2.2 A for 65 °C). After reaching the target temperature, the heater starts to change states between on and off to maintain the temperature. The total energy consumed is 3.02 Wh in each 45 minutes test, meaning we can perform at least four tests before recharging.

**Connectivity Module.** A smartphone app was developed to assist the user in conducting the test. The flow chart of the app process is shown in **Figure 5-1**. The SLIDE analyzer and the smartphone

communicated through Bluetooth LE protocol. The App could provide test instructions, acquire data, and make positive and negative calls to easily interpret the test results. The App could also save the test results into a spreadsheet, which could be saved on the local smartphone or uploaded to cloud-based storage (Google Drive). **Figure 5-2** shows the representative screenshots of the developed App.



**Figure 5-5.** SLIDE Instrument design and validation. (a) Schematic of the SLIDE device showing components in an exploded view. The platform consists of five main functional modules: optical module (LED/optical sensor), thermal modules (power resistor/thermal sensor), micro pump modules, power supply module (battery), and data connectivity modules (Bluetooth). Each module was controlled by a microcontroller on a customized PCB board. (b) Photograph of the SLIDE analyzer and the smartphone interface. (c-d) Characterization of the optical sensor using 40  $\mu\text{l}$  calcein solution for 10 minutes of recording. The optical sensor showed a linear response to the concentration of calcein from 0 to 25  $\mu\text{M}$ . The temperature profile of the heating block and the liquid (saliva/assay) for (e) 95°C virus heat inactivation and 65°C RT-LAMP reaction. (g) Characterization of the piezo pump frequency with the flowrate. (h) Characterization the power

consumption for one test.

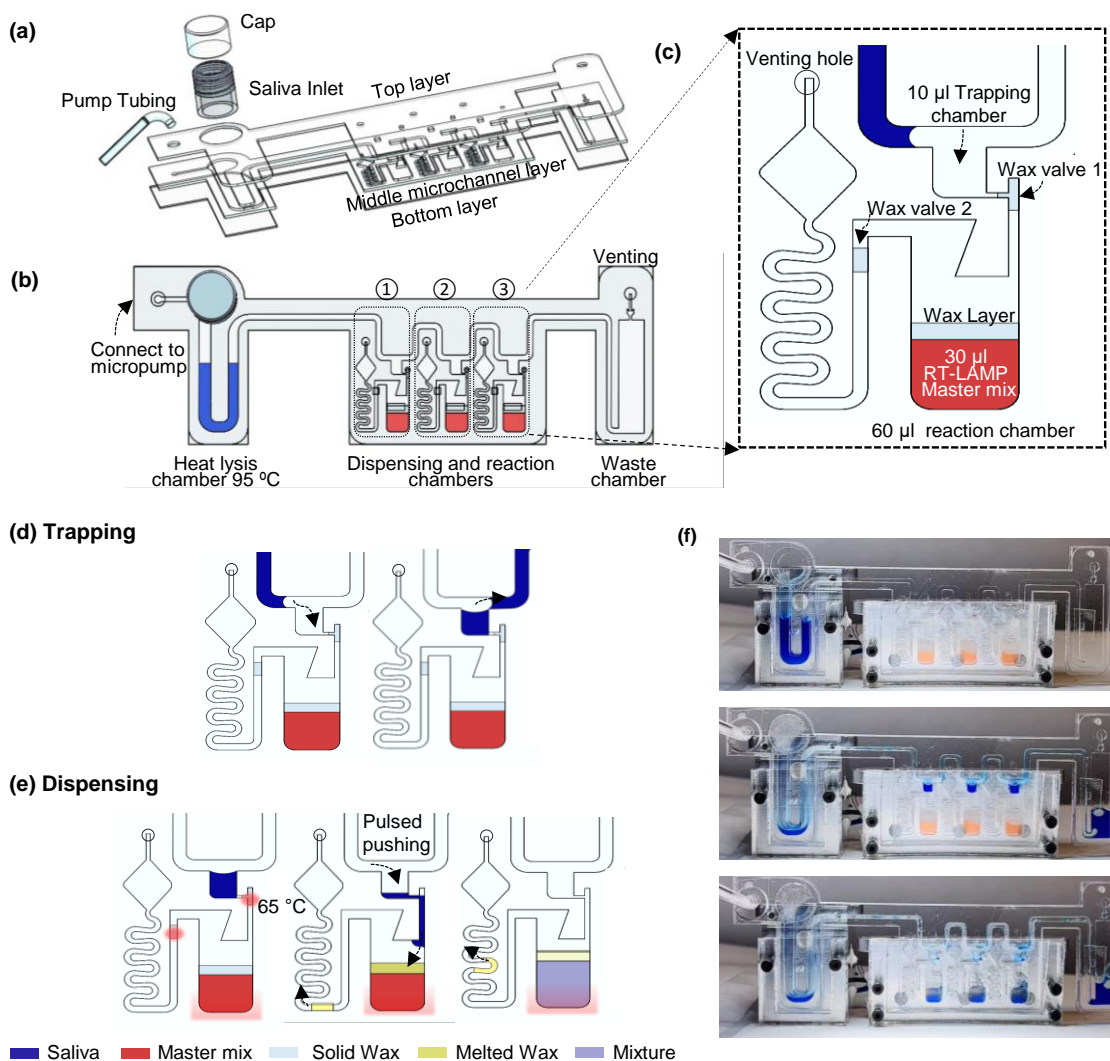
### 5.3.2. Automated Salvia Processing on The Cartridge

To facilitate the raw salvia processing, we developed a disposable cartridge with the SLIDE analyzer. The cartridge was fabricated in polymethyl methacrylate (PMMA). It consists of three laminated layers: top layer, middle microchannel layer, and bottom layer (**Figure 5-6a**). The overall layout of the assembled cartridge shows in **Figure 5-6b**. It includes a heat lysis chamber (250  $\mu$ l), three independent dispensing (10  $\mu$ l) and reaction chambers (60  $\mu$ l), and a waste chamber (300  $\mu$ l). First, the collected raw saliva sample was heat-inactivated and lysed at 95°C for 5 minutes. The resulting lysates were transferred to the dispensing and reaction chambers through the microchannel. The excessive analyte sample was stored in the wastes chamber with a venting hole to the atmospheric pressure.

**Figure 5-6c** illustrates the detailed design of a single unit of dispensing and reaction chambers. Since the laser-processed PMMA side walls are hydrophilic[25], a side pocket structure can easily trap 10  $\mu$ l of the samples without bubbles. We found the flow rate at 5.3 ml/min could help ensure the reliable trapping process. During the trapping process, the paraffin wax valve 1 was in the solid phase such that the trapping volume was fixed (**Figure 5-6d**). The average trapping volume is  $10.25 \pm 0.27$   $\mu$ l. The difference between the three chambers was less than 2.5%.

After excessive samples were pushed into the waste chamber and each unit metered 10  $\mu$ l of the heat-processed saliva, we increased the temperature to 65 °C to open the paraffin wax valves. When the wax valves 1 and 2 change from the solid phase to the liquid phase, the trapped saliva sample will start flowing into the reaction chamber by capillary force. To facilitate transferring all samples into the reaction chamber and thorough mixing with the RT-LAMP master mix, we applied 30

consecutive micro pump pressure pulses. Each pulse is programmed to be 100 ms in duration (Figure 5-6e). in duration (Figure 5-6e). The paraffin wax valve 2 serves as a hydraulic resistor,



**Figure 5-6.** (a) Exploded view of the cartridge with three PMMA layers: top-loading layer, middle microchannel layer, and bottom covering layer. (b) Assembled view of the cartridge includes a saliva collection chamber (250 µl), three trapping chambers (10 µl), three reaction chambers (60 µl) with preloaded RT-LAMP master mix (30 µl), two wax valves in each reaction chamber (six in total), and a waste chamber for collecting the rest of the saliva sample. (c) One unit of the dispensing and reaction chamber. Illustration of (d) trapping and (e) dispensing processes. (f) One example of sample trapping and dispensing processes (Supplementary Video S2). The blue liquid is the saliva with the blue dye. The orange liquid is the RT-LAMP master mix with orange dye for better visualization.

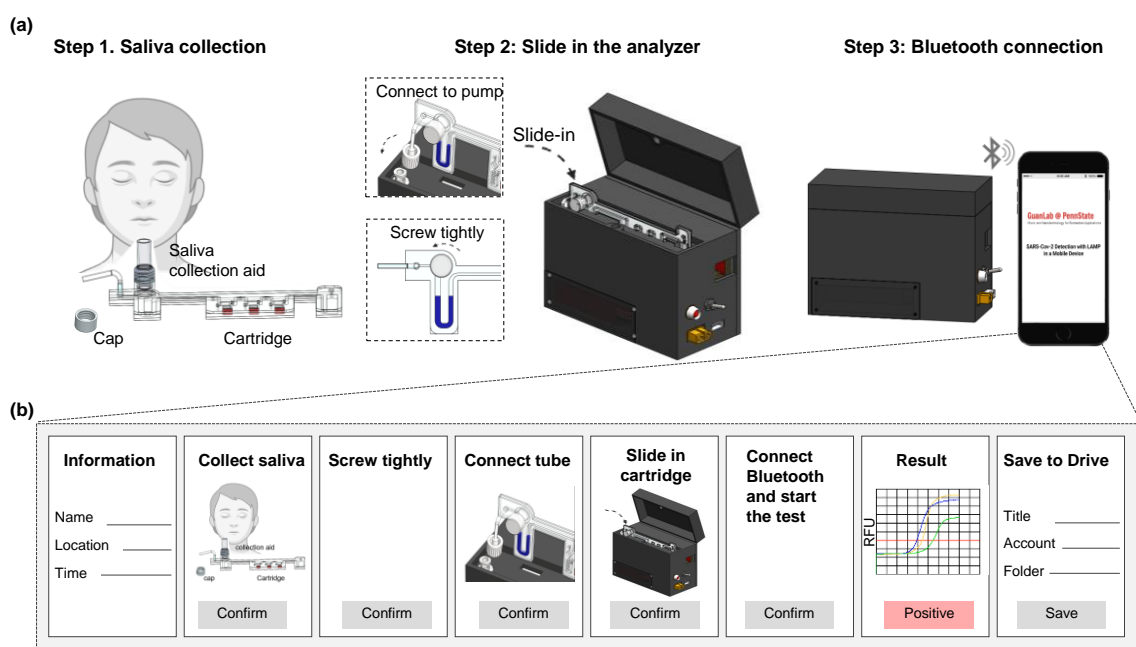
which helps to balance the hydraulic resistance among three units. To avoid liquid overflowing, we intentionally designed a long S-shaped releasing channel with a venting hole at the end. In addition, a thin layer of wax on top of the RT-LAMP mix functions as an evaporation barrier. **Figure 5-6f** and **Video 1** showed a representative example of automated saliva processing on the cartridge.

### 5.3.3. Saliva Test Workflow

The overall SLIDE workflow from the saliva sample to the molecular results is shown in **Figure 5-7a**. Four components are needed for a test: a disposable cartridge, a saliva collection aid (SCA), a portable analyzer, and an Android smartphone. With the help of the instructions on an interactive smartphone app (**Figure 5-7b**), one would self-collect saliva samples into a cartridge with the help of an SCA. While collecting the whole saliva through spitting or drooling is feasible, the saliva collection aid could increase participant compliance and avoid sample foaming [154]. After sufficient saliva (~120  $\mu$ l) was collected into the cartridge, the user should seal the cartridge with a screw cap. The sealed cartridge can then be connected to the piezo pump through a luer-lock interface and be inserted into the analyzer. One then would need to turn on the analyzer for the smartphone to recognize and communicate through the Bluetooth connection. This process takes less than 2 min hands-on time and is the only manual testing step.

Once the SLIDE analyzer receives the ‘start testing’ command from the smartphone app, the analyzer will automatically perform the required tasks on the cartridge. It includes saliva thermal lysis, sample metering and dispensing, RT-LAMP reaction and real-time detection, and data analysis and storage. Specifically, the analyzer begins the test by thermal lysis of the saliva sample at 95°C for 5 minutes. This step inactivates RNases and releases the virus from the saliva sample [154]. The resulting lysates were automatically transferred and dispensed into the reaction chamber with a preloaded RT-LAMP master. The whole sample preparation takes about 13 minutes. After

dispensing the sample, the real-time RT-LAMP reaction starts at a constant temperature of  $\sim 64$  °C. The acquired fluorescence data are transmitted to the smartphone app every 5 seconds. The threshold to distinguish the positive from the negative was set at 50 RFU based on the NTC samples tested (**Figure 5-3**). We classify a sample as positive only when two out of three reactions have a higher RFU than the threshold value in 30 minutes. The test results could be saved on the local device and uploaded to a cloud. The whole process is fully automated (**Figure 5-8**) and takes about 45 min from the saliva collection to the result, with very minimal user intervention (**Video S2**).



**Figure 5-7.** Overall SLIDE workflow. (a) Step 1: the patient self-collect  $\sim 120$   $\mu\text{L}$  of saliva into a cartridge using saliva collection aid. The users tighten the screw cap and connect the lure luck to the micro pump. Step 2: Insert the cartridge into the analyzer. Step 3: Connect the SLIDE analyzer with a smartphone through Bluetooth to initiate the test. (b) Step by step instruction of APP interface, including personal information collection, sample collection guidance, Bluetooth connection, test initiation, receiving and plotting real-time amplification data on the phone screen, and upload all data to the cloud.

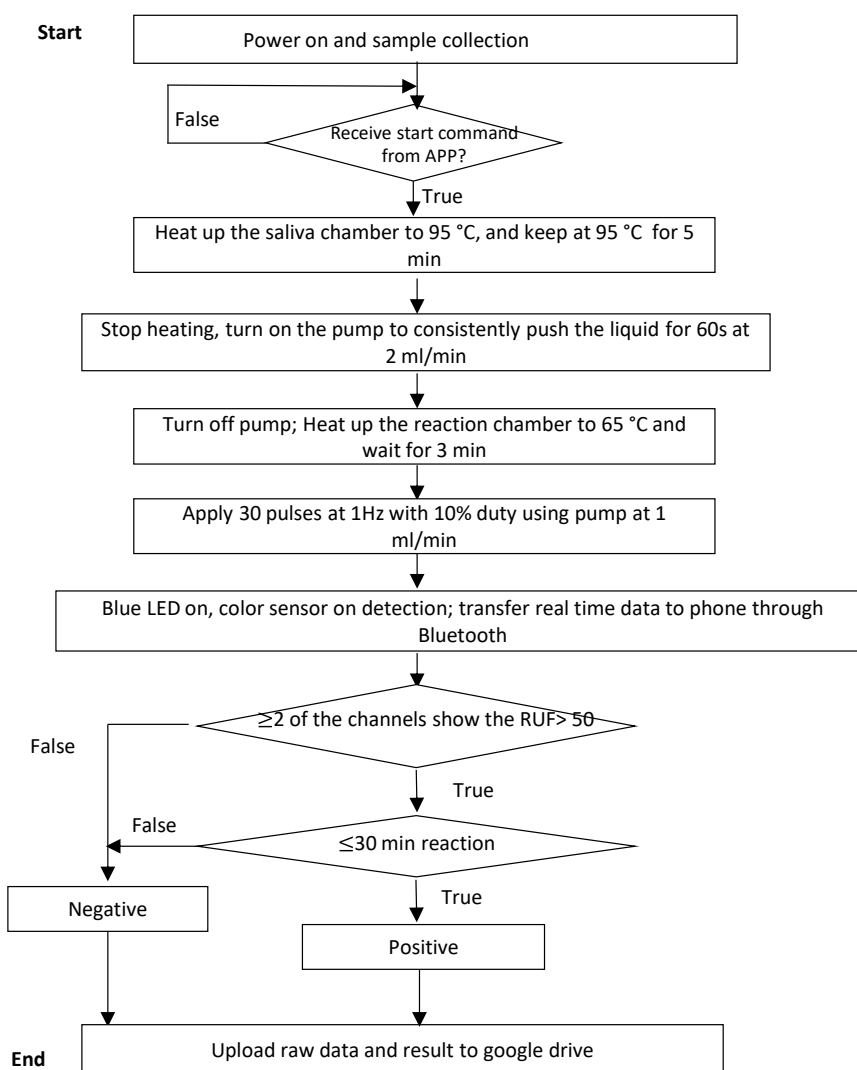


#### 5.3.4. Evaluation with mock sample and clinical sample

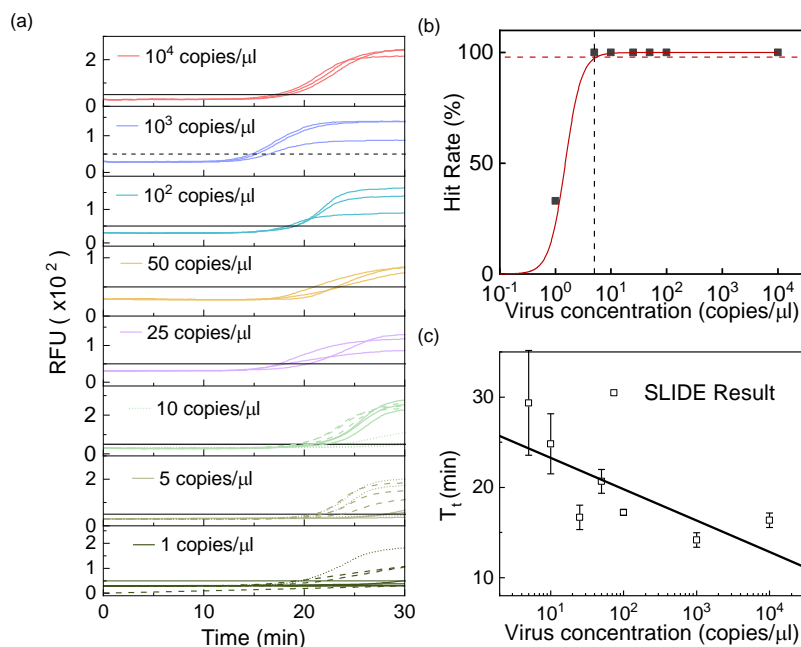
After validating all the subsystems and system integration, we set out to test the performance of the SLIDE. Here, we used our previously validated SARS-CoV-2 RT-LAMP primer set [162] (Table 3-2) against the highly conserved N region with a modified fluorescent concentration of SYTO9 (Table 5-1). We formed mock SARS-CoV-2 positive samples by spiking the healthy saliva with different concentrations of heat-inactivated SARS-CoV-2 virus particles. The final viral concentration of the mock sample ranges from 1 to  $10^4$  copies/ $\mu$ l. We run one test (three reactions each) at the concentration above 25 copies/ $\mu$ l and three tests (nine reactions) at the concentration below 10 copies/ $\mu$ l. **Figure 5-9a** shows the real-time result. Based on the voting decision-making system, more than two amplified assay is identified as positive, otherwise is determined as negative. Therefore, all samples are positive with the concentration above 5 copies/ $\mu$ l. While with the 1 copy/ $\mu$ l sample, only one test was identified as positive, the rest of the two are negative.

**Figure 5-10** shows the detailed plot of each test at a concentration lower than 10 copies/ $\mu$ l. To estimate the LoD of the test, we examine the hit rates at different virus concentrations [87]. The hit rate is defined as the positive test over all the tests under the same concentration. As shown in **Figure 5-9b**, the hit rate started to roll off from 1 to 0.3 when the concentration decreased from 5 copies/ $\mu$ l to 1 copy/ $\mu$ l. We fitted the experimental hit rate data with a logistic curve. The LoD is determined to be about 5 copies/reaction at the 98% confidence level. This LoD is comparable with the LoD (6/ $\mu$ L) using FDA-proved qRT-PCR assays with the same heat-lysis saliva sample preparation method[154]. **Figure 5-9c** shows the threshold time in the SLIDE analyzer with different virus concentrations. As expected, the threshold time and the standard deviation among the times to positive increases as the virus particle concentration decreases. To further evaluate our device, the same spike samples were tested using the benchtop PCR machine. We manually performed the sample thermal lysis in the heating block for 5 min at 95°C, then transferred 10  $\mu$ l

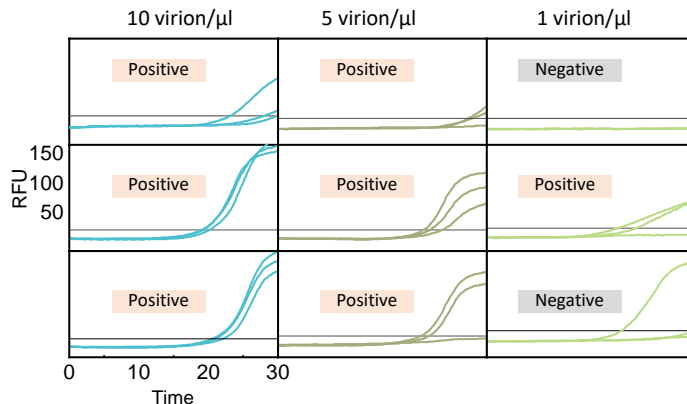
of the processed sample using a pipette to the PCR tube with a preloaded RT-LAMP master mix. After mixing the reagents thoroughly, the reactions were performed using a benchtop PCR machine **Figure 5-11**. **Figure 5-11d** show a Pearson correlation of the threshold time between the SLIDE analyzer and the PCR instrument. A coefficient ( $R=0.835$ ) indicates a strong positive correlation between automatic and manual methods. The threshold values for all the concentrations are shown in **Table 5-2** and **Table 5-3**.



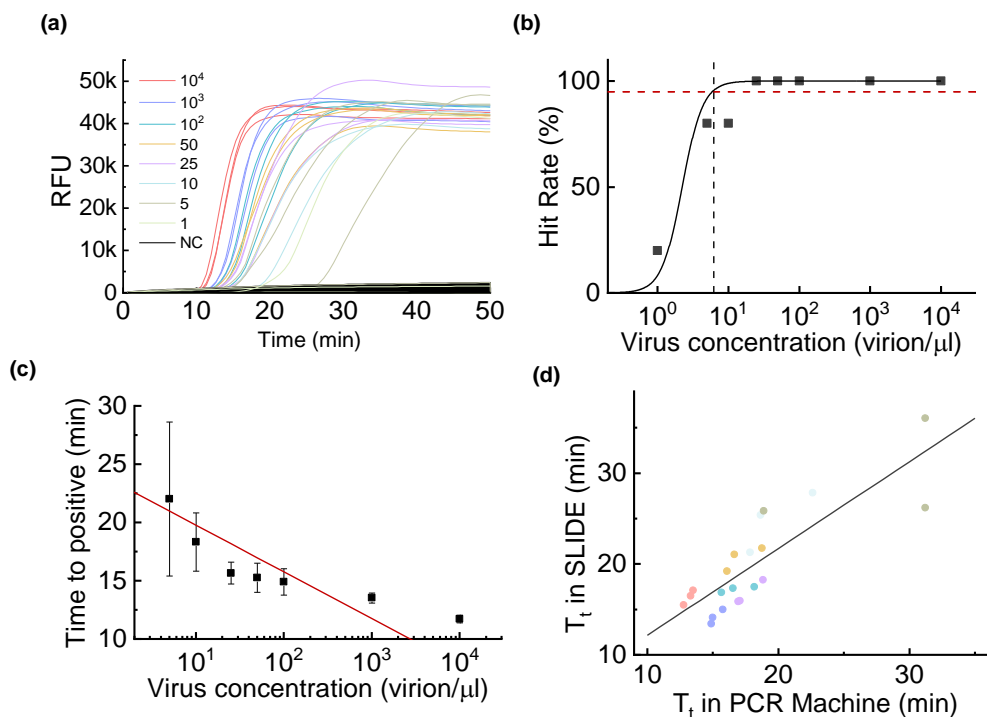
**Figure 5-8.** The Flow chart of the automatic workflow from sample collection, sample preparation, sample dispensing, RT-LAMP reaction, and result storage.



**Figure 5-9.** SLIDE device performance evaluation. (a) Real-time RT-LAMP results with different concentrations of the spiked saliva samples (1 virion/ $\mu\text{l}$  to 104 virion/ $\mu\text{l}$ ) using a SLIDE analyzer. The threshold to classify an amplification curve as positive or negative was 50 RFU based on the NTC sample (Supplementary Figure S5). (b) The extracted hit rate at various virus particle concentrations to establish LoD. (c) The inversely proportional relationship between the threshold time ( $T_t$ ) and virus particle concentration was obtained from the SLIDE analyzer. (d) The Pearson correlation analysis of the threshold time ( $T_t$ ) between the manual operation with PCR machine and automatic method using SLIDE analyzer. (e) Two clinical samples, one known positive(top) and one known negative(bottom), were tested by the SLIDE device. The RT-PCR assay performed the initial diagnosis as the reference. The experiment follows the process flow schematic shown in Figure 5-7.



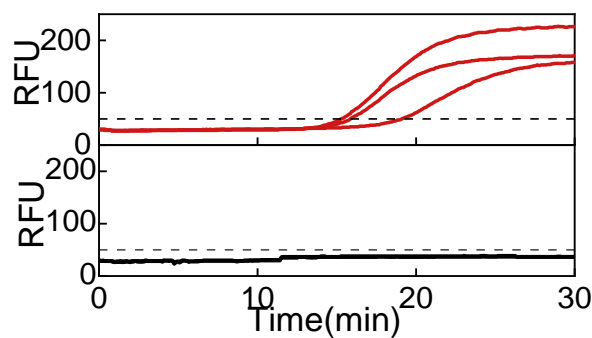
**Figure 5-10.** The real-time amplification result for the mock samples at low concentrations from 1 to 10 virion/ $\mu\text{l}$  using the SLIDE analyzer. The final results were labeled on the figure based on our voting system



**Figure 5-11.** Real-time RT-LAMP results with different concentrations of the Spiked saliva samples (1 copies/ $\mu\text{l}$  to 104 copies/ $\mu\text{l}$ ) using a PCR machine. The Spiked saliva samples were manually prepared in the heating block for 5 min at 95°C. 10  $\mu\text{l}$  of the sample was taken by pipette and transferred into the 30  $\mu\text{l}$  of the RT-LAMP master mix (b) The extracted hit rate at various virus particle concentrations to establish LoD. (c) The inversely proportional relationship between the time to positive and virus particle concentration.

To best evaluate the performance of SLIDE, clinical samples are tested. Here, two clinical samples (one known positive and one known negative) were obtained through an approved institutional review board (IRB) of the Pennsylvania State University (study number STUDY00016633). All the samples were coded to remove information associated with patient identifiers. The RT-PCR assay (DiaSorin Molecular, Cypress, CA, USA) performed the initial diagnosis as the reference method to benchmark our SLIDE. The experiment follows the process flow schematic shown in **Figure 5-8** and **Supplementary Video S2**. The amplification curves (raw data) are shown in

**Figure 5-12.** In 30 minutes of the amplification process, all of the reactions in the positive test showed sharp RFU increases and stabilized at the RFU value at least three times above the threshold. Three out of three reactions in the bottom negative clinical sample showed no obvious RFU changes and stabilized at the RFU value less than the threshold value (RFU 50). Based on the voting system for result making, the positive and negative samples determined by the SLIDE analyzer were the same as the pre-identified positive and negative samples by RT-PCR.



**Figure 5-12.** Two clinical samples, one known positive(top) and one known negative(bottom), were tested by the SLIDE device. The RT-PCR assay performed the initial diagnosis as the reference. The experiment follows the process flow schematic shown in Figure 5-8 and Supplementary Video S1.

**Table 5-2.** Time to positive with mock sample using manual operation

Concentration	Sample 1 (min)	Sample 2 (min)	Sample 3 (min)	Average (min)
10 <sup>4</sup> virion/μl	12.7	13.3	13.4	13.1
10 <sup>3</sup> virion/μl	14.8	15.7	15.0	15.2
100 virion/μl	16.5	15.6	18.1	16.7
50 virion/μl	16.6	16.1	18.7	17.1
25 virion/μl	16.9	17.1	18.8	17.6
10 virion/μl	17.8	18.6	22.6	19.7
5 virion/μl	18.8	31.2	31.2	27.1
1 virion/μl	NA	NA	NA	NA

**Table 5-3.** Time to positive with different concentration of mock sample using SLIDE

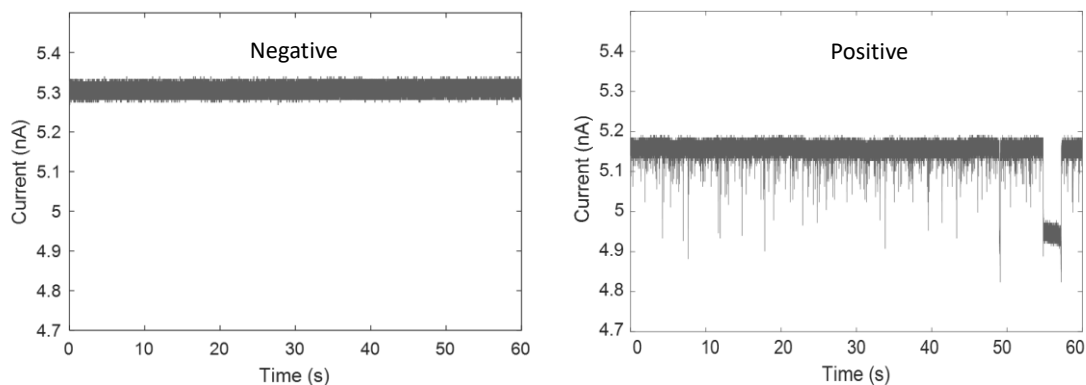
Concentration	Sample 1 (min)	Sample 2 (min)	Sample 3 (min)	Average (min)
10 <sup>4</sup> virion/μl	15.5	16.5	17.1	16.4
10 <sup>3</sup> virion/μl	13.4	14.1	15.0	14.2
100 virion/μl	16.87	17.3	17.5	17.2
50 virion/μl	19.2	21.0	21.7	20.6
25 virion/μl	16.0	18.23	21.26	18.5

Concentration	S1	S2	S3	S4	S5	S6	S7	S8	S9
10 virion/μl	21.3	25.4	27.8	18.8	18.8	20.4	20.9	21.2	22.3
5 virion/μl	25.8	26.1	36.1	21.1	21.9	23.96	21.03	22.6	NA
1virion/μl	NA	NA	NA	19.1	21.8	NA	NA	NA	20.0

### 5.3.5. Nanopore analyze of the final amplicons

We set out to test if the nanopore could detect the end-product of the RT-LAMP reaction from the saliva sample. First, we tested the negative control (NC) sample. These samples only contain healthy people saliva and RT-LAMP master mix and reaction for 30 minutes. As shown in **Figure 5-13a**, no events were observed for 60 s of recording. This confirmed the RT-LAMP reagents and the heat inactivated saliva sample were not detectable by the nanopore. After confirming the negative master mix did not produce measurable events, we continued to test the positive sample with mock SARS-CoV-2 positive sample. As shown in **Figure 5-13b**, after 30 min of RT-LAMP reaction of this positive control sample, clear events were immediately observable in the 60s measurement, with the event rate of 12/s. These results confirmed that the saliva background has negligible impact on event rate determination since SARS-CoV-2 RNA specific amplicons dominated the RT-LAMP product.



**Figure 5-13.** Validation of nanopore counting of the end-product of the RT-LAMP reaction from the saliva sample. (a) negative control (NTC), and (b) positive control after the 30 min

### 5.3.6. Performance comparison

We compare our SLIDE analyzer with eight top-rated NAT device for SARS-CoV-2 detection, shown in the below table. In general, RT-PCR based detections are more sensitive and specific than the RT-isothermal based platform, but taking more recourse (e.g., time, power etc.) to perform. Among those RT-isothermal based platforms, CUE Health can be used for self-testing and show comparable accuracy with other two methods, but this method has no sample preparation step and the LoD (60000 cp/ml) is 12 times and 20 times higher than that of SLIDE (5000 cp/ml) and ID NOW. ID NOW and SLIDE both implement the sample preparation method with the RT-isothermal method, but prepare sample and transfer liquids in different methods. In ID NOW platform, the swab sample will be first inserted into the pre-heated lysis buffer and transfer the high temperature processed sample to the amplification assay. This process must be performed by a clinician in healthcare provider. In contrast, SLIDE analyzer implements the heat-inactivated method for the sample preparation which require so addition lysis buffer. Moreover, SLIDE analyzer can automatically handle all the steps including sample preparation, dispensing, amplification, detection on the signal cartridge with zero interference. Last but not least, SLIDE is

the only one using saliva as the sample type, which is easy, noninvasive and can largely increase the accessibility of self-testing. We admit that SLIDE analyzer takes longer time than the other two platform, which is because 13 minutes were spent on the sample preparation step. In the future, we will further minimize the sample preparation step by, for example, improving the thermal coupling and minimizing the heating dissipation.

**Table 5-4.** Performance comparison between SLIDE analyzer with commercially available NAT devices

<b>Analyzer</b>	<b>Sensitivity (Ci 95%)</b>	<b>Specificity (Ci 95%)</b>	<b>Limit Of Detection</b>	<b>Type Of NAAT</b>	<b>Sample Type</b>	<b>Time (Min)</b>
<b>CEPHEID XPE RT[163-166]</b>	99% (97%-99%)	97% (95%-98%)	250 copies/ml	RT-PCR	Nasopharyngeal, throat, nasal swab	46
<b>VISIBY MEDICAL [167, 168]</b>	95% (86%-99%)	100% (81%-100%)	1112copies/ ml	RT-PCR	Nasal swab	45
<b>BIOMEME FRANKLIN™ THREE 9[169, 170]</b>	99% (97%-100%)	97% (95%-100%)	4200 copies/ml	RT-PCR	Nasal swab	80
<b>ACCUA SARS-COV-2 TEST[171]</b>	68.0% (53-81%)	100% (94%-100%)	150 copies/ml	RT-PCR	Nasal swab	30
<b>BIOFIRE[165, 172]</b>	93% (85%-97%)	100% (90%-100%)	330 copies/ml	RT-PCR	Nasopharyngeal swab	45
<b>EPLEX[166]</b>	91.4% (81%-97%)	100% (93%-100%)	316 copies/ml	RT-PCR	Nasopharyngeal and nasal swab	90
<b>ABBOTT ID NOW [163- 166, 173]</b>	79% (69%-86%)	100% (98%-100%)	3225 copies/ml	RT- isothermal	Nasopharyngeal and nasal swab	<15
<b>CUE HEALTH [174, 175]</b>	92%	98%	60000 copies/ml	RT- isothermal	Nasal swab	20
<b>SLIDE</b>	97% (97%-99%)	92% (95%-98%)	5000 copies/ml	RT- isothermal	Saliva	30-45



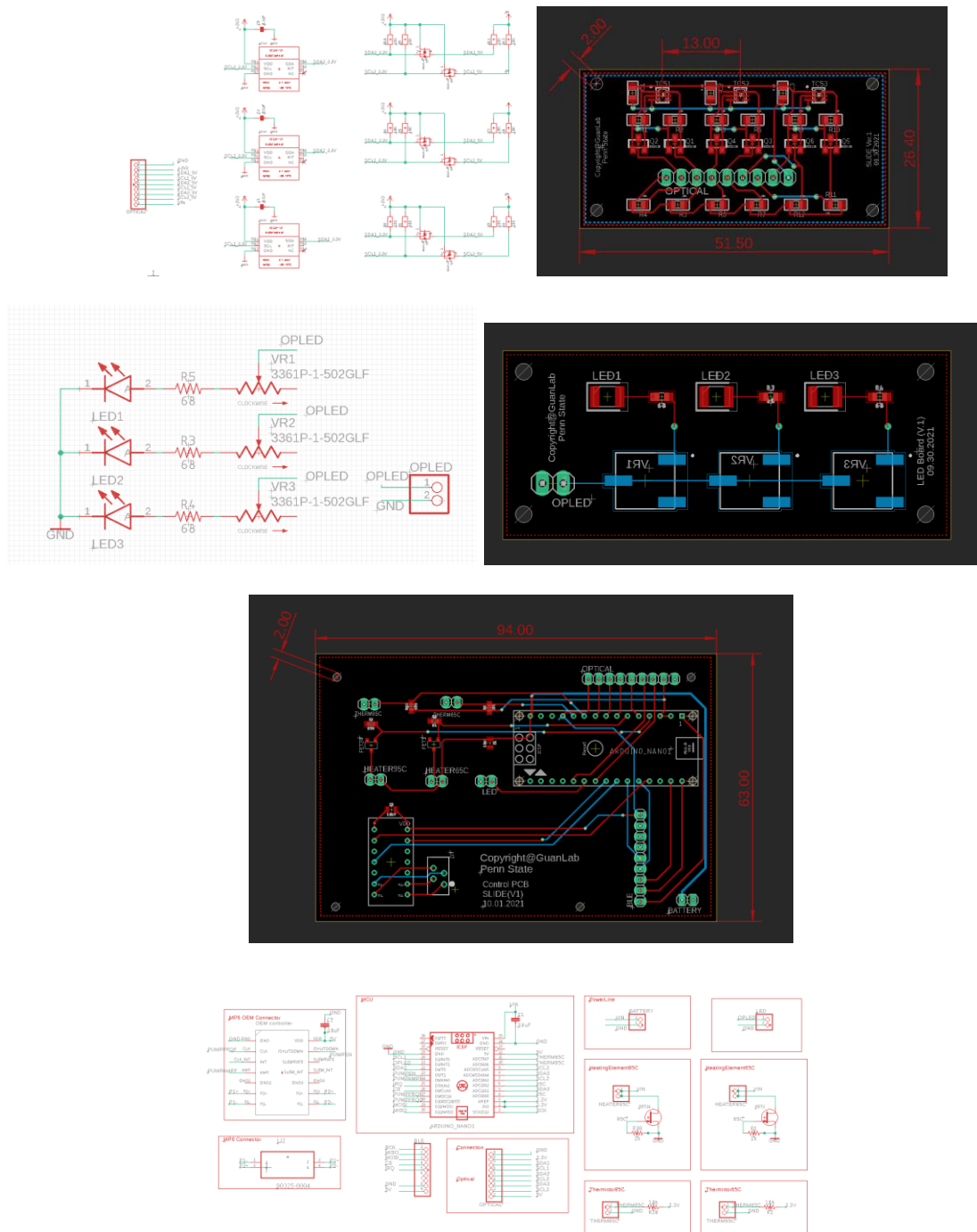
## 5.4. Summary

In this paper, we demonstrate a fully integrated system for rapid (<45 min) self-testing for the SARS-CoV-2 virus from saliva samples. This fully portable approach can detect the virus rapidly without needing an RNA extraction kit and pipetting steps. All other complexities are handled automatically by the SLIDE analyzer, including heat-inactivated sample preparation, the pressure-driven sample dispensing and mixing, real-time RT-LAMP reaction and detection, and data processing, storage and upload. Our automatic system shows a great quantitative agreement with the manual process using a benchtop PCR machine (outside the cartridge). The analytical sensitivity (Limit of detection) against SARS-CoV-2 virus particle spiked saliva sample is 5 virion/ $\mu$ l. With these two clinical saliva samples, our device shows 100% agreement with the RT-PCR method. The final amplicons from the developed prototype were also detected by nanopore counting methods. The promising results of the present study could likely be extended for use with saliva samples for noninvasive, portable, rapid, and scalable self-testing for COVID-19. Considering the limited reagent lifetime at room temperature, we will address the challenge of storing and transporting the liquid phase on the microfluidic reagent with reagent lyophilization in the future study.

## 5.5. Appendix

**Table 5-5.** Bill of materials for analyzer

System	Vendor	Description	Part#	Function	Unit (\$)	Unit	Ext (\$)
Electronics	Adafruit	Arduino Nano	A000005	Microcontroller	20.07	1	20.07
Electronics	Newark	Through Hole Resistor, 10 k $\Omega$	38K0328	Temperature control	0.09	1	0.09
Electronics	Newark	Through Hole Resistor, 47 $\Omega$	38K0326	Resistors for LED	0.09	4	0.36
Electronics	Newark	Capacitor 470uF	65R3137	Power Stabilizing	0.11	1	0.11
Electronics	Newark	Capacitor 0.33uF	46P6304	Voltage regulating	0.27	1	0.27
Electronics	Newark	Capacitor 0.1uF	46P6667	Voltage regulating	0.354	1	0.354
Electronics	DigiKey	8 Position Header Connector	S7041-ND	PCB connector	0.3	5	1.5
Electronics	Adafruit	Jumper Wire	1568-1512-ND	Wiring	1.95	1	1.95
Electronics	DigiKey	Tactile switch	1825910-6	Push-button	0.09	1	0.09
Electronics	Adafruit	Bluetooth Low Energy (BLE)	2633	Bluetooth module	14	1	14
Electronics	ZIPPY	1300mAh 2S 25C Lipo Pack	ZC.1300.2S.25	Battery	7.95	1	7.95
Pumping	Servoflo	Piezo-pump	mp6-hyb	Drive reagents	22.31	1	22.31
Pumping	Servoflo	Driver circuit	mp6-oem	Power the piezo-pump	42	1	42
PCB fabrication	OSH Park	Control PCB	NA		30	1	30
PCB fabrication	OSH Park	LED PCB	NA		6.2	1	6.2
PCB fabrication	OSH Park	Optical sensor PCB	NA		7	1	7
Thermal	Newark	N Channel Power MOSFET	63J7707	Switch for resistive heater	1.66	1	1.66
Thermal	Newark	Thermistor	95C0606	Temperature sensing	4.48	2	8.96
Thermal	DigiKey	Power resistor	MP725-5.00	Heating the alumin block	3.22	5	16.1
Thermal	Mc master	Aluminum	9246K523	Heating block	12.3	1	12.3
Optics	Adafruit	Color Sensor	TCS34725	Detection	2.6	3	7.8
Optics	Newark	LED, Blue, T-1 3/4 (5mm)	04R6674	Fluorescence excitation	0.21	1	0.21
Enclosure	Inhouse	3D printed platform	NA	NA	40	1	40
<b>Total Cost</b>							<b>241.284</b>



**Figure 5-14.** PCB design for all the sub modules: color sensor module, LED module control PCB module.

## Chapter 6 Conclusions and Future Perspectives

### 6.1. Conclusions

This dissertation explores the possibility of developing a fully integrated NAAT system using solid-state nanopores for rapid, label-free nucleic acid self-testing. Three major parts has been explored in the realm of this thesis.

Amplification strategies can exponentially increase the target molecules and the results are often read out using optical methods by introducing florescence to the system. In our work, we first proposed and demonstrated the RT-LAMP-coupled nanopore counting method for label free nucleic acid testing. This approach lends itself to most amplification strategies as long as the target template is specifically replicated in numbers. Due to its intrinsic single molecule sensitivity, it is found that the nanopore sensor could make a faster positive/negative call than bulk optical methods. We examined the ability of the nanopore to capture the LAMP reaction dynamics. We found that LAMP-coupled glass nanopore counting has the potential to be used in a qualitative as well as quantitative test. The highly sensitive and specific sensing strategy would open a new avenue for solid-state nanopore sensors towards a new form of compact, rapid, low-cost nucleic acid testing at the point of care.

To further explore a more reliable and integratable method for nanopore fabrication, we developed the optical system for single nanopore fabrication and characterization. We developed and validated a physical model to project the confidence level for single nanopore fabrication using laser-assisted breakdown method. Both the model and our experimental data suggest that a combination of a high laser power and a low electric field is statistically favorable for forming a single nanopore at a programmed location. Addressing the reliability and fidelity issue in the controlled dielectric

breakdown method is critical for the scalable SiNx nanopore fabrication, which is essential for developing integrated point of care devices.

The integrated molecular diagnostics device typically has four essential steps: (1) cells or virus particles lysis and DNA or RNA extraction, (2) sample partition by pipetting or microfluidic device, (3) target sequence amplification, (4) real-time detection mechanism. We developed a fully integrated sample-in-answer-out nucleic acid testing system for SARS-CoV-2 detection. The unprecedentedly integrated system facilitates streamlined virus lysis and inactivation, sample dispensing and real-time detection on a single reagent compact cartridge. The prototype system was first validated using optical sensor. With a turnaround time of ~45 minutes, we achieved a limit of detection (LoD) of 5 virion/ $\mu$ l of a saliva sample. This LoD is comparable with the LoD(6–12 copies/ $\mu$ L) using FDA-proved qRT-PCR assays with the same heat-inactivated saliva sample preparation method [154]. The performance of the developed prototype was also evaluated with the using nanopore counting method. Therefore, the success demonstration of this nanopore measurement pave the way for ultracompact, rapid, and affordable nanopore-based nucleic acid testing.

In summary, the significant contributions of this thesis are as follows:

- (1) We provided a novel LAMP-coupled nanopore counting method for label free nucleic acid testing. We found that LAMP-coupled glass nanopore counting has the potential to be used in a qualitative as well as quantitative test.
- (2) Using SARS-CoV-2 as an example, we systematical studied the performance of LAMP-coupled nanopore counting. Our method shows the about 65 cp/ $\mu$ l limit of detection and 100% analytical specificity. With 127 clinical samples and RT-PCR as the gold standard, our nanopore platform was able to detect SARS-CoV-2 with 98% diagnostic sensitivity, and 92%

diagnostic specificity.

(3) We developed the laser-assisted dielectric breakdown method for Single Nanopore Fabrication.

Both the model and our experimental data suggest that a combination of a high laser power and a low electric field is statistically favorable for forming a single nanopore at a programmed location.

(4) We provided an unprecedentedly integrated sample-to-answer nucleic acid testing device for highly sensitive detection of SARS-CoV-2 self-testing.

## **6.2. Future prospective**

The research work presented in the thesis has showed very promising results. However, several important aspects should be addressed in future researches.

Due to the negatively charged DNA is electrophoretically driven through the nanopore, the nanopore surface charge of nanopore can affect the translocation process under low salt concentration [82]. To efficiently count of the amplicons, we performed experiment with end point product and salt concentration of the assay was adjusted from 100 mM to 1 M KCl. In our next work, we considered monitoring the real-time RT-LAMP amplification process under 100 mM salt concentration. One of the possible solution would be neutralization the surface charge of the nanopore sensor [176]. Monitoring the amplicon population change at low salt concentration will be the essential step for a fully integrated the nanopore based POCT analyzer development.

The current laser-assisted breakdown method can localize the single nanopore at the desired location and decrease the noise by minimizing the exposed area under the electric field. So far, only one nanopore can be fabrication in each experiment. In the future, to increase the fabrication efficiency, we could design and fabricate a chamber array to assemble hundreds of SiN<sub>x</sub> membranes

on the sample on the sample chip. By automatically moving the 3D nano positioner, we can fabricate hundreds of nanopores sequentially. Besides, the pore size estimation can be further improved. In this paper, the pore size estimation is by using the well-accepted model,  $G = \sigma \left( \frac{4h}{\pi d^2} + \frac{1}{d} \right)^{-1}$  where  $\sigma$ ,  $h$ , and  $d$  represent the electrolyte conductivity, effective membrane thickness, and pore diameter, respectively. The effective membrane thickness of the pore area was estimated based on the etching rate multiply fabrication time. This etching rate was measured by AFM calibration result, which may vary from the experiment due to the SiNx membrane quality. Therefore, in the future, we could incorporate the Photoluminescence (PL) method to real-time monitoring the remaining thickness of the membrane[177].

We have demonstrated single pathogen (Malaria or SARS-CoV-2) can be rapid, effective detected by our RT-LAMP coupled nanopore platform. In this scheme, only one dimension data (event rate) from the nanopore sensing result was analyzed for making decision. This is sufficient for single pathogen detection. In the future, we intend to couple the nanopore platform with other type of amplification (e.g. recombinase polymerase amplification (RPA) [178] ) which generate its own signature amplicons with well-defined length. By combining these two-dimension information (event rate and molecule size), it has the potential to achieve the multiplexing platform. To be able to distinguish the different amplicons, more effort should be made on increasing the sensitivity and resolution of the solid state nanopore sensor. One possible direction could be decreasing the nanopore size and membrane thickness [31].

In the current system, we only incorporated the optical system to monitor the amplification process for demonstration. In our next step, we will need to integrate a nanopore sensor, electrodes and amplifier into the system. Three potential challenges must be overcome: 1) The nanopore sensor assembly and sealing. Our current method is manually assembling SiNx chip on the cartridge using

Ecoflex. It is acceptable for few chips but will be too tedious and less realizable for hundreds and thousands chip assembly. Also, Sealing is the key of nanopore sensing measurement to ensure the 100 pA-10 nA current measurement. It is necessary to develop a proper way to examine the sealing before the measurement. 2) The electrode interfaces. Most of the experiment performed in the lab directly immerse the electrode into the measurement chamber and changing/cleaning electrodes for the next measurement to avoid contamination. When it comes to the integrated system, keeping changing/ cleaning the electrode will not be a practical practice. Therefore, developing an indirect method for measurement is essential. For example, instead of immersing the electrode directly into the chamber, we could coat conductive materials on the disposable cartridge to interface with the integrated electrode to facilitate the measurement and avoid contamination. 3) The high gain ( $10^7$ ) and high bandwidth (10kHz), low noise (less than 10 pA RMS @ 10 kHz) amplifier development and integration. Some commercially available portable amplifiers, for example, Elements nanopore reader, can be used in our system. But, for further multiplexing measurement, we can also collaborate with Integrated Circuits and Systems Laboratory to customize the nanopore reader.

The platform was mainly focus on thermal lysis sample preparation method. This is sufficient for clean sample and the sample with high viral load. For some sample with low virus load (e.g., HIV), an extra sample pre-concentration step is critical to improve the limit of detection. Other researchers of our group are parallely working the column-based or magnetic-based sample preparation step to improve the sample preparation step and increase the limit of detection.

The manual filling of liquid RT-LAMP assay in the cartridge is not optimal and still in prototyping stages. Future work is also suggested to investigate the better assay handling and storage. One possible solution is incorporating with the lyophilization technology.



Overall, amplification-coupled solid-state nanopore diagnostic technology has a promising future. It provides an unprecedented possibility of a new generation of label free, highly specific, sensitive, and reliable nucleic acid testing.

## Bibliography

- [1] R. G. Kerry *et al.*, "A comprehensive review on the applications of nano-biosensor-based approaches for non-communicable and communicable disease detection," *Biomaterials Science*, vol. 9, no. 10, pp. 3576-3602, 2021.
- [2] H. Harapan *et al.*, "Coronavirus disease 2019 (COVID-19): A literature review," *Journal of infection and public health*, 2020.
- [3] S. G. Deeks, J. Overbaugh, A. Phillips, and S. Buchbinder, "HIV infection," *Nature reviews Disease primers*, vol. 1, no. 1, pp. 1-22, 2015.
- [4] P. Sands, C. Mundaca-Shah, and V. J. Dzau, "The neglected dimension of global security—a framework for countering infectious-disease crises," *New England Journal of Medicine*, vol. 374, no. 13, pp. 1281-1287, 2016.
- [5] A. Hematian *et al.*, "Traditional and modern cell culture in virus diagnosis," *Osong public health and research perspectives*, vol. 7, no. 2, pp. 77-82, 2016.
- [6] R. M. Lequin, "Enzyme immunoassay (EIA)/enzyme-linked immunosorbent assay (ELISA)," *Clinical chemistry*, vol. 51, no. 12, pp. 2415-2418, 2005.
- [7] G. A. Posthuma-Trumpie, J. Korf, and A. van Amerongen, "Lateral flow (immuno) assay: its strengths, weaknesses, opportunities and threats. A literature survey," *Analytical and bioanalytical chemistry*, vol. 393, no. 2, pp. 569-582, 2009.
- [8] I. M. Mackay, K. E. Arden, and A. Nitsche, "Real-time PCR in virology," *Nucleic acids research*, vol. 30, no. 6, pp. 1292-1305, 2002.
- [9] S. Aydin, "A short history, principles, and types of ELISA, and our laboratory experience with peptide/protein analyses using ELISA," *Peptides*, vol. 72, pp. 4-15, 2015.
- [10] J. Gordon and G. Michel, "Analytical sensitivity limits for lateral flow immunoassays," *Clinical chemistry*, vol. 54, no. 7, pp. 1250-1251, 2008.
- [11] P. K. Drain *et al.*, "Diagnostic point-of-care tests in resource-limited settings," *The Lancet infectious diseases*, vol. 14, no. 3, pp. 239-249, 2014.
- [12] N. Zhu *et al.*, "A novel coronavirus from patients with pneumonia in China, 2019," *New England journal of medicine*, vol. 382, pp. 727-733, 2020.
- [13] Y. Mori, M. Kitao, N. Tomita, and T. Notomi, "Real-time turbidimetry of LAMP reaction for quantifying template DNA," *Journal of biochemical and biophysical methods*, vol. 59, no. 2, pp. 145-157, 2004.
- [14] S. Roy, S. X. Wei, J. L. Z. Ying, M. Safavieh, and M. U. Ahmed, "A novel, sensitive and label-free loop-mediated isothermal amplification detection method for nucleic acids using luminophore dyes," *Biosensors and Bioelectronics*, vol. 86, pp. 346-352, 2016.
- [15] A. Ganguli *et al.*, "Rapid isothermal amplification and portable detection system for SARS-CoV-2," *Proceedings of the National Academy of Sciences*, vol. 117, no. 37, pp. 22727-22735, 2020.
- [16] F. Sun *et al.*, "Smartphone-based multiplex 30-minute nucleic acid test of live virus from nasal swab extract," *Lab on a Chip*, vol. 20, no. 9, pp. 1621-1627, 2020.
- [17] S. Wei *et al.*, "Direct diagnostic testing of SARS-CoV-2 without the need for prior RNA extraction," *Scientific reports*, vol. 11, p. 2402., 2021.
- [18] L. Yu *et al.*, "Rapid detection of COVID-19 coronavirus using a reverse transcriptional loop-mediated isothermal amplification (RT-LAMP) diagnostic platform," *Clinical chemistry*, vol. 66, no. 7, pp. 975-977, 2020.

- [19] L. E. Lamb, S. N. Bartolone, E. Ward, and M. B. Chancellor, "Rapid detection of novel coronavirus (COVID19) by reverse transcription-loop-mediated isothermal amplification," Available at SSRN 3539654, vol. <http://dx.doi.org/10.2139/ssrn.3539654>, 2020.
- [20] V. L. D. Thi *et al.*, "A colorimetric RT-LAMP assay and LAMP-sequencing for detecting SARS-CoV-2 RNA in clinical samples," *Science translational medicine*, vol. 12, no. 556, p. eabc7075, 2020.
- [21] C. Yan *et al.*, "Rapid and visual detection of 2019 novel coronavirus (SARS-CoV-2) by a reverse transcription loop-mediated isothermal amplification assay," *Clinical Microbiology and Infection*, vol. 26, no. 6, pp. 773-779, 2020.
- [22] B. Ning *et al.*, "A smartphone-read ultrasensitive and quantitative saliva test for COVID-19," *Science advances*, vol. 7, no. 2, p. eabe3703, 2021.
- [23] T. Albrecht, "Single-molecule analysis with solid-state nanopores," *Annual Review of Analytical Chemistry*, vol. 12, pp. 371-387, 2019.
- [24] B. N. Miles, A. P. Ivanov, K. A. Wilson, F. Doğan, D. Japrun, and J. B. Edel, "Single molecule sensing with solid-state nanopores: novel materials, methods, and applications," *Chemical Society Reviews*, vol. 42, no. 1, pp. 15-28, 2013.
- [25] G. Choi, T. Prince, J. Miao, L. Cui, and W. Guan, "Sample-to-answer palm-sized nucleic acid testing device towards low-cost malaria mass screening," *Biosensors and Bioelectronics*, vol. 115, pp. 83-90, 2018.
- [26] C. Toumazou *et al.*, "Simultaneous DNA amplification and detection using a pH-sensing semiconductor system," *Nature methods*, vol. 10, no. 7, pp. 641-646, 2013.
- [27] Z. Tang, G. Choi, R. Nouri, and W. Guan, "Loop-mediated isothermal amplification-coupled glass nanopore counting toward sensitive and specific nucleic acid testing," *Nano letters*, vol. 19, no. 11, pp. 7927-7934, 2019.
- [28] B. N. Miles, A. P. Ivanov, K. A. Wilson, F. Dogan, D. Japrun, and J. B. Edel, "Single molecule sensing with solid-state nanopores: novel materials, methods, and applications," (in English), *Chemical Society Reviews*, vol. 42, no. 1, pp. 15-28, 2013.
- [29] T. Albrecht, "Single-Molecule Analysis with Solid-State Nanopores," *Annu Rev Anal Chem*, vol. 12, no. 1, pp. 371-387, Jun 12 2019.
- [30] J. L. Li, M. Gershow, D. Stein, E. Brandin, and J. A. Golovchenko, "DNA molecules and configurations in a solid-state nanopore microscope," (in English), *Nature Materials*, vol. 2, no. 9, pp. 611-615, Sep 2003.
- [31] H. Yamazaki, R. Hu, Q. Zhao, and M. Wanunu, "Photothermally assisted thinning of silicon nitride membranes for ultrathin asymmetric nanopores," *ACS nano*, vol. 12, no. 12, pp. 12472-12481, 2018.
- [32] K. A. Roshan, Z. Tang, and W. Guan, "High fidelity moving Z-score based controlled breakdown fabrication of solid-state nanopore," *Nanotechnology*, vol. 30, no. 9, p. 095502, Mar 1 2019.
- [33] L. J. Steinbock, R. D. Bulushev, S. Krishnan, C. Raillon, and A. Radenovic, "DNA translocation through low-noise glass nanopores," *Acs Nano*, vol. 7, no. 12, pp. 11255-11262, 2013.
- [34] N. A. Bell, M. Muthukumar, and U. F. Keyser, "Translocation frequency of double-stranded DNA through a solid-state nanopore," *Phys Rev E*, vol. 93, no. 2, p. 022401, Feb 2016.
- [35] N. Reza, Z. Tang, and W. Guan, "Calibration-Free Nanopore Digital Counting of Single Molecules," *Anal Chem*, vol. 91, no. 17, pp. 10915-11488, 2019.
- [36] S. Garaj, W. Hubbard, A. Reina, J. Kong, D. Branton, and J. A. Golovchenko, "Graphene as a subnanometre trans-electrode membrane," (in English), *Nature*, vol. 467, no. 7312, pp. 190-193, Sep 9 2010.

- [37] J. Li, D. Stein, C. McMullan, D. Branton, M. J. Aziz, and J. A. Golovchenko, "Ion-beam sculpting at nanometre length scales," *Nature*, vol. 412, no. 6843, pp. 166-169, 2001.
- [38] R. S. Wei, V. Gatterdam, R. Wieneke, R. Tampe, and U. Rant, "Stochastic sensing of proteins with receptor-modified solid-state nanopores," (in English), *Nature Nanotechnology*, vol. 7, no. 4, pp. 257-263, Apr 2012.
- [39] S. M. Iqbal, D. Akin, and R. Bashir, "Solid-state nanopore channels with DNA selectivity," *Nature nanotechnology*, vol. 2, no. 4, p. 243, 2007.
- [40] U. F. Keyser, "Enhancing nanopore sensing with DNA nanotechnology," (in English), *Nature Nanotechnology*, vol. 11, no. 2, pp. 106-108, Feb 2016.
- [41] J. Y. Y. Sze, A. P. Ivanov, A. E. G. Cass, and J. B. Edel, "Single molecule multiplexed nanopore protein screening in human serum using aptamer modified DNA carriers," *Nat Commun*, vol. 8, no. 1, p. 1552, Nov 16 2017.
- [42] N. A. W. Bell and U. F. Keyser, "Specific Protein Detection Using Designed DNA Carriers and Nanopores," (in English), *Journal of the American Chemical Society*, vol. 137, no. 5, pp. 2035-2041, Feb 11 2015.
- [43] J. L. Kong, J. B. Zhu, and U. F. Keyser, "Single molecule based SNP detection using designed DNA carriers and solid-state nanopores," (in English), *Chemical Communications*, vol. 53, no. 2, pp. 436-439, Jan 7 2017.
- [44] Y. F. Wu, R. D. Tilley, and J. J. Gooding, "Challenges and Solutions in Developing Ultrasensitive Biosensors," (in English), *Journal of the American Chemical Society*, vol. 141, no. 3, pp. 1162-1170, Jan 23 2019.
- [45] J. J. Gooding and K. Gaus, "Single-Molecule Sensors: Challenges and Opportunities for Quantitative Analysis," (in English), *Angewandte Chemie-International Edition*, vol. 55, no. 38, pp. 11354-11366, Sep 12 2016.
- [46] M. Wanunu, W. Morrison, Y. Rabin, A. Y. Grosberg, and A. Meller, "Electrostatic focusing of unlabelled DNA into nanoscale pores using a salt gradient," *Nat Nanotechnol*, vol. 5, no. 2, pp. 160-5, Feb 2010.
- [47] K. J. Freedman, L. M. Otto, A. P. Ivanov, A. Barik, S.-H. Oh, and J. B. Edel, "Nanopore sensing at ultra-low concentrations using single-molecule dielectrophoretic trapping," *Nature communications*, vol. 7, p. 10217, 2016.
- [48] T. Notomi *et al.*, "Loop-mediated isothermal amplification of DNA," *Nucleic Acids Res*, vol. 28, no. 12, p. E63, Jun 15 2000.
- [49] N. Tomita, Y. Mori, H. Kanda, and T. Notomi, "Loop-mediated isothermal amplification (LAMP) of gene sequences and simple visual detection of products," *Nature protocols*, vol. 3, no. 5, pp. 877-882, 2008.
- [50] Y. L. Ma, F. Y. Teng, and M. Libera, "Solid-Phase Nucleic Acid Sequence-Based Amplification and Length-Scale Effects during RNA Amplification," (in English), *Analytical Chemistry*, vol. 90, no. 11, pp. 6532-6539, Jun 5 2018.
- [51] H. Ahn, B. S. Batule, Y. Seok, and M. G. Kim, "Single-Step Recombinase Polymerase Amplification Assay Based on a Paper Chip for Simultaneous Detection of Multiple Foodborne Pathogens," *Anal Chem*, vol. 90, no. 17, pp. 10211-10216, Sep 4 2018.
- [52] S. D. Polley *et al.*, "Mitochondrial DNA targets increase sensitivity of malaria detection using loop-mediated isothermal amplification," *J Clin Microbiol*, vol. 48, no. 8, pp. 2866-71, Aug 2010.
- [53] S. Britton *et al.*, "Sensitive detection of *Plasmodium vivax* using a high-throughput, colourimetric loop mediated isothermal amplification (HtLAMP) platform: a potential novel tool for malaria elimination," *PLoS neglected tropical diseases*, vol. 10, no. 2, p. e0004443, 2016.

- [54] K. Venta *et al.*, "Differentiation of Short, Single-Stranded DNA Homopolymers in Solid-State Nanopores," (in English), *Acs Nano*, vol. 7, no. 5, pp. 4629-4636, May 2013.
- [55] Q. Jin, A. M. Fleming, R. P. Johnson, Y. Ding, C. J. Burrows, and H. S. White, "Base-Excision Repair Activity of Uracil-DNA Glycosylase Monitored Using the Latch Zone of alpha-Hemolysin," (in English), *Journal of the American Chemical Society*, vol. 135, no. 51, pp. 19347-19353, Dec 25 2013.
- [56] M. Wanunu, T. Dadosh, V. Ray, J. Jin, L. McReynolds, and M. Drndic, "Rapid electronic detection of probe-specific microRNAs using thin nanopore sensors," *Nat Nanotechnol*, vol. 5, no. 11, pp. 807-14, Nov 2010.
- [57] Y. Wang, D. Zheng, Q. Tan, M. X. Wang, and L.-Q. Gu, "Nanopore-based detection of circulating microRNAs in lung cancer patients," *Nature nanotechnology*, vol. 6, no. 10, p. 668, 2011.
- [58] A. Y. Grosberg and Y. Rabin, "DNA capture into a nanopore: interplay of diffusion and electrohydrodynamics," *The Journal of chemical physics*, vol. 133, no. 16, p. 10B617, 2010.
- [59] K. J. Freedman *et al.*, "Nonequilibrium capture rates induce protein accumulation and enhanced adsorption to solid-state nanopores," *ACS nano*, vol. 8, no. 12, pp. 12238-12249, 2014.
- [60] A. Meller and D. Branton, "Single molecule measurements of DNA transport through a nanopore," *Electrophoresis*, vol. 23, no. 16, pp. 2583-2591, 2002.
- [61] G. Choi, D. Song, S. Shrestha, J. Miao, L. W. Cui, and W. H. Guan, "A field-deployable mobile molecular diagnostic system for malaria at the point of need," (in English), *Lab on a Chip*, vol. 16, no. 22, pp. 4341-4349, 2016.
- [62] G. Choi, T. Prince, J. Miao, L. W. Cui, and W. H. Guan, "Sample-to-answer palm-sized nucleic acid testing device towards low-cost malaria mass screening," (in English), *Biosensors & Bioelectronics*, vol. 115, pp. 83-90, Sep 15 2018.
- [63] N. Keller, S. Grimes, P. J. Jardine, and D. E. Smith, "Single DNA molecule jamming and history-dependent dynamics during motor-driven viral packaging," (in English), *Nature Physics*, vol. 12, no. 8, pp. 757-761, Aug 2016.
- [64] M. Gershow and J. A. Golovchenko, "Recapturing and trapping single molecules with a solid-state nanopore," (in English), *Nature Nanotechnology*, vol. 2, no. 12, pp. 775-779, Dec 2007.
- [65] V. Patil and H. Kulkarni, "Comparison of confidence intervals for the Poisson mean: some new aspects," *REVSTAT-Statistical Journal*, vol. 10, no. 2, pp. 211-227, 2012.
- [66] S. Subramanian and R. D. Gomez, "An Empirical Approach for Quantifying Loop-Mediated Isothermal Amplification (LAMP) Using Escherichia coli as a Model System," (in English), *Plos One*, vol. 9, no. 6, p. 0100596, Jun 30 2014.
- [67] D. Fekedulegn, M. P. Mac Siurtain, and J. J. Colbert, "Parameter estimation of nonlinear growth models in forestry," *Silva Fennica*, vol. 33, no. 4, pp. 327-336, 1999.
- [68] S. Subramanian and R. D. Gomez, "An empirical approach for quantifying loop-mediated isothermal amplification (LAMP) using Escherichia coli as a Model System," *PloS one*, vol. 9, no. 6, p. e100596, 2014.
- [69] S. Takeuchi, J. Kim, Y. Yamamoto, and H. H. Hogue, "Development of a high-quantum-efficiency single-photon counting system," *Applied Physics Letters*, vol. 74, no. 8, pp. 1063-1065, 1999.
- [70] R. Nouri, Z. Tang, and W. Guan, "Quantitative Analysis of Factors Affecting the Event Rate in Glass Nanopore Sensors," *ACS Sensors*, 2019/10/15 2019.
- [71] N. A. Bell *et al.*, "Multiplexed ionic current sensing with glass nanopores," *Lab on a Chip*, vol. 13, no. 10, pp. 1859-1862, 2013.

- [72] G. Choi, E. Murphy, and W. Guan, "Microfluidic Time-Division Multiplexing Accessing Resistive Pulse Sensor for Particle Analysis," *ACS Sens*, vol. 4, no. 7, pp. 1957-1963, Jul 16 2019.
- [73] WHO, "Available at <https://covid19.who.int/> [Accessed August 15, 2021]," 2020.
- [74] B. Udugama *et al.*, "Diagnosing COVID-19: the disease and tools for detection," *ACS nano*, vol. 14, no. 4, pp. 3822-3835, 2020.
- [75] D. Thompson and Y. Lei, "Mini review: Recent progress in RT-LAMP enabled COVID-19 detection," *Sensors and Actuators Reports*, vol. 2, no. 1, p. 100017, 2020.
- [76] G.-S. Park *et al.*, "Development of reverse transcription loop-mediated isothermal amplification assays targeting severe acute respiratory syndrome coronavirus 2 (SARS-CoV-2)," *The Journal of Molecular Diagnostics*, vol. 22, no. 6, pp. 729-735, 2020.
- [77] A. L. Wyllie *et al.*, "Saliva or nasopharyngeal swab specimens for detection of SARS-CoV-2," *New England Journal of Medicine*, vol. 383, no. 13, pp. 1283-1286, 2020.
- [78] L. Azzi *et al.*, "Saliva is a reliable tool to detect SARS-CoV-2," *Journal of Infection*, vol. 81, no. 1, pp. e45-e50, 2020.
- [79] I. Yelin *et al.*, "Evaluation of COVID-19 RT-qPCR test in multi sample pools," *Clinical Infectious Diseases*, vol. 71, no. 16, pp. 2073-2078, 2020.
- [80] C. B. Vogels *et al.*, "SalivaDirect: A simplified and flexible platform to enhance SARS-CoV-2 testing capacity," *Med*, vol. 2, no. 3, pp. 263-280., 2021.
- [81] R. Wang *et al.*, "opvCRISPR: One-pot visual RT-LAMP-CRISPR platform for SARS-cov-2 detection," *Biosensors and Bioelectronics*, vol. 172, p. 112766, 2021.
- [82] R. Nouri, Z. Tang, and W. Guan, "Quantitative Analysis of Factors Affecting the Event Rate in Glass Nanopore Sensors," *ACS sensors*, vol. 4, no. 11, pp. 3007-3013, 2019.
- [83] G. Butler-Laporte *et al.*, "Comparison of saliva and nasopharyngeal swab nucleic acid amplification testing for detection of SARS-CoV-2: a systematic review and meta-analysis," *JAMA Intern Med*, vol. 181, no. 3, pp. 353-358, 2021.
- [84] M. Nagura-Ikeda *et al.*, "Clinical evaluation of self-collected saliva by quantitative reverse transcription-PCR (RT-qPCR), direct RT-qPCR, reverse transcription-loop-mediated isothermal amplification, and a rapid antigen test to diagnose COVID-19," *Journal of Clinical Microbiology*, vol. 58, no. 9, pp. e01438-20., 2020.
- [85] M. Parida, S. Sannarangaiah, P. K. Dash, P. Rao, and K. Morita, "Loop mediated isothermal amplification (LAMP): a new generation of innovative gene amplification technique; perspectives in clinical diagnosis of infectious diseases," *Reviews in medical virology*, vol. 18, no. 6, pp. 407-421, 2008.
- [86] J. P. Broughton *et al.*, "CRISPR-Cas12-based detection of SARS-CoV-2," *Nature biotechnology*, vol. 38, no. 7, pp. 870-874, 2020.
- [87] C. A. Holstein, M. Griffin, J. Hong, and P. D. Sampson, "Statistical method for determining and comparing limits of detection of bioassays," *Analytical chemistry*, vol. 87, no. 19, pp. 9795-9801, 2015.
- [88] J. Rodriguez-Manzano *et al.*, "Handheld point-of-care system for rapid detection of SARS-CoV-2 extracted RNA in under 20 min," *ACS central science*, vol. 7, no. 2, pp. 307-317, 2021.
- [89] D. Fologea, E. Brandin, J. Uplinger, D. Branton, and J. Li, "DNA conformation and base number simultaneously determined in a nanopore," *Electrophoresis*, vol. 28, no. 18, pp. 3186-3192, 2007.
- [90] M. H. Zweig and G. Campbell, "Receiver-operating characteristic (ROC) plots: a fundamental evaluation tool in clinical medicine," *Clinical chemistry*, vol. 39, no. 4, pp. 561-577, 1993.

- [91] V. Bewick, L. Cheek, and J. Ball, "Statistics review 13: receiver operating characteristic curves," *Critical care*, vol. 8, no. 6, p. 508., 2004.
- [92] C. Dekker, "Solid-state nanopores," *Nature nanotechnology*, vol. 2, no. 4, pp. 209-215, 2007.
- [93] A. J. Storm, C. Storm, J. Chen, H. Zandbergen, J.-F. Joanny, and C. Dekker, "Fast DNA translocation through a solid-state nanopore," *Nano letters*, vol. 5, no. 7, pp. 1193-1197, 2005.
- [94] B. M. Venkatesan and R. Bashir, "Nanopore sensors for nucleic acid analysis," *Nature nanotechnology*, vol. 6, no. 10, pp. 615-624, 2011.
- [95] R. Nouri, Y. Jiang, X. L. Lian, and W. Guan, "Sequence-Specific Recognition of HIV-1 DNA with Solid-State CRISPR-Cas12a-Assisted Nanopores (SCAN)," *ACS sensors*, vol. 5, no. 5, pp. 1273-1280, 2020.
- [96] D. Fologea, M. Gershow, B. Ledden, D. S. McNabb, J. A. Golovchenko, and J. Li, "Detecting single stranded DNA with a solid state nanopore," *Nano letters*, vol. 5, no. 10, pp. 1905-1909, 2005.
- [97] R. Y. Henley, B. A. Ashcroft, I. Farrell, B. S. Cooperman, S. M. Lindsay, and M. Wanunu, "Electrophoretic deformation of individual transfer RNA molecules reveals their identity," *Nano letters*, vol. 16, no. 1, pp. 138-144, 2016.
- [98] G. M. Skinner, M. van den Hout, O. Broekmans, C. Dekker, and N. H. Dekker, "Distinguishing single- and double-stranded nucleic acid molecules using solid-state nanopores," *Nano Letters*, vol. 9, no. 8, pp. 2953-2960, 2009.
- [99] J. Wilson, L. Sloman, Z. He, and A. Aksimentiev, "Graphene nanopores for protein sequencing," *Advanced functional materials*, vol. 26, no. 27, pp. 4830-4838, 2016.
- [100] E. C. Yusko *et al.*, "Controlling protein translocation through nanopores with bio-inspired fluid walls," *Nature nanotechnology*, vol. 6, no. 4, pp. 253-260, 2011.
- [101] B. Hornblower *et al.*, "Single-molecule analysis of DNA-protein complexes using nanopores," *Nature Methods*, vol. 4, no. 4, pp. 315-317, 2007.
- [102] G. e. Celaya, J. Perales-Calvo, A. Muga, F. Moro, and D. Rodriguez-Larrea, "Label-free, multiplexed, single-molecule analysis of protein-dna complexes with nanopores," *ACS nano*, vol. 11, no. 6, pp. 5815-5825, 2017.
- [103] A. Storm, J. Chen, X. Ling, H. Zandbergen, and C. Dekker, "Fabrication of solid-state nanopores with single-nanometre precision," *Nature materials*, vol. 2, no. 8, pp. 537-540, 2003.
- [104] Y. H. Lanyon *et al.*, "Fabrication of nanopore array electrodes by focused ion beam milling," *Analytical chemistry*, vol. 79, no. 8, pp. 3048-3055, 2007.
- [105] H. Kwok, K. Briggs, and V. Tabard-Cossa, "Nanopore fabrication by controlled dielectric breakdown," *PloS one*, vol. 9, p. e92880, 2014.
- [106] K. Briggs, H. Kwok, and V. Tabard - Cossa, "Automated Fabrication of 2 - nm Solid - State Nanopores for Nucleic Acid Analysis," *Small*, vol. 10, no. 10, pp. 2077-2086, 2014.
- [107] I. Yanagi, R. Akahori, T. Hatano, and K.-i. Takeda, "Fabricating nanopores with diameters of sub-1 nm to 3 nm using multilevel pulse-voltage injection," *Scientific reports*, vol. 4, p. 5000, 2014, Art. no. 5000.
- [108] I. Yanagi, R. Akahori, and K.-i. Takeda, "Stable fabrication of a large nanopore by controlled dielectric breakdown in a high-pH solution for the detection of various-sized molecules," *Scientific reports*, vol. 9, p. 13143, 2019.
- [109] M. Waugh *et al.*, "Solid-state nanopore fabrication by automated controlled breakdown," *Nature Protocols*, vol. 15, no. 1, pp. 122-143, 2020.

- [110] K. A. Roshan, Z. Tang, and W. Guan, "High fidelity moving Z-score based controlled breakdown fabrication of solid-state nanopore," *Nanotechnology*, vol. 30, p. 095502, 2019.
- [111] K. Briggs *et al.*, "Kinetics of nanopore fabrication during controlled breakdown of dielectric membranes in solution," *Nanotechnology*, vol. 26, p. 084004, 2015.
- [112] M. Dong, Z. Tang, X. He, and W. Guan, "Direct Observation of Redox Induced Bubble Generation and Nanopore Formation Dynamics in Controlled Dielectric Breakdown," *ACS Applied Electronic Materials*, vol. 2, no. 9, pp. 2954-2960, 2020.
- [113] S. Lombardo, J. H. Stathis, B. P. Linder, K. L. Pey, F. Palumbo, and C. H. Tung, "Dielectric breakdown mechanisms in gate oxides," *Journal of applied physics*, vol. 98, p. 121301, 2005.
- [114] Y. Wang, C. Ying, W. Zhou, L. de Vreede, Z. Liu, and J. Tian, "Fabrication of multiple nanopores in a SiN<sub>x</sub> membrane via controlled breakdown," *Scientific reports*, vol. 8, p. 1234, 2018.
- [115] A. P. Ivanov, K. J. Freedman, M. J. Kim, T. Albrecht, and J. B. Edel, "High precision fabrication and positioning of nanoelectrodes in a nanopore," *ACS nano*, vol. 8, no. 2, pp. 1940-1948, 2014.
- [116] P. Krishnakumar *et al.*, "Slowing DNA translocation through a nanopore using a functionalized electrode," *ACS nano*, vol. 7, no. 11, pp. 10319-10326, 2013.
- [117] F. Nicoli, D. Verschueren, M. Klein, C. Dekker, and M. P. Jonsson, "DNA translocations through solid-state plasmonic nanopores," *Nano letters*, vol. 14, no. 12, pp. 6917-6925, 2014.
- [118] C. R. Crick *et al.*, "Precise attoliter temperature control of nanopore sensors using a nanoplasmonic bullseye," *Nano letters*, vol. 15, no. 1, pp. 553-559, 2015.
- [119] M. P. Cecchini *et al.*, "Rapid ultrasensitive single particle surface-enhanced raman spectroscopy using metallic nanopores," *Nano letters*, vol. 13, no. 10, pp. 4602-4609, 2013.
- [120] M. Belkin, S.-H. Chao, M. P. Jonsson, C. Dekker, and A. Aksimentiev, "Plasmonic nanopores for trapping, controlling displacement, and sequencing of DNA," *ACS nano*, vol. 9, no. 11, pp. 10598-10611, 2015.
- [121] M. P. Jonsson and C. Dekker, "Plasmonic nanopore for electrical profiling of optical intensity landscapes," *Nano letters*, vol. 13, no. 3, pp. 1029-1033, 2013.
- [122] S. Pud, D. Verschueren, N. Vukovic, C. Plesa, M. P. Jonsson, and C. Dekker, "Self-aligned plasmonic nanopores by optically controlled dielectric breakdown," *Nano letters*, vol. 15, no. 10, pp. 7112-7117, 2015.
- [123] C. E. Arcadia, C. C. Reyes, and J. K. Rosenstein, "In situ nanopore fabrication and single-molecule sensing with microscale liquid contacts," *ACS nano*, vol. 11, no. 5, pp. 4907-4915, 2017.
- [124] Y. Zhang *et al.*, "Nanopore Formation via Tip - Controlled Local Breakdown Using an Atomic Force Microscope," *Small Methods*, vol. 3, p. 1900147, 2019.
- [125] A. T. Carlsen, K. Briggs, A. R. Hall, and V. Tabard-Cossa, "Solid-state nanopore localization by controlled breakdown of selectively thinned membranes," *Nanotechnology*, vol. 28, p. 085304, 2017.
- [126] Y. Wang, Q. Chen, T. Deng, and Z. Liu, "Nanopore fabricated in pyramidal HfO<sub>2</sub> film by dielectric breakdown method," *Applied Physics Letters*, vol. 111, p. 143103, 2017.
- [127] Y. Yuan *et al.*, "Sub-20 nm nanopores sculptured by a single nanosecond laser pulse," *arXiv* vol. 1806, p. 08172, 2018.
- [128] C. Ying *et al.*, "Formation of single nanopores with diameters of 20–50 nm in silicon nitride membranes using laser-assisted controlled breakdown," *ACS nano*, vol. 12, no. 11, pp. 11458-11470, 2018.



- [129] T. Gilboa, E. Zvuloni, A. Zreben, A. H. Squires, and A. Meller, "Automated, Ultra - Fast Laser - Drilling of Nanometer Scale Pores and Nanopore Arrays in Aqueous Solutions," *Advanced Functional Materials*, vol. 30, p. 1900642, 2020.
- [130] N. Di Fiori, A. Squires, D. Bar, T. Gilboa, T. D. Moustakas, and A. Meller, "Optoelectronic control of surface charge and translocation dynamics in solid-state nanopores," *Nature nanotechnology*, vol. 8, no. 12, pp. 946-951, 2013.
- [131] O. N. Assad, N. Di Fiori, A. H. Squires, and A. Meller, "Two color DNA barcode detection in photoluminescence suppressed silicon nitride nanopores," *Nano letters*, vol. 15, no. 1, pp. 745-752, 2015.
- [132] T. Gilboa, A. Zreben, A. Girsault, and A. Meller, "Optically-monitored nanopore fabrication using a focused laser beam," *Scientific reports*, vol. 8, p. 9765, 2018.
- [133] X. He, Z. Tang, S. Liang, M. Liu, and W. Guan, "Confocal scanning photoluminescence for mapping electron and photon beam induced microscopic changes in SiN<sub>x</sub> during nanopore fabrication," *Nanotechnology*, vol. 31, p. 395202, 2020.
- [134] S. Logan, "The origin and status of the Arrhenius equation," *Journal of Chemical Education*, vol. 59, no. 4, pp. 279-281, 1982.
- [135] M. Kimura and H. Koyama, "Mechanism of time-dependent oxide breakdown in thin thermally grown SiO<sub>2</sub> films," *Journal of applied physics*, vol. 85, no. 11, pp. 7671-7681, 1999.
- [136] H. Cramer, J. Oliver, and R. Porter, "Lifetime of SiN capacitors determined from ramped voltage and constant voltage testing," in *2006 CS MANTECH Conference*, 2006, pp. 91-94.
- [137] M. Wanunu, J. Sutin, B. McNally, A. Chow, and A. Meller, "DNA translocation governed by interactions with solid-state nanopores," *Biophysical journal*, vol. 95, no. 10, pp. 4716-4725, 2008.
- [138] S. Liang *et al.*, "Noise in nanopore sensors: sources, models, reduction, and benchmarking," *Nanotechnology and Precision Engineering*, vol. 3, no. 1, pp. 9-17, 2020.
- [139] H. Harapan *et al.*, "Coronavirus disease 2019 (COVID-19): A literature review," *Journal of infection and public health*, vol. 13, no. (5), pp. 667-673, 2020.
- [140] N. Zhu *et al.*, "A novel coronavirus from patients with pneumonia in China, 2019," *New England journal of medicine*, vol. 382, pp. 727-733, 2020.
- [141] "World Health Organization (WHO)," *WHO coronavirus-2019*. <https://www.who.int/emergencies/diseases/novel-coronavirus-2019>.
- [142] J. S. Tregoning, K. E. Flight, S. L. Higham, Z. Wang, and B. F. Pierce, "Progress of the COVID-19 vaccine effort: viruses, vaccines and variants versus efficacy, effectiveness and escape," *Nature Reviews Immunology*, vol. 21, no. 10, pp. 626-636, 2021.
- [143] J. F.-W. Chan *et al.*, "Improved molecular diagnosis of COVID-19 by the novel, highly sensitive and specific COVID-19-RdRp/Hel real-time reverse transcription-PCR assay validated in vitro and with clinical specimens," *Journal of clinical microbiology*, vol. 58, no. 5, pp. e00310-20, 2020.
- [144] A. Tahamtan and A. Ardebili, "Real-time RT-PCR in COVID-19 detection: issues affecting the results," *Expert review of molecular diagnostics*, vol. 20, no. 5, pp. 453-454, 2020.
- [145] C. B. Vogels *et al.*, "Analytical sensitivity and efficiency comparisons of SARS-CoV-2 RT-qPCR primer-probe sets," *Nature microbiology*, vol. 5, no. 10, pp. 1299-1305, 2020.
- [146] G. C. Mak *et al.*, "Evaluation of rapid antigen test for detection of SARS-CoV-2 virus," *Journal of Clinical Virology*, vol. 129, p. 104500, 2020.

- [147] J. Dinnes *et al.*, "Rapid, point-of-care antigen and molecular-based tests for diagnosis of SARS-CoV-2 infection," *Cochrane Database of Systematic Reviews*, vol. Revision, no. 3, 2021.
- [148] E. Albert *et al.*, "Field evaluation of a rapid antigen test (Panbio™ COVID-19 Ag Rapid Test Device) for COVID-19 diagnosis in primary healthcare centres," *Clinical Microbiology and Infection*, vol. 27, no. 3, pp. 472. e7-472. e10, 2021.
- [149] I. Torres, S. Poujois, E. Albert, J. Colomina, and D. Navarro, "Evaluation of a rapid antigen test (Panbio™ COVID-19 Ag rapid test device) for SARS-CoV-2 detection in asymptomatic close contacts of COVID-19 patients," *Clinical Microbiology and Infection*, vol. 27, no. 4, pp. 636. e1-636. e4, 2021.
- [150] A. Scohy, A. Anantharajah, M. Bodéus, B. Kabamba-Mukadi, A. Verroken, and H. Rodriguez-Villalobos, "Low performance of rapid antigen detection test as frontline testing for COVID-19 diagnosis," *Journal of Clinical Virology*, vol. 129, p. 104455, 2020.
- [151] N. Taleghani and F. Taghipour, "Diagnosis of COVID-19 for controlling the pandemic: A review of the state-of-the-art," *Biosensors and Bioelectronics*, vol. 174, p. 112830, 2021.
- [152] H. Van Nguyen, V. D. Nguyen, H. Q. Nguyen, T. H. T. Chau, E. Y. Lee, and T. S. Seo, "Nucleic acid diagnostics on the total integrated lab-on-a-disc for point-of-care testing," *Biosensors and Bioelectronics*, vol. 141, p. 111466, 2019.
- [153] G. Butler-Laporte *et al.*, "Comparison of saliva and nasopharyngeal swab nucleic acid amplification testing for detection of SARS-CoV-2: a systematic review and meta-analysis," *JAMA internal medicine*, vol. 181, no. 3, pp. 353-360, 2021.
- [154] C. B. Vogels *et al.*, "SalivaDirect: A simplified and flexible platform to enhance SARS-CoV-2 testing capacity," *Med*, vol. 2, no. 3, pp. 263-280, 2021.
- [155] M. A. Lalli *et al.*, "Rapid and extraction-free detection of SARS-CoV-2 from saliva by colorimetric reverse-transcription loop-mediated isothermal amplification," *Clinical chemistry*, vol. 67, no. 2, pp. 415-424, 2021.
- [156] T. Notomi *et al.*, "Loop-mediated isothermal amplification of DNA," *Nucleic acids research*, vol. 28, no. 12, pp. e63-e63, 2000.
- [157] Y. H. Baek *et al.*, "Development of a reverse transcription-loop-mediated isothermal amplification as a rapid early-detection method for novel SARS-CoV-2," *Emerging microbes & infections*, vol. 9, no. 1, pp. 998-1007, 2020.
- [158] M. Jiang *et al.*, "Development and validation of a rapid, single-step reverse transcriptase loop-mediated isothermal amplification (RT-LAMP) system potentially to be used for reliable and high-throughput screening of COVID-19," *Frontiers in cellular and infection microbiology*, vol. 10, p. 331, 2020.
- [159] Y. Kitagawa *et al.*, "Evaluation of rapid diagnosis of novel coronavirus disease (COVID-19) using loop-mediated isothermal amplification," *Journal of Clinical Virology*, vol. 129, p. 104446, 2020.
- [160] R. Lu *et al.*, "Development of a novel reverse transcription loop-mediated isothermal amplification method for rapid detection of SARS-CoV-2," *Virologica Sinica*, vol. 35, no. 3, pp. 344-347, 2020.
- [161] X. Zhu *et al.*, "Multiplex reverse transcription loop-mediated isothermal amplification combined with nanoparticle-based lateral flow biosensor for the diagnosis of COVID-19," *Biosensors and Bioelectronics*, vol. 166, p. 112437, 2020.
- [162] Z. Tang *et al.*, "Rapid detection of novel coronavirus SARS-CoV-2 by RT-LAMP coupled solid-state nanopores," *Biosensors and Bioelectronics*, vol. 197, p. 113759, 2022.

- [163] J. Lee and J. U. Song, "Diagnostic accuracy of the Cepheid Xpert Xpress and the Abbott ID now assay for rapid detection of SARS - CoV - 2: a systematic review and meta - analysis," *Journal of medical virology*, vol. 93, no. 7, pp. 4523-4531, 2021.
- [164] N. Chauhan, S. Soni, A. Gupta, and U. Jain, "New and developing diagnostic platforms for COVID-19: A systematic review," *Expert review of molecular diagnostics*, vol. 20, no. 9, pp. 971-983, 2020.
- [165] P. R. Lephart *et al.*, "Comparative study of four SARS-CoV-2 Nucleic Acid Amplification Test (NAAT) platforms demonstrates that ID NOW performance is impaired substantially by patient and specimen type," *Diagnostic Microbiology and Infectious Disease*, vol. 99, no. 1, p. 115200, 2021.
- [166] W. Zhen, E. Smith, R. Manji, D. Schron, and G. J. Berry, "Clinical evaluation of three sample-to-answer platforms for detection of SARS-CoV-2," *Journal of clinical microbiology*, vol. 58, no. 8, pp. e00783-20, 2020.
- [167] B. M. Katzman, A. M. Wockenfus, B. R. Kelley, B. S. Karon, and L. J. Donato, "Evaluation of the Visby medical COVID-19 point of care nucleic acid amplification test," *Clinical Biochemistry*, 2021.
- [168] A. Renzoni *et al.*, "Analytical evaluation of Visby Medical RT-PCR portable device for rapid detection of SARS-CoV-2," *Diagnostics*, vol. 11, no. 5, p. 813, 2021.
- [169] H. M. Zowawi *et al.*, "Portable RT-PCR system: a rapid and scalable diagnostic tool for COVID-19 testing," *Journal of clinical microbiology*, vol. 59, no. 5, pp. e03004-20, 2021.
- [170] C. R. Voelker *et al.*, "Evaluating sensitivity and specificity of the Biomeme Franklin™ three9 real-time PCR device and SARS-CoV-2 go-strips assay using clinical samples," *Journal of Clinical Virology*, vol. 146, p. 105046, 2022.
- [171] C. A. Hogan *et al.*, "Comparison of the Accula SARS-CoV-2 test with a laboratory-developed assay for detection of SARS-CoV-2 RNA in clinical nasopharyngeal specimens," *Journal of clinical microbiology*, vol. 58, no. 8, pp. e01072-20, 2020.
- [172] F. M. Liotti *et al.*, "Evaluating the newly developed BioFire COVID-19 test for SARS-CoV-2 molecular detection," *Clinical Microbiology and Infection*, vol. 26, no. 12, pp. 1699-1700, 2020.
- [173] A. Harrington *et al.*, "Comparison of Abbott ID Now and Abbott m2000 methods for the detection of SARS-CoV-2 from nasopharyngeal and nasal swabs from symptomatic patients," *Journal of Clinical Microbiology*, vol. 58, no. 8, pp. e00798-20, 2020.
- [174] "SARS-CoV-2 Reference Panel Comparative Data," <https://www.fda.gov/medical-devices/coronavirus-covid-19-and-medical-devices/sars-cov-2-reference-panel-comparative-data>.
- [175] L. J. Donato *et al.*, "Evaluation of the Cue Health point-of-care COVID-19 (SARS-CoV-2 nucleic acid amplification) test at a community drive through collection center," *Diagnostic Microbiology and Infectious Disease*, vol. 100, no. 1, p. 115307, 2021.
- [176] G.-C. Liu, W. Chen, M.-J. Gao, L.-B. Song, X.-Y. Hu, and Y.-D. Zhao, "Ion-current-rectification-based customizable pH response in glass nanopipettes via silanization," *Electrochemistry Communications*, vol. 93, pp. 95-99, 2018.
- [177] X. He, Z. Tang, S. Liang, M. Liu, and W. Guan, "Confocal scanning photoluminescence for mapping electron and photon beam-induced microscopic changes in SiNx during nanopore fabrication," *Nanotechnology*, vol. 31, no. 39, p. 395202, 2020.
- [178] I. M. Lobato and C. K. O'Sullivan, "Recombinase polymerase amplification: Basics, applications and recent advances," *Trac Trends in analytical chemistry*, vol. 98, pp. 19-35, 2018.

VITA  
Zifan Tang

### Education

- Ph.D. candidate in Electrical Engineering  
**The Pennsylvania State University**, University Park, Pennsylvania, USA
- Master in Instrument Engineering  
**Tianjin University**, Tianjin, China
- Bachelor in Instrument Engineering  
**Xi'an Shiyu University**, Xi'an, China

### Journal Publication

1. **Z. Tang**, J.Cui, A. Kshirsagar, T. Liu and W. Guan, “. Saliva-based SARS-Cov-2 Self-Testing with RT-LAMP In a Mobile Device (SLIDE),” In preparation.
2. T. Liu, G. Choi, **Z. Tang**, and W. Guan, "Fingerpick Blood-Based Nucleic Acid Testing on A USB Interfaced Device towards HIV self-testing." *Biosensors and Bioelectronics*, 114255,209,2022.
3. M. Dong, **Z. Tang**, S. Hicks, and W. Guan "Rolling Circle Amplification-Coupled Glass Nanopore Counting of Mild Traumatic Brain Injury-Related Salivary miRNAs." *Analytical Chemistry*, 3865-3871, 94(9), 2022.
4. G. Choi, **Z. Tang**, and W. Guan, "Microfluidic high-throughput single-cell mechanotyping : Devices and applications." *Nanotechnology and Precision Engineering* 4045002, 4, 2022.
5. **Z. Tang**, N. Nouri, M. Dong, J. Yang, Y. Zhu, W. Greene, M. Yon, M. Nair, S. Kuchipudi, and W. Guan, “. Rapid Detection of Novel Coronavirus SARS-CoV-2 by RT-LAMP Coupled Solid-State Nanopore,” *Biosensors and Bioelectronics*, 113759, 197, 2021.
6. **Z. Tang**, M. Dong, X. He, W. Guan, “On Stochastic Reduction in Laser-Assisted Dielectric Breakdown for Programmable Nanopore Fabrication,” *ACS Applied Materials & Interface*, 13383, 13, 2021.
7. R. Nouri, **Z. Tang**, M. Dong, T. Liu, A. Kshirsagar, and W. Guan, “CRISPR-based detection of SARS-CoV-2: A review from sample to result”. *Biosensors and Bioelectronics*, 2021, 15, 113012.
8. R. Nouri, Y. Jiang, **Z. Tang** and W. Guan. Detection of SARS-CoV-2 with Solid-State CRISPR-Cas12a-Assisted Nanopores. *Nano letters*, 8393-8400, 19, 2021.
9. M. Dong, **Z. Tang**, X. He, and W. Guan "Direct Observation of Redox-Induced Bubble Generation and Nanopore Formation Dynamics in Controlled Dielectric Breakdown." *ACS Applied Electronic Materials* 2954-2960, 2(9), 2020.
10. S. Liang, F Xiang, **Z. Tang**, and W. Guan et al. “Noise in nanopore sensors: sources, models, reduction, and benchmarking”, *Nanotechnology and Precision Engineering*, 9-17, 3(1), 2020.
11. X. He, **Z. Tang**, M. Dong, W. Guan "Confocal scanning photoluminescence for mapping electron and photon beam-induced microscopic changes in SiNx during nanopore fabrication." *Nanotechnology*, 395202, 31(39), 2020.
12. **Z. Tang**, G. Choi, R. Nouri, and W. Guan, “Loop-Mediated Isothermal Amplification-Coupled Glass Nanopore Counting Toward Sensitive and Specific Nucleic Acid Testing,” *Nano letters*, 7927-7934, 11, 2019.

13. R. Nouri, **Z. Tang** and W. Guan, "Calibration-Free Nanopore Digital Counting of Single Molecules .Analytical Chemistry, 2019, 91, 11178. (Featured on the front Cover)
14. K. Roshan, **Z. Tang**, and W. Guan. "High fidelity moving Z-score based controlled breakdown fabrication of solid-state nanopore." Nanotechnology, 095502, 30(9) 2019.
15. R. Nouri, **Z. Tang** and W. Guan, "Quantitative analysis of factors affecting the event rate in glass nanopore sensors." ACS sensors, 3007-3013, 4(11), 2019.

#### **Conference Presentation (6 of 11)**

1. **Z. Tang**, J. Cui, and W. Guan, "Saliva-Based Sars-Cov-2 Self-Testing with RT-LAMP In A Mobile Device (SLIDE)," HiltonHead, June. 5-9, 2022, Sonesta Resort, SC, USA (Oral presentation).
2. **Z. Tang**, R. Nouri, and W. Guan, "Rapid Detection of Novel Coronavirus Sars-Cov-2 by Solid-State Nanopore," MicroTAS, Oct. 10-14, 2021, Palm Springs, CA, USA (Oral presentation).
3. **Z. Tang** and W. Guan "Dynamics of Laser-Assisted Silicon Nitride Dielectric Breakdown for Deterministic Fabrication of Solid-State Nanopore" Biophysical society annual meeting, Feb. 15-19, 2020, San Diego, CA, USA.
4. Z. Tang, G. Choi, R. Nouri, and W. Guan, "Nanopore Digital Counting of Amplicons for Ultrasensitive Electronic DNA Detection," IEDM, Dec. 12-16, 2019, San Francisco, CA, USA (Oral presentation).
5. Z. Tang and W. Guan, "Real-Time Nanopore Counting of Amplicons for Ultrasensitive and Label-Free Sequence-Specific DNA Detection". Biophysical society annual meeting, Mar. 03-06, 2019, Baltimore, MD, USA.

#### **Award**

- HiltonHead Conference, 2022 Student Travel Award
- Melvin P. Bloom Memorial Outstanding Doctoral Research Award in Electrical Engineering (2022)
- China National Scholarship, Tianjin University (2%)
- First-class Scholarship, (Tianjin University (10%)
- Outstanding MS Graduates (Tianjin University, 2017)